Benchmarking Organic Thin Film Transistors and the Selective Wavelength Exposure of Carbon Nanotube Transistors

Nicholas Dallaire

Thesis submitted to the University of Ottawa
in partial fulfilment of the requirements for the
Master of Science, Physics

Department of Physics
Faculty of Science
University of Ottawa

Acknowledgements

To begin I would like to express the biggest thank you for both of my wonderful and supporting supervisors Karin Hinzer and Benoit Lessard. Both have guided me throughout my Master's and even part of my undergraduate degree. Their support, understanding and guidance has truly given me a memorable experience. I would also like to thank my modeling project supervisor, Prof Blawid who opened my mind to the world of data modeling. I would not be where I am today if it was not for the help from Dr Brendan Mirka, his guidance and teachings in nanotube fabrication, properties and characterisation were invaluable. I would be remiss if I would not additionally pass my gratitude to both research groups, the SUNLAB for all their help on the optics side of things, especially Robert and Sebastian for painstakingly teaching me laser alignment and calibration. And the Lessard research group for their continuous support during fabrication, no matter the time of day. Especially, Sam and Rose who always seems to know how to fix everything, Joe who brings order to the lab and all our projects and May who helped me with the everyday life in the lab.

Finally, I would like to thank my family, friends and colleagues who have helped keep a leveled head and who have supported my projects and aspirations at each stop on my path.

Abstract

Carbon based semiconductors such as conjugated polymer or single walled carbon nanotubes (SWNT) are promising materials for use next generation printable and wearable electronics. Thin film transistors (TFTs) are often viewed as a building block for more complex electronic device, however, lack of proper characterization of these devices using these novel carbon-based materials is preventing their large-scale adoption.

This thesis has two sections; in the first section I explored and improved a novel electrical model originally developed for organic or polymer-based TFTs called the organic virtual source emission diffusion model (OVSED). I improved this model by adding a variable contact resistance parameter and effective gate voltages. I then found better agreement between model and experimental data using this improved OVSED model against the conventional MOSFET based models: the SH and Y-function models, for poly{[N,N′-bis(2-octyldodecyl)-naphthalene-1,4,5,8-bis(dicarboximide)-2,6-diyl]-alt-5,5′-(2,2′-bithiophene)} (P(NDI2OD-T2)) based OTFTs. The new model proved to be an efficient tool for benchmarking polymer based TFTs and provided an efficient way to characterize and reduce contact resistance in the devices.

In the second section, I explore the effect of light on a series of conjugated polymer wrapped SWNT TFTs. A structure property relationship was established between the wrapping polymer structure and the exposure wavelength intensity. We demonstrated that SWNT TFTs can act as photodetectors after an initial light soak. Finally, we further characterized the SWNT TFTs using our OVSED model validating the observed structure property relationship. Overall this thesis demonstrates steps towards proper characterization of emerging carbon based semiconductors used in TFTs.

Résumé

Les semi-conducteurs à base de carbone, tels que les polymères conjugués ou les nanotubes de carbone à paroi simple (SWNT), sont des matériaux prometteurs pour la prochaine génération d'appareils électroniques imprimables et portables. Les transistors à couche mince (TFT) sont souvent considérés comme un élément de base pour des dispositifs électroniques plus complexes, mais la caractérisation incorrecte de ces dispositifs utilisant ces nouveaux matériaux à base de carbone empêche leur adoption à grande échelle.

Cette thèse comporte deux sections ; dans la première, j'ai exploré et amélioré un nouveau modèle électrique développé à l'origine pour les TFT organiques ou à base de polymères, appelé le modèle de diffusion d'émission de source virtuelle organique (OVSED). J'ai amélioré ce modèle en ajoutant un paramètre de résistance de contact variable et des tensions de grille effectives. J'ai ensuite constaté une meilleure concordance entre le modèle et les données expérimentales en utilisant ce modèle OVSED amélioré par rapport aux modèles conventionnels basés sur les MOSFET : les modèles à fonction SH et Y, pour les OTFT à base de poly{[N,N′-bis(2-octyldodecyl)-naphtalène-1,4,5,8-bis(dicarboximide)-2,6-diyl]-alt-5,5′-(2,2′-bithiophène)} (P(NDI2OD-T2)). Le nouveau modèle s'est avéré être un outil efficace pour comparer les TFT à base de polymères et a fourni un moyen efficace de caractériser et de réduire la résistance de contact dans les dispositifs.

Dans la deuxième partie, j'explore l'effet de la lumière sur une série de TFT à base de SWNT enveloppés de polymères conjugués. Une relation structure-propriété a été établie entre la structure du polymère enveloppant et l'intensité de la longueur d'onde d'exposition. Nous avons démontré que les SWNT TFT peuvent agir comme des photodétecteurs après une imprégnation

initiale de lumière. Enfin, nous avons caractérisé les SWNT TFT à l'aide de notre modèle OVSED en validant la relation structure-propriété observée. Dans l'ensemble, cette thèse démontre les étapes vers une caractérisation appropriée des semi-conducteurs émergents à base de carbone utilisés dans les TFT.

List of Peer-Reviewed Publications

1. **Dallaire, N. J.,** Brixi, S., Claus, M., Blawid, S. & Lessard, B. H. Benchmarking contact quality in N-type organic thin film transistors through an improved virtual-source emission-diffusion model. *Appl Phys Rev* **9**, 11418 (2022).

   In this publication, I measured the current-voltage curves for half the devices, I extracted device characteristics for all the devices using the Shichman-Hodges model. I also fitted the organic virtual source emission diffusion (OVSED) model to the measurements and improved the model to offer better fittings. I improved the original MATLAB code used to run the OVSED model, given to me by Prof Blawid. The resistance measurements were also done by me, via the Y-function method coded on Python. Once the project was complete, I wrote most of the published manuscript. The other authors measured the other half of the devices, gave insight during the project and helped with during the redaction of the manuscript.

2. Blawid, S., **Dallaire, N. J.** & Lessard, B. H. Self-Consistent Extraction of Mobility and Series Resistance: A Hierarchy of Models for Benchmarking Organic Thin-Film Transistors. *IEEE Journal on Flexible Electronics* **1**, 114–121 (2022).

   In this publication I provided the data and fitting from the previous manuscript. I also provided curve fittings and repeatability tests. I was consulted for and wrote a small portion of the manuscript.

3. **Dallaire, N. J.** Mirka, B.; Manion, J. G.; Bodnaryk, W. J.; Fong, D.; Adronov, A.; Hinzer, K.; Lessard, B. H. Conjugated Wrapping Polymer Influences on Photoexcitation of Single-Walled Carbon Nanotube-Based Thin Film Transistors. *J. Mater. Chem. C*, **11** (27), 9161–9171 (2023).

   In this work I synthesized the three single walled carbon nanotube dispersions and fabricated the transistors. I setup and calibrated the laser stage, extracted the devices current-voltage curves and extracted device parameters via both models. For this work, I converted the MATLAB code for the OVSED model, into Python for easier implementation and the eventual formation of an executable version. I wrote the paper and made most of the figures with other authors providing edits and small changes.

The author also contributed to the following works through their Master's.

1. Samantha Brixi , **Nicholas Dallaire**, Benoit Lessard, "Development and modelling of improved n-type solution-processed field-effect transistors" Oral presentation at the International Conference on Science and Technology of Synthetic Metals (ICSM) in Glasgow. (July 2022)

2. **Nicholas J. Dallaire**, Samantha Brixi, Stefan Blawid, Benoît H. Lessard, “Benchmarking Organic Thin Film Transistors Through an Improved Novel Virtual-Source Emission-Diffusion Model” UOttawa Engineering and Computer Science Graduate Poster Competition, received an honorable mention, (March 2023)

3. **Nicholas J Dallaire,** Samantha Brixi, Stefan Blawid, Benoît H. Lessard “Benchmarking Organic Thin Film Transistors Through an Improved Novel Virtual-Source Emission-Diffusion Model”. Oral presentation given at the international F-pi conference in North Carolina. June 2023

4. Samantha Brixi , **Nicholas Dallaire**, Benoit Lessard, "Enhancing stability and performance of n-type OFETs" Poster presentation at the green electronics network AGM in Montreal (June 2023)

Table of Contents

List of Abbreviations, Symbols and Acronyms

(n, m)	SWNT Chiral Indices
$\vec{a}, \vec{b}, \vec{c}$	Basis vectors in a 3D lattice
$(\vec{a}, \vec{b})$ and a_1, a_2	Single-Walled carbon nanotube Unit Vectors
a	Lattice constant
$a_{c\text{-}c}$	Carbon-Carbon Bond Length (1.44 Å)
AFM	Atomic Force Microscopy
Au	Gold
$\overrightarrow{b_1}, \overrightarrow{b_2}$	SWNT Reciprocal Lattice Vectors
c	Speed of light
C_G	Capacitance density of the gate
C_i	Capacitance density of the oxide
C_S	Capacitance density of the semiconductor
$\overrightarrow{C_h}$	Chiral Vector
Cr	Chromium
CuPc	Copper phthalocyanine
CVD	Chemical Vapour Deposition
d_i	SWNT diameter
DOS	Density of States
DNA	Deoxyribonucleic acid
E	Energy
E_c	Conduction band
E_g	Band gap
E_o	Permittivity in vacuum
E_v	Valence band
F_{sat}	Function which allows the transition from saturation to linear regimes
g_m	Transconductance
GCA	Gradual channel approximation

h	Planck's constant
He	Helium
HiPco	SWNT Synthetic Route, High-Pressure Disproportionation of Carbon Monoxide
HOMO	Highest-Occupied Molecular Orbital
H_2O	Dihydrogen monoxide
I_{DLeak}	Parasitic leakage current
I_{DS}	Drain-source current
$I_{DS_{lin}}$	Drain-source current in the linear regime
$I_{DS_{Sat}}$	Drain-source current in the saturation regime
I_{OFF}	Off current
I_{ON}	On current
IV	Current-voltage
J_{DS}	Drain current density
k	Momentum
k_B	Boltzmann constant
k_d	Dielectric constant
k_{max}	Maximum momentum in the Brillouin zone
K_1	Reciprocal circumferential vector
K_2	Reciprocal longitudinal vector
L	Channel length
l	Unitless value describing the exponential tail of the density of trap states
L_G	Gate length
LUMO	Lowest-Unoccupied Molecular Orbital
M_{11}	Metallic SWNT First van-Hove Singularity
M, K, Γ	High symmetry points
m-SWNT	Metallic Single-Walled Carbon Nanotube
Mn	Manganese
MOSFET	Metal Oxide Semiconducting Field Effect Transistors
Mw	Molecular weight
n	Gate coupling factor

N_2	Dinitrogen
N2200	poly{[N,N′-bis(2-octyldodecyl)-naphthalene-1,4,5,8-bis(dicarboximide)-2,6-diyl]-alt-5,5′-(2,2′bithiophene)}
ND	Neutral Density
NDI	Naphthalenetetracarboxylic diimide
NIR	Near-Infrared
O_2	Dioxygen
OTFT	Organic Thin-Film Transistor
OTS	Octyltrichlorosilane
OVSED	Organic Virtual-Source Emission-Diffusion
PCF	Polymer, Poly(9,9'-didodecy1fluorene-co-N-(2'-decy1tetradecane)-carbazole)
PFMB	Polymer, Poly[(2,7-(9,9-dihexade-cy1f1uorene)-alt-2,5-dimethoxybenzene]
PFO-BPy	Polymer, Poly(9,9-di-n-octy1f1uorene-co-bipyridine)
q	Elementary charge
Q	Charge density
Q_{free}	Total charge of the free charges
Q_n	Charge function
$\vec{R}$	Translational vector in a lattice
R_C	Contact resistance
RFID	Radio Frequency Identification
R_{max}	Maximum resistance
R_O	Minimum resistance
S_{11}	Semiconducting SWNT first Van-Hove singularity
S_{22}	Semiconducting SWNT second Van-Hove singularity
S_{33}	Semiconducting SWNT third Van-Hove singularity
sc-SWNT	Semiconducting SWNT
SH	Shichman-Hodges
Si	Silicon
SiO_2	Silicon Dioxide
SWNT	Single-Walled Carbon Nanotube

T	Temperature
t	Critical length for diffusion
TFT	Thin Film Transistor
t_t	Dielectric thickness
UV	Ultra-Violet
V_0	Constant describing the location of the contact resistance transition
V_{DS}	Drain-source voltage
V_{gcrit}	Critical voltage for velocity saturation
V_{GD}	Gate-drain voltage
V_{GS}	Gate-source voltage
V_T	Threshold voltage
V_{temp}	Thermal voltage
$V_{T_{lin}}$	Threshold voltage extracted from the linear regime
$V_{T_{sat}}$	Threshold voltage extracted from the saturation regime
V_{tun}	Constant describing the smoothing of the contact resistance transition
W	Channel width
α	Absorption coefficient
β	Unitless firring parameter
δ	Variable threshold voltage constant
μ	Mobility
μ_d	Drift mobility
μ_e	Electron mobility
υ	Charge velocity
υ_d	Drift velocity
υ_{sat}	High-field bulk saturation velocity
σ_V	Density of valence charge carriers
σ_T	Density of charge traps
θ	Chiral angle
ε	Electric field
λ	The ratio between the gate length and mean free path

λ_f	Mean free path
λ_{ph}	Photon wavelength
γ	Absorption coefficient modulation constant

Chapter 1: Introduction

1.1. Motivation

Carbon-based semiconductors, such as single walled carbon nanotubes (SWNT) and conjugated polymers have desirable physical and electronic properties while also being solution processable which can lead to low temperature integration into flexible plastic substrates. These carbon-based semiconductors have shown great potential in thin film transistors (TFT) and other electronic devices based on TFT . Synthesis of SWNT leads to metallic and semiconducting variants which are often separated and purified using selective dispersion using conjugated polymers. Various conjugated homopolymers and copolymers with different functional groups have been reported to effectively purify the semiconductive SWNTs, however the effect of these polymer wrappings are often overlooked. For example, the effect of light on the device performance as a function of the polymer structure. Secondly, typical carbon based electronics suffer from inaccurate estimation of performance metrics due to over and underestimation of factors such a contact resistance. Unfortunately, most benchmarking tools and models typically used to characterize carbon based TFTs behavior are based off the Metal Oxide Semiconducting Field Effect Transistors (MOSFET) models. These models are based off inorganic ideal semiconductors with negligible contact resistance, low charge trap densities and high mobilities. When applying these models to carbon based TFTs the mobilities are typically overestimated and their behavior cannot be properly evaluated. This is a root problem many face when trying to solve other problems such as contact resistance and polymer interference, hence, new models are required.

1.2. Structure and Scope of Thesis

This thesis focuses on the implementation and improvement of a novel organic thin film transistor characterization model; used to diagnose and bring potential solutions to transistor contact resistance and the innerworkings of the conjugated polymer in single walled carbon nanotube based thin film transistors. This thesis is the culmination of three published papers, two first authors and many presentations. In the second chapter of this thesis, the relevant theory is discussed necessary to understand the chapters following. The theory encompasses basic semiconductor theory, band structure, density of states, charge carrier mobility and photon absorption. The second portion of the theory discusses inorganic and organic semiconductors, introducing single walled carbon nanotubes properties, and synthesis. The theory concludes by introducing transistors with a focus on thin film transistors and transistor models.

Chapter 3 presents a submitted manuscript to Applied Physics Reviews "Benchmarking contact quality in N-type organic thin film transistors through an improved virtual-source emission-diffusion model". The manuscript discusses on contact resistance optimization in organic thin film transistors using electrode interlayers and the importance of using organic models instead of inorganic models when characterizing organic thin film transistors. This is followed by the improvements made to the Organic Virtual-Source Emission-Diffusion model and its validation as an effective benchmarking tool. The final section of the chapter briefly discusses a second manuscript "Self-Consistent Extraction of Mobility and Series Resistance: A Hierarchy of Models for Benchmarking Organic Thin-Film Transistors", focusing on the continued work on the model and its limits.

Chapter 4 introduces the third and final manuscript, "Conjugated Wrapping Polymer Influences on Photoexcitation of Single-Walled Carbon Nanotube-Based Thin Film Transistors". This

manuscript introduces a new problem involving the effects of selective wavelength exposure on single walled carbon nanotube based thin film transistors, with a focus of separating the effects of the dispersion polymer compared to the nanotube during illumination. The improved model was applied to better diagnose the observed behaviors along with traditional models.

Chapter 5 continues upon the works presented in **chapters 3 and 4** by comparing the extracted parameters from the Organic Virtual-Source Emission-Diffusion model from the modeled devices in **chapter 3** to the modeled single walled carbon nanotube devices in **chapter 4**. The chapter focuses on the major differences between both devices and discusses the model limits from the second manuscript. This chapter amalgamates the results from all three manuscripts and brings a conclusion to this work. In this section the raw python code for the model is provided.

Chapter 6 concludes this work. Future work is discussed along with the outcomes of this thesis. The future of the model is addressed giving further direction for continued experiments and research.

Chapter 2: Theory and Overview

In the following subchapters I will briefly introduce basic concepts of semiconductor theory before discussing in depth the theory necessary to understand the following chapters.

2.1. Semiconductors

Crystal structures are defined by their periodic placement of atoms. A single unit of this periodic structure is named a primitive cell. The characterization of the primitive cell is crucial as it defines the crystal's electrical and structural properties. The lattice of a crystal is composed of lattice points, with each primitive cell containing only one point. These points can contain a single atom or a group of atoms which repeat at each point, distance between these points is known as the lattice constant. A position on crystal can be mapped via basis vectors which are valid if the structure remains invariant through translation and every point can be reached. For instance, given $\vec{a}$, $\vec{b}$ and $\vec{c}$ basis vectors, a translation of $\vec{R} = n\vec{a} + m\vec{b} + p\vec{c}$ would have the same pattern for any $n, m, p \in Z$. The reciprocal lattice is a lattice formed with each of its vectors normal to the planes formed in the regular or direct lattice. This new lattice is known as the momentum space or the Fourier transform of the real lattice. In this space the lattice points represent the number of wavevectors in units of inverse distance. The primitive cell in reciprocal space is called a Wigner-Seitz cell or the first Brillouin zone; this zone helps to describe the relationship between the energy of a system, E, and the momentum, k for the entire crystal.[1]

The relationships between the energy and momentum are crucial to understand electronic properties. These relationships are defined by the potential and applied energies, and form bands of allowed states. For semiconductors, unlike for metals, there exists an energy gap between the

bands as seen in **Figure 2.1** for a metallic and semiconducting nanotube. The energy gap, E_g, is the energy required to bring a charge carrier from the lower valence band, E_V to the upper conduction band, E_c. The bandgap is called a direct bandgap when the lowest point in the conduction band is aligned with the highest point in the valence band, such as it is in **Figure 2.1c**. In an indirect bandgap, they are misaligned, and the charge carrier would require a change in momentum to cross the gap. The bandgap can also be observed in the density of states (DOS), which describes the density possible electronic states for a system as a function of energy. The bandgap would be shown as a location where no electronic states are possible, for instance in the gap in **Figure 2.1a**. For metallic structures, there are possible electronic states for every energy level, **Figure 2.1b**.

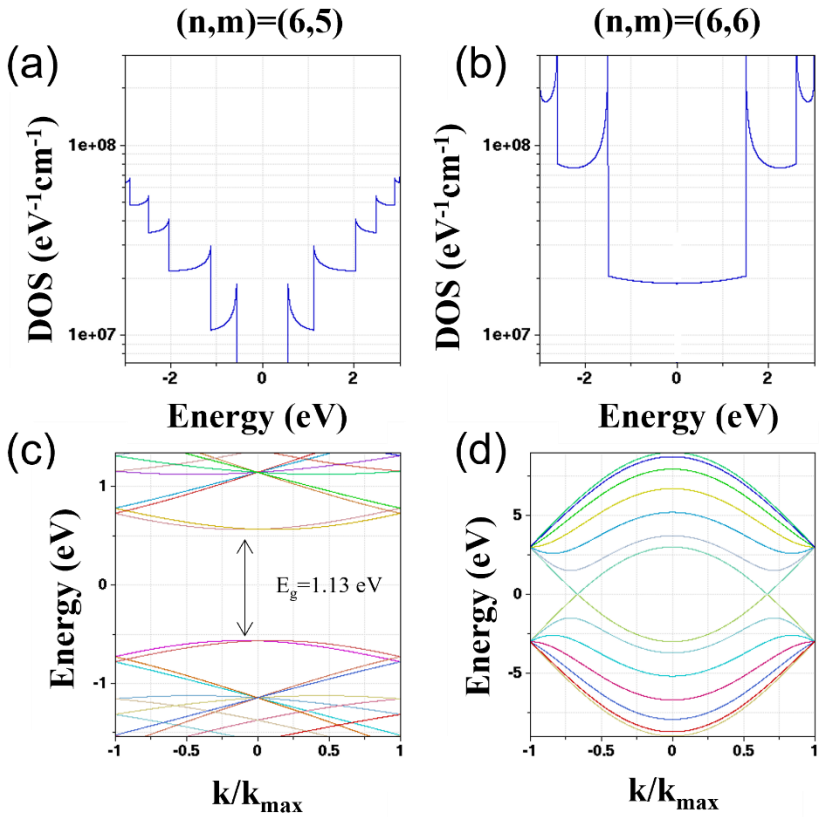

Figure 2.1) Theoretical simulation of the density of states (DOS) for a semiconducting (6,5) (a) and a metallic (6,6) (b) nanotube and energy bands for a semiconducting (6,5) (a) and metallic (6,6) (b) nanotube.[1] (n,m) are the chiral indices which describe the nanotube chiral vector or "roll-up" vector.

The charge carrier's movement through a semiconductor can be defined using its mobility, where for low electric fields is defined as: $\mu = \nu_d/\varepsilon$, where ν_d is the drift velocity and ε is the electric field. The drift velocity is dependent on the charge carrier and the energy band where it is located; thus, holes and electrons have each their own mobilities. The mobility is proportional to the mean free path λ_f, defined as the average distance traveled before the carrier changes its velocity, often due to collisions.

In field effect electronics, electric fields give charge carriers enough energy to surpass the bang gap to reach the conduction band, proving a channel to move charges. However, photons, depending on the absorption coefficient, α, of the semiconductor, can also induce electronic transitions between different bands. This absorption depends on a few factors, $\alpha \propto \left(\frac{hc}{\lambda_{ph}} - E_g\right)^{\gamma}$ where h is Planck's constant 6.6261 x 10^{-34} J*s, c is the speed of light 2.9979 x 10^{8} m/s, λ_{ph} is the photon wavelength in meters and γ is a constant depending on the type of transition (direct or indirect). Excitons, formed through photon absorption, are electron-hole pairs which diffuse through the lattice and could potentially contribute to the current if separated.[1]

2.1.1. Inorganic and Organic Semiconductors

Common examples of inorganic semiconductors include silicon, Si, revered for its many years of study and its tunable bandgap through controlled doping, an introduction of impurities in the semiconductor to change the concentration of a certain charge carrier. Gallium arsenide, GaAs has also piqued the interest of many scientists in recent years due to its direct bandgap.[2] Although

traditional inorganic semiconductors offer exceptional electrical performance, a growing number of electronic applications require mendable, flexible and solution processable semiconductors, demands which are unobtainable by traditional inorganic semiconductors. Organic, or carbon-based semiconductors, are based on small molecule, polymer, or carbon allotrope semiconductors capable of flexibility and solution processability[3]. Common examples of organic semiconductors include the phthalocyanines with various cores, such as copper phthalocyanine (CuPc)[4], or N2200 and other similar polymers which have gained traction for their semi air stability.[5] However, unlike their inorganic counterparts, organic semiconductors contain various potentially undesired properties, such as environmental and temperature sensitivity and larger concentrations of lattice defects.[6] In organic semiconductors, since the discussion often centers around the individual molecules with orbitals rather than the lattice, the conduction band is often replaced by the Lowest Unoccupied Molecular Orbital (LUMO) and similarly, the valence band is replaced by the Highest Occupied Molecular Orbital (HOMO). In both, organic and inorganic semiconductors, holes or electrons can be preferentially transported depending on the semiconductor and the doping. If electrons are the preferred charge carriers, then the transport occurs at the conduction band and the semiconductor is called an *n*-type semiconductor. Inversely, for holes, the transport occurs at the valence band and the semiconductor is called a *p*-type semiconductor.

Semiconductor-Metal contact

A metal's work function is defined as the amount of energy required to bring an electron to vacuum from the fermi level, which is the electrochemical energy of electrons in a material. For a semiconductor, the fermi level lies between the conduction and valence band with the fermi level of *n*-type semiconductors lying closer to the conduction band and the valence band for *p*-type semiconductors . At a metal-semiconductor contact point, due to the difference between the fermi

levels, a depletion region will be created, and charges will flow between both until equilibrium is reached. Based on the position of the fermi levels, there are two possible outcomes, a Schottky barrier where the transport of carriers resembles a diode, where transport is supressed in reverse bias and allowed in forward bias after surpassing the barrier. Alternatively, an Ohmic contact where transport is possible in both direction with a constant resistance. For an *n*-type semiconductor, a Schottky barrier will be formed when the fermi level for the metal is lower than that of the semiconductor, and an Ohmic barrier will be formed. The reverse happens in *p*-type semiconductors. The Ohmic barrier can be reduced by choosing the metal and semiconductor, such that their fermi levels are close while still keeping the condition for Ohmic contacts.

2.1.2. Single-Walled Carbon Nanotubes

Due to their unique electronic and thermal conductivity[7], optical properties[8,9] and mechanical strength[10] Single-Walled Carbon Nanotube (SWNTs) have been thoroughly researched. Because of these, SWNT have gained popularity for applications in photovoltaics[11], chemical sensors[12–14], thin-film transistors[15,16], and many other applications [17].

SWNT are similar to a rolled graphene cylinder, consisting of sp^2-hybridized carbon. They have a diameter of 1 to 2 nm and a length of 1 μm to 500 mm[18], indicating that they possess quasi-one-dimensional properties, as observed by the sharp peaks in the density of states of Figure 2.1ab. The geometry of the tube can be described using graphene lattice base vectors $\overrightarrow{a_1}$ and $\overrightarrow{a_2}$ and a translational vector or chiral vector (Figure 2.2a):

$$\overrightarrow{C_h} = n\overrightarrow{a_1} + m\overrightarrow{a_2} \tag{2.1}$$

$$\overrightarrow{a_1} = \left(\frac{\sqrt{3}}{2}, \frac{1}{2}\right)a \tag{2.2}$$

$$\overrightarrow{a_2} = \left(\frac{\sqrt{3}}{2}, \frac{-1}{2}\right) a \tag{2.3}$$

where $n, m \in \{0, \mathbb{N}\}$, and $a = \sqrt{3} a_{c-c} = 2.46$ Å the lattice constant with $a_{c\text{-}c}$ the carbon-carbon distance. The diameter d_i and chiral angle $0 \leq \theta \leq 30^{o}$ of the nanotube can then be calculated:

$$d_i = \frac{a}{\pi} \sqrt{n^2 + m^2 + nm} \tag{2.4}$$

$$tan\,\theta = \frac{\sqrt{3} m}{2n + m}. \tag{2.5}$$

SWNTs with a chiral angle of 0^{o} are called Zig Zag, 30^{o} are Armchair, and in between, are Chiral. Figure 2.2 depicts a schematic of an unrolled SWNT, and a (6,5) rolled nanotube.[19]

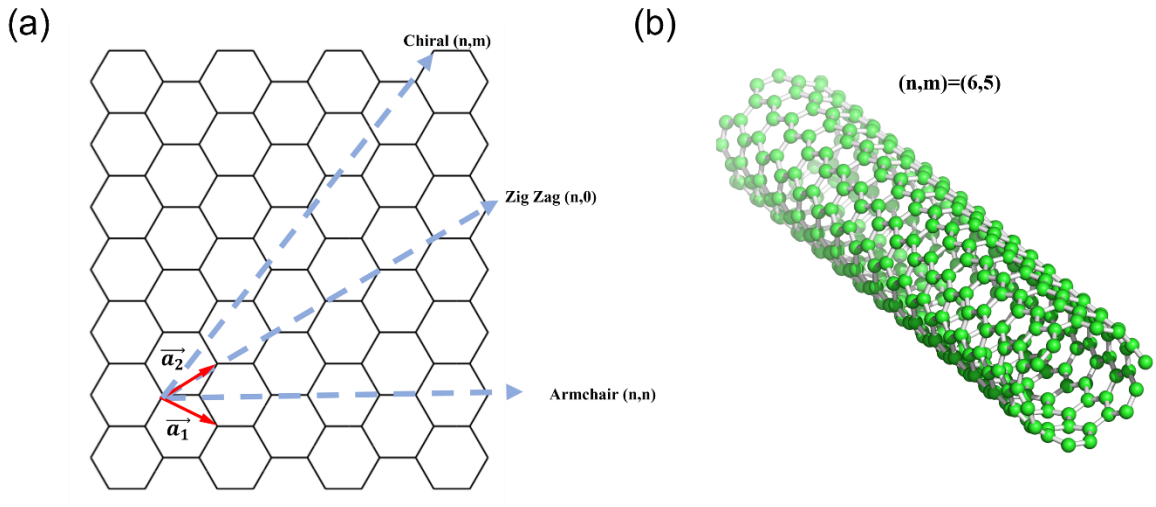

Figure 2.2) a) Schematic of an unrolled SWNT, displaying its hexagonal lattice. The base vectors ($\overrightarrow{a_1}$ and $\overrightarrow{a_2}$) are highlighted in red. The three possible rolling configurations (Zig Zag (n,0), Arm Chair (n,n) and Chiral (n,m)) are shown with dotted blue arrows. b) A model of a (6,5) carbon nanotube.

The Brillouin zone of the SWNT contains three high symmetry points *M, K* and *Γ* and two vectors, K_1 and K_2 which describe the circumferential and longitudinal vectors respectively. The circumferential vector gives rise to discrete vectors describing the electron waveguide, therefore, the electron wavevector is quantized in the K_1 direction. At the *K* symmetry point the conduction

and valence band overlap. If the quantized electron wavevectors intersect the *K* symmetry point, $E_g = 0$ which means the SWNT will have metallic properties such as in Figure 2.1d.

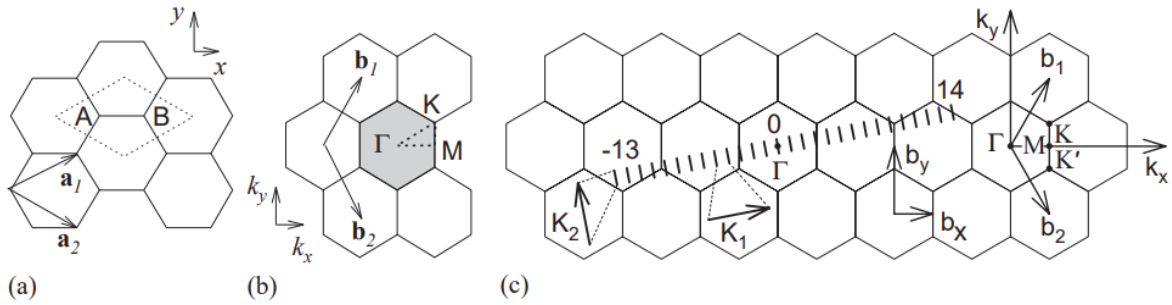

Figure 2.3) (a) A SWNT lattice with the base vectors $\vec{a}_1$, $\vec{a}_2$ along with the unit cell designated by the dotted lines and the carbon atoms *A* and *B*. (b) The reciprocal lattice with its reciprocal base vectors $\vec{b}_1$, $\vec{b}_2$. The Brillouin zone shown in gray with the high symmetry points *M, K* and *Γ*. (c) the electron waveguide traveling along the circumferential direction of the SWNT (the K_1 direction) in the reciprocal lattice. Figure reproduced from Dresselhaus, M. S et al.[20]

This also means that the density of states (DOS) will have a non-zero value at the Fermi level (0 eV) (Figure 2.1b). The opposite is also true, if they do not intersect the SWNT will have a bandgap and will exhibit semiconducting properties. This indicates that the chiral vector and thus the indices (n,m) indicate if the SWNT will have metallic or semiconducting properties. As a general rule, if (n-m)mod(3)=0 then the SWNT is metallic, else it is semiconducting, which indicates that 1/3 of all SWNT are metallic given a random chirality probability during fabrication. The bandgap size in semiconducting SWNTs is also inversely proportional to the diameter size. This can pose a problem where one property is preferred for a specific application, such as in thin film transistors where a semiconducting variant with a smaller bandgap is desired, thus the variants need to be separated.

Synthesis

Many methods exist to synthesize SWNT, each containing their own diameter and length range. A common technique uses chemical vapour deposition (CVD). This method uses the dissociation of hydrocarbon gases, such as high-pressure carbon monoxide, over a transition metal

catalyst, for instance an iron catalyst followed by a dissolution and saturation of the carbon atoms. The disassociated carbon then precipitates into tubular form, forming SWNTs. This method often referred as HiPco, produces SWNTs with a diameter range of 0.8-1.1 nm.[21] Another popular method involves an arc discharge across carbon anode and cathode. In an enclosed environment with a noble gas, such as argon or helium, a carbon anode, typically made of graphite with a cobalt catalyst, is brought near a similar anode without the catalyst. The current passing across the anode and cathode ignites the He into plasma which forces the carbon atoms to evaporate and then condense into SWNT. These typically produce SWNT with a diameter range of 1.2-1.7 nm.[22,23] In this thesis, the SWNTs were fabricated using a plasma torch method similar to arc discharge, where evaporation of black carbon is done through the use of radio frequency plasma torch. This method is used as it has a high production rate ~100 g/h and produces large diameters ranging from 0.9-1.5 nm.[24] Other popular methods with their ranges include laser ablation with 1-1.4 nm and CVD with a cobalt-molybdenum catalyst produces diameters of 0.7-0.9 nm. [25]

SWNT Sorting

As prementioned, the SWNT are required to be separated before they can be integrated into devices. This separation can be obtained using several separation techniques. Such techniques include density gradient ultracentrifugation[26], DNA sorting [27], gel chromatography[28,29] and conjugated polymer extraction[30–33]. In this work, the semiconducting SWNTs were sorted using conjugated polymer extraction as it is a simple, scalable, and effective means of producing high purity (>99.99%[34]) semiconducting SWNT.

The procedure for polymer sorting of SWNT is simple. Raw un-sorted SWNT are combined with selected polymers in a solvent. The mixture is then sonicated in a cooled sonication bath. During sonication, the polymers selectively wrap around semiconducting SWNT while the

metallic variants remain bundled possibly since they are significantly more polarizable than their semiconducting variants.[35,36] Using a short-term, typically 15-30 mins, centrifugation, the metallic SWNT separate from the supernatant which now mostly consist of excess polymer and polymer wrapped semiconducting SWNT. A filtration can then be used to remove any excess polymer. The resulting solution is verified for metallic SWNT and impurities using UV-Vis-NIR and Raman spectroscopy, by calculating the difference in metallic SWNT peak height from raw SWNT to the purified solution.[37]

The polymers used can be tuned to selectively wrap around specific diameter sized semiconducting SWNT. Although the specific mechanisms behind the selectivity have yet to be discovered, certain researchers have discovered that the selectivity is dependent on the polymer molecular weight, backbone and alkyl side chains.

The larger the molecular weight, the larger the polymer. Thus, when wrapping around SWNT, if the polymer is too light consequently too short, it cannot fully wrap around the SWNTs. In contrast, if the polymer molecular weight is too large, the solution viscosity will increase, which could decrease the purity by inhibiting the bundling of metallic SWNT. Works from Rice et al. discovered that the optimal weight ranges from 30 – 90 kg/mol.[38] The polymer backbone can also be used to tune the selectivity. The conjugated polymers used typically have an aromatic backbone of fluoride or carbazole derivatives. [38–42] Depending on the rigidity of the polymer, they will preferentially wrap around larger or smaller SWNT, with smaller diameter SWNT requiring a more flexible polymer backbone. The alkyl chains, similar to both the molecular weight and the backbone, contain an optimal length for the desired diameter. Larger chains promote the selectivity for larger diameters with smaller selecting smaller ones, however if the chains are too long, the

purity decreases, similar to the polymer weights. Optimal ranges seem to be between 10 to 18 carbon atoms.[43,44]

Absorption Spectra

Optical spectroscopy of SWNT can be used to evaluate the purity of semiconducting SWNTs. For large diameter SWNT, four peaks can be observed from 400 – 1800 nm, the first semiconducting transition, S_{11}, located between 1400 and 1700 nm, the second semiconducting transition S_{22} located between 800 and 1100 nm, the first metallic transition, M_{11} located between 600 and 800 nm and finally the third semiconducting transition S_{33} located between 425 and 550 nm. Figure 2.4 shows the absorption spectra for semiconducting SWNTs dispersed using PFO-BPy, the lack of a metallic transition peak indicates a good purity.[45] Due to their quasi one-dimensionality, these peaks arise from the transition energies from the Van Hove Singularities in the DOS in Figure 2.1ab.

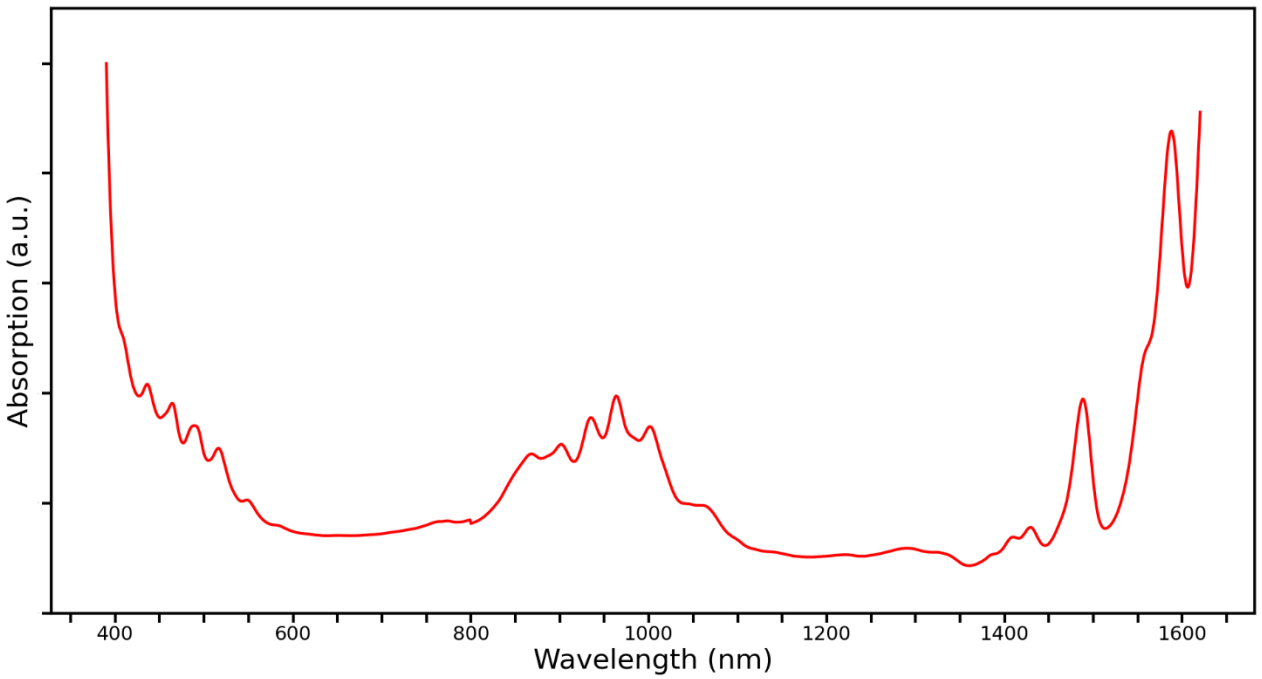

Figure 2.4)*: Normalized absorption profile of PFO-BPy dispersed semiconducting SWNTs.*

2.2. Transistors

Transistors are a three-terminal device, the first sources or emits the current, the second collects or drains the current and the third controls the flow of current through a semiconductor across the first two, often called the base or gate depending on the type of transistor. Transistors are an integral part of any modern electronic device, they the base unit for all logic gates, memory systems, and power systems. Metal Oxide Semiconducting Field Effect Transistors (MOSFET) are currently the leading transistor type capable of high voltage, high current density with low channel resistance.[46] MOSFETs works by employing an electric field between the source and drain electrodes, using capacitance between at the gate and source electrodes which allows the passage of current through the semiconductor between the source and drain. There exist two main types of MOSFETs, the *n*-type, which requires a positive drain-source voltage (V_{DS}) and a positive gate-

source voltage (V_{GS}) and the *p*-type which requires a negative V_{DS} and V_{GS} to function. For *p*-type MOSFETs, the substrate contains excess electrons while the semiconductor connected to the source and drain electrodes contain excess holes, with the reverse for *n*-type MOSFETs. This difference in charges creates a migration of charges and therefore a deletion region is formed. At the electrode-semiconductor contact, there exists a voltage barrier called the contact resistance. This resistance is due to the metal-semiconductor contact and can be lowered by matching the work function of the electrode to the conduction level band of the semiconductor for *n*-type or the valence band for *p*-type. To measure the performance of MOSFETs many parameters are considered. Some include the threshold voltage representing the minimum voltage required at the gate to pass a current across the channel and the depletion region, V_T, the mobility, related to the current density, describes the ease of charge carrier displacement, μ. In addition, there's the ON current density I_{ON} which describes the current once saturated and the current leakage or OFF current I_{OFF}, describing the parasitic current which passes through without a gate voltage. All are typically monitored as benchmarking values. Although less common in Si MOSFETs, there are some imperfections which may undesirably affect the performance, which would require additional parameters. For instance, defects or unwanted doping can cause charge trapping and can lower the I_{ON} through charge recombination in the channel.

2.2.1. Thin Film Transistors

Although traditional inorganic MOSFETs have mobilities upwards of 5000 cm^2/Vs and are highly efficient,[47] recent interest has turned towards flexible electronics. Thin Film transistors have the capacity to be flexible, scalable and solution processable, perfect for dispensing in printing solutions.[16] Thin Film Transistors (TFT) and Organic TFTs (OTFT), use the same mechanisms as

MOSFETs. Their components include the source and drain electrode, the gate, the semiconductor and finally the dielectric to form the capacitance between the source and the gate (Figure 2.5).

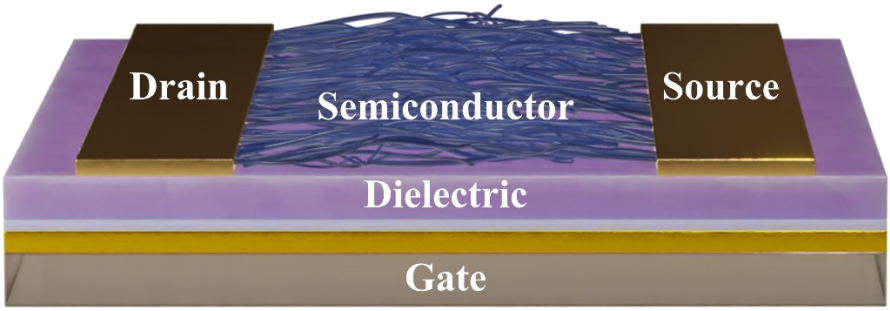

Figure 2.5) Components of an Organic Thin Film Transistor.

Recently, OTFTs have shown significant interest for unique applications such as RFID detectors[48], chemical and biological sensors.[49]

2.2.2. Models and Characterisation

Multiple models and model types exists to characterize and evaluate semiconductor devices, Figure 2.6 displays the hierarchy of transport model types. In these works, I have used the Shichman-Hodges[50] model (SH) model also known as the common MOSFET model, the Y-function method[51], and the novel Organic Virtual Source Emission Diffusion (OVSED) model which is an adaption of the virtual source model for organic transistors[52,53]. The first two of these models are considered compact models, they are very easy to implement but suffer from inaccuracies. The OVSED model is also compact model but allows for better fitting on organic field effect transistors.

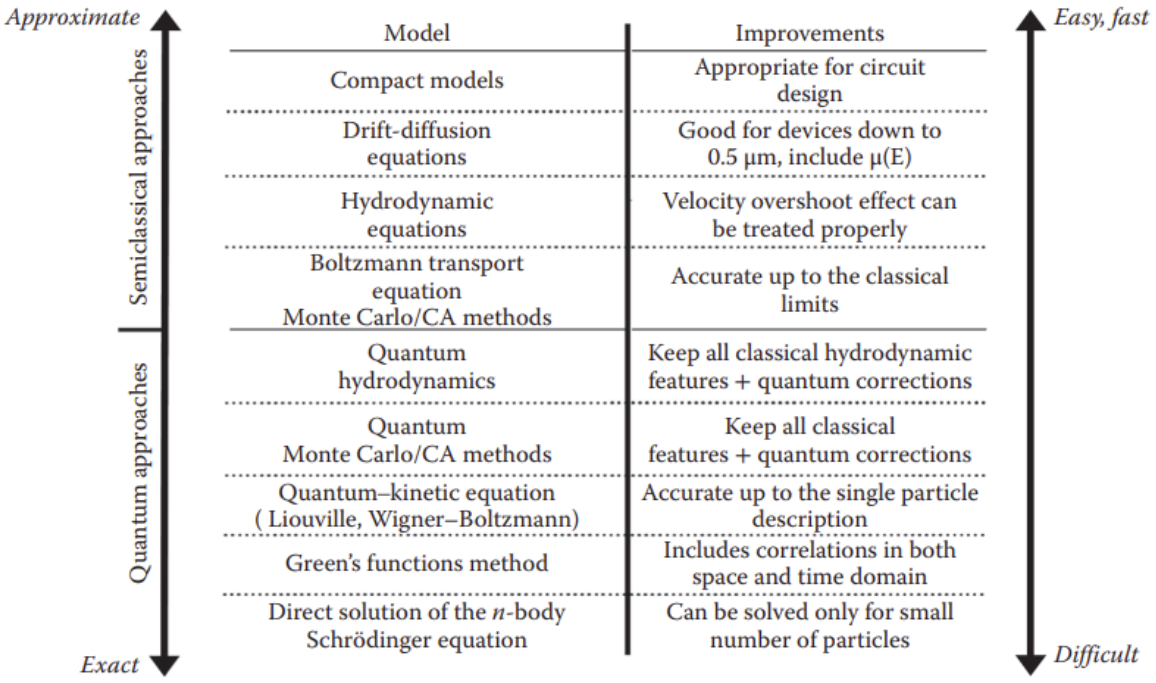

Model	Improvements
Compact models	Appropriate for circuit design
Drift-diffusion equations	Good for devices down to 0.5 μm, include μ(E)
Hydrodynamic equations	Velocity overshoot effect can be treated properly
Boltzmann transport equation Monte Carlo/CA methods	Accurate up to the classical limits
Quantum hydrodynamics	Keep all classical hydrodynamic features + quantum corrections
Quantum Monte Carlo/CA methods	Keep all classical features + quantum corrections
Quantum–kinetic equation (Liouville, Wigner–Boltzmann)	Accurate up to the single particle description
Green's functions method	Includes correlations in both space and time domain
Direct solution of the *n*-body Schrödinger equation	Can be solved only for small number of particles

Figure 2.6) Illustration depicting the hierarchy of transport models, reproduced from the Handbook of Optoelectronic Device Modeling and Simulation[54].

To characterize OTFTs using any of these three models, two IV curves are typically analysed. The first, the output curve, consists of a sweeping source-drain voltage ($V_{DS} = V_D - V_S$) at a set V_{GS} (Figure 2.7b), the second is the transfer curve, which consists of a sweeping gate voltage ($V_{GS} = V_G - V_S$) at set V_{DS} (Figure 2.7a).

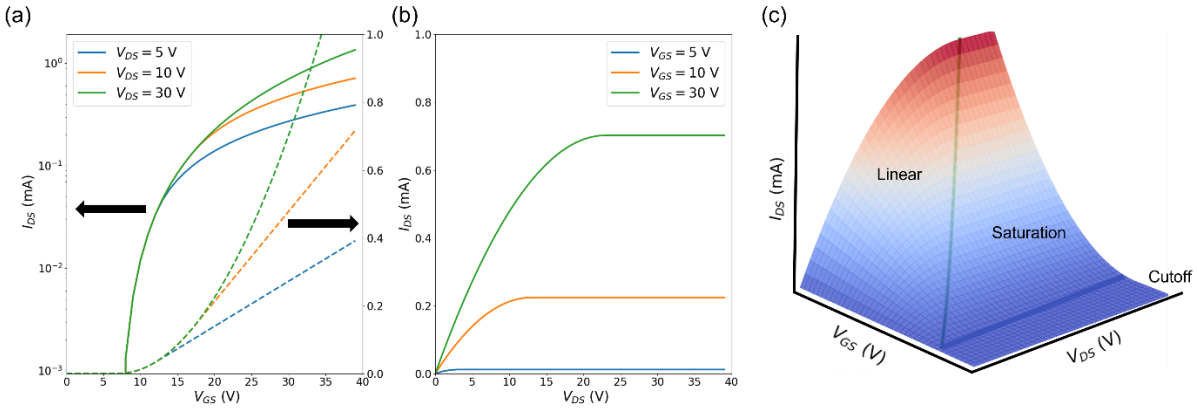

Figure 2.7) Simulated plots depicting the transfer (a) and output curves (b) obtained using the SH model without contact resistance, with V_t = 7 V, μ=5 cm^2/Vs, W=1 mm, L=20 μm and C_i= 1.06 x 10^{-8} F/cm^2 for an *n*-type device. A 3D plot, combining both the output and transfer curves with the different SH model regimes labeled.

Shichman-Hodges Model

The SH model separates the performance of the field effect transistor in three sections (Figure 2.7c). The cut-off regime where $|V_{GS}| < |V_T|$ and the current is $I_{DS} = 0$. The linear regime where $|V_{GS}| > |V_T|$ and $|V_{GD}| > |V_T|$, which indicates that $|V_{DS}| < |V_{GS} - V_T|$ for $V_{GD} = V_{GS} - V_{DS}$ and the current is $I_{DS_{lin}}$. In this regime, as the gate voltage increases, the charges keep accumulating at the gate which increases the current flow, and as the V_{DS} increases, the field effect across the depletion region increases, further increasing the current in a linear fashion. And finally, the saturation regime where$|V_{GS}| > |V_T|$ and $|V_{GD}| < |V_T|$, which indicates that $|V_{DS}| > |V_{GS} - V_T|$ and the current is $I_{DS_{sat}}$. In this regime, the drain is pinched and approaches a limit $|V_{DS}| = |V_{GS} - V_T|$, where at the end of the channel the inversion layer thins down, decreasing the charge density. In this regime the current becomes independent of V_{DS} as a result of this limit. The general equation for the conventional current in one direction across the channel is

$$I_{DS} = -W \cdot Q \cdot \nu \tag{2.6}$$

where Q [C/m^2] is the charge density, W [m] is the width of the channel and υ [m/s] is the charge velocity. The velocity can be linked to the electric field ε by assuming a linear relation and a constant called the mobility μ:

$$\nu = -\mu\varepsilon = \mu\frac{\partial V}{\partial x} \tag{2.7}$$

where x is the distance across the channel path. The charge density across the channel can be described using a charge control relation at a location on the channel:

$$Q = -C_i\big(V_{GS} - V_T - V(x)\big) \tag{2.8}$$

This assumes a constant threshold voltage and $V_{GS} - V(x) > V_T$. At the source $x = 0, V(0) = 0$, at the drain $x = L$ and $V(x) = V_{DS}$. By putting it all together, we obtain:

$$I_{DS} = W \cdot C_i\big(V_{GS} - V_T - V(x)\big) \cdot \mu \frac{\partial V}{\partial x} \tag{2.9}$$

$$\int_0^L I_{DS}\, dx = \int_0^{V_{DS}} W \cdot C_i\big(V_{GS} - V_T - V(x)\big) \cdot \mu dV \tag{2.10}$$

$$I_{DS_{lin}} = \frac{\mu V_{DS} W C_i}{L}\left(V_{GS} - V_T - \frac{V_{DS}}{2}\right) \tag{2.11}$$

And finally in the saturation regime, as previously mentioned $V_{DS} = V_{GS} - V_T$:

$$I_{DS_{sat}} = \frac{\mu W C_i}{2L}(V_{GS} - V_T)^2 \tag{2.12}$$

Where I_{DS} is the drain source current, L is the channel length and C_i is the capacitance density in F/m^2. Using the parallel plate model, $C_i = k_d \cdot E_o/t_t$, with k_d the dielectric constant, E_o the permittivity in vacuum in F/m, and t_t the thickness in m. To extract the mobility and threshold voltage, Equations 2.11 and 2.12 can be rearranged to the following forms

$$\mu_{sat} = \frac{2L}{W C_i}\left(\frac{\partial \sqrt{I_{DS}}}{\partial V_{GS}}\right)^2. \tag{2.13}$$

$$V_{T_{sat}} = V_{GS}(x - axis\ intercept) \tag{2.14}$$

$$\mu_{lin} = \frac{\partial I_{DS}}{\partial V_{GS}} \frac{L}{W V_{DS} C_i} \tag{2.15}$$

$$V_{T_{lin}} = V_{GS}(x - axis\ intercept) - V_{DS}/2 \tag{2.16}$$

To better compare the SH model to the OVSED model, I included a modified version which included contact resistance at the source and drain electrode each with a value of $R_C/2$.

$$I_{DS_{Lin}} = \frac{V_{DS}\left(V_{GS} - V_T - \frac{V_{DS}}{2}\right)}{R_C\left(\frac{1}{R_C\chi} + V_{GS} - \frac{V_{DS}}{2} - V_T\right)} \tag{2.17}$$

$$I_{DS_{Sat}} = \frac{-2R_C V_T + 4\chi^{-1} + 2V_{GS}R_C - 4\sqrt{\chi^{-1}(R_C V_{GS} + \chi^{-1} - R_C V_T)}}{{R_C}^2} \tag{2.18}$$

Where $\chi = \frac{W\mu C_i}{L}$ and both return to the regular SH model in the limit where R_C tends to 0. From these, a corrected value of mobility can be extracted, in the presence of contact resistance, using the transconductance g_m:

$$\mu_{lin} = \frac{L}{WC_i}\left(\frac{2V_{DS}{g_m}^{-1}\left(1 - \sqrt{1 - 2V_{DS}^{-1}g_m\alpha}\right) - 2\alpha}{\alpha^2}\right) \tag{2.19}$$

$$g_m = \frac{\partial I_{DS}}{\partial V_{GS}} \tag{2.20}$$

$$\alpha = R_C(2\Delta V_{Gt} - V_{DS}) \tag{2.21}$$

Where ΔV_{Gt} is a small voltage difference to compensate for the nonlinearity of the slope due to the contact resistance. For the saturation regime the mobility is:

$$\mu_{sat} = \left(\frac{\partial\sqrt{I_{DS_{sat}}}}{\partial V_{GS}}\right)^2 \frac{L}{WC_i}\frac{\left(2n + 4 - 4\sqrt{n+1}\right)(n+1)}{\left(\sqrt{n+1} - 1\right)^2} \tag{2.22}$$

Where $n = \Delta V_{Gt}R_C\chi$.

Y-Function Method

The Y-function method is a method unrelated to the SH model, used exclusively to extract the contact resistance, R_C, using the linear region of the transfer curves. The model is described as follows:

$$R_C = \frac{\partial S}{\partial V_{GS}}\left(\frac{\partial Y}{\partial V_{GS}}\right)^{-1} V_{DS} \tag{2.23}$$

$$Y = I_{DS}S \tag{2.24}$$

$$S = \frac{1}{\sqrt{g_m}} \tag{2.25}$$

Virtual Source Model

Unfortunately, the SH model often fails to provide proper parameter extraction when the charge transport becomes ballistic in small channel devices (~100 nm) and overestimates the magnitude of the channel's charge as a function of voltage. Additionally, it also does not account for the Drain Induced Barrier Lowering (DIBL), which is often seen though an increase in current for larger V_{DS} in transfer curves. The Virtual Source (VS) model[55] is a recent, compact semi-empirical model which addresses these faults using a non piecewise function, combining all three regimes, and reduces to the SH model at the limits. The VS model, named after the virtual source, a critical point on the channel marking the beginning of the channel and is located at the top of the electronic barrier. Although, it is important to note that the virtual source is not always at the physical start of the channel as the barrier is modulated by transport. Multiple iterations of the VS model exist, a simple version of the VS model above threshold ($V_{GS} > V_T$) can be described using the following equations:

$$I_{DS} = W \cdot Q_n \cdot F_{sat} \cdot \nu_{sat} \tag{2.26}$$

$$F_{sat} = \frac{V_{DS}}{V_{DSAT}[1 + (V_{DS}/V_{DSAT})^{\beta}]^{1/\beta}} \tag{2.27}$$

$$Q_n = -C_i(V_{GS} - \Psi) \tag{2.28}$$

$$\Psi = V_T - \delta V_{DS} \tag{2.29}$$

$$V_{DSAT} = \frac{\nu_{sat} L}{\mu}. \tag{2.30}$$

F_{sat} is an empirical function that facilitates a smooth transition from the linear, where the charge velocity is dominated by $\mu V_{DS}/L$, to the saturation regime, where the charge velocity is dominated by high-field bulk saturation velocity, $\nu_{sat} \approx \frac{\mu}{2L}(V_{GS} - V_T)$. The β is a fitting parameter, typically between 1.4 and 1.8 for Si MOSFETs and the voltage at the intersection of the two regimes is V_{DSAT}. The charge function, Q_n contains a modified threshold voltage, Ψ which accounts for DIBL using a linear reduction constant δ. To obtain the full curve, from bellow to above the threshold the charge function becomes:

$$Q_n = -m_C C_G V_{temp}\, ln\left[1 + e^{(V_{GS} - \Psi)/m_C V_{temp}}\right] \tag{2.31}$$

Where $C_G = (C_i^{-1} + C_S^{-1})^{-1}$ is the gate capacitance which approaches the smallest capacitance between the oxide capacitance, C_i, and the semiconductor's capacitance, C_S, and $m_C = 1 + C_S/C_i$. Finally, the thermal voltage V_{temp} can be expressed in terms of the temperature T, the Boltzmann constant k_B and the elementary charge q, $V_{temp} = k_B T/q$.

This model has had many adaptions, for instance for low temperature applications[56] and in small channel carbon nanotube transistors[57] among others, each showing good fittings on the fitted measurements. More recently, an organic version of the VS model was adapted for organic transistors.[53]

Organic Virtual Source Emission Diffusion model

The OVSED model was first developed by Blawid, Lima[53] as an adaption to the VS model to account for the differences between the inorganic and organic semiconductors, such as higher density of charge traps. An improved OVSED model was developed by Blawid and myself in our joint papers[52,58]. The complete model can be summarized by the following equations where J_{DS} and Q_{free} are the one-dimensional drain current density and the density of total charge of the free charges in C/cm^2.

$$J_{DS} = I_{DS}/W = v_{sat} Q_{free} F_{sat} \tag{2.32}$$

$$Q_{free} = q\sigma_v \cdot \left(\frac{Q_{tot}}{q\sigma_T}\right)^l \tag{2.33}$$

$$Q_{tot} = C_i V_{temp}\, ln\left[1 + exp\left(\frac{\Psi - V_{GS}}{nV_{temp}}\right)\right] \tag{2.34}$$

$$\Psi = V_T + |\delta| V_{DS} \tag{2.35}$$

The density of valence charge carriers and traps are denoted by σ_V and σ_T, both in cm^{-2}. Equation 2.35 is a variable threshold voltage dependant on the source drain voltage (V_{DS}). This accounts for DIBL similarly to the standard VS model, however, in OTFTs the strong accumulation is shifted to a higher electric field for larger V_{DS}, thus δ becomes a drain induced barrier increase variable. The l variable is a unitless value describing the exponential tail of the density of trap states in equation 2.33. The n is a gate coupling factor or non-ideality factor which determines the effectiveness of the gate bias to control the semiconductor charge. The high-field bulk saturation velocity $v_{sat} = \mu_d V_{temp}/\lambda_f$ is dependant on the drift mobility μ_d and the mean free path λ_f. This along with the density of valence charge carriers and traps is included in the linear current density $J_T = q\sigma_V(C_i n V_{temp}/q\sigma_T)^l$ to simplify fitting the model to measurements using the method of least squares. The transitional function F_{sat} takes a different form in this adaption:

$$F_{sat} = \frac{1 - e^{-V_{DS}/V_{temp}}}{1 + 2t + e^{-V_{DS}/V_{temp}}} \tag{2.36}$$

$$t = \frac{2\lambda}{m^2(1-\eta^2)}\left[(1 - m\eta)e^{-m(1-\eta)} - 1 + m\right] \tag{2.37}$$

$$\eta = 1 - tanh\left(\frac{V_{DS}}{mV_{temp}}\right) \tag{2.38}$$

$$m = \frac{V_{GT}/V_{temp}}{1 + \sqrt{\frac{2V_{GT}}{V_{gcrit}}}} \tag{2.39}$$

$$V_{GT} = Q_{Tot}/C_i \tag{2.40}$$

where t is a unitless unit describing the critical length for diffusion, V_{gcrit} is the critical voltage for v_{sat} and $\lambda = L_G/\lambda_f$ with L_G being the gate length. Recently, it has been discovered that in OTFTs the contact resistance is dependent on the drain voltage causing an s-shape in the output curve[59]. To compensate for the s-shape originating from devices a voltage dependence resistance replaces the typical contact resistance:

$$R_C = 2R_0 + \frac{R_{max} - R_0}{2} \cdot \left[1 - \tanh\left(\frac{V_{DS} - V_0}{V_{tun}}\right)\right] \tag{2.41}$$

The values R_O and R_{max} describe the minimum and maximum resistance values while the hyperbolic tangent function allows the swift change from the maximum to the minimum. The parameter V_0 is the source-drain voltage when the switch happens and V_{tun} describes the smoothing of the transition in volts, a bigger V_{tun} describes a slow transition and a smaller V_{tun} describes a quick transition. The model contains a total of 11 model parameters, J_T, δ, l, n, V_{gcrit}, $V_{tun,}$ R_O, R_{max} V_T and λ since V_{DS}, V_{GS}, T and W were controlled and the parasitic leakage current I_{DLeak} was added to the final current value.

2.3. References

1. Simon, M. S. & Kwok, K. N. Physics of Semiconductor Devices, 3rd Edition. (Wiley, 2006).
2. NCN Nanoelectronics: Simulation Tools for Education. Preprint at https://nanohub.org/resources/3584 (2007).
3. Organic Electronics: Materials, Manufacturing and Applications. (Wiley, 2006).
4. Melville, O. A., Lessard, B. H. & Bender, T. P. Phthalocyanine-Based Organic Thin-Film Transistors: A Review of Recent Advances. ACS Appl Mater Interfaces 7, 13105–13118 (2015).
5. Brixi, S. et al. Air and temperature sensitivity of n-type polymer materials to meet and exceed the standard of N2200. Sci Rep 10, 1–10 (2020).
6. Ray, B., Baradwaj, A. G., Boudouris, B. W. & Alam, M. A. Defect Characterization in Organic Semiconductors by Forward Bias Capacitance–Voltage (FB-CV) Analysis. The Journal of Physical Chemistry C 118, 17461–17466 (2014).
7. Kumanek, B. & Janas, D. Thermal conductivity of carbon nanotube networks: a review. J Mater Sci 54, 7397–7427 (2019).
8. Li, M.-K. et al. Electroluminescence from Single-Walled Carbon Nanotubes with Quantum Defects. ACS Nano 16, 11742–11754 (2022).
9. Blackburn, J. L. Semiconducting Single-Walled Carbon Nanotubes in Solar Energy Harvesting. ACS Energy Lett 2, 1598–1613 (2017).
10. Walters, D. A. et al. Elastic strain of freely suspended single-wall carbon nanotube ropes. Appl Phys Lett 74, 3803–3805 (1999).
11. Arnold, M. S. et al. Recent developments in the photophysics of single-walled carbon nanotubes for their use as active and passive material elements in thin film photovoltaics. Phys. Chem. Chem. Phys. 15, 14896–14918 (2013).
12. Muguruma, H., Hoshino, T. & Nowaki, K. Electronically Type-Sorted Carbon Nanotube-Based Electrochemical Biosensors with Glucose Oxidase and Dehydrogenase. ACS Appl Mater Interfaces 7, 584–592 (2015).
13. Yoon, B., Liu, S. F. & Swager, T. M. Surface-Anchored Poly(4-vinylpyridine)–Single-Walled Carbon Nanotube–Metal Composites for Gas Detection. Chemistry of Materials 28, 5916–5924 (2016).
14. Schroeder, V., Savagatrup, S., He, M., Lin, S. & Swager, T. M. Carbon Nanotube Chemical Sensors. Chem Rev 119, 599–663 (2019).
15. Mirka, B. et al. Contact Engineering in Single-Walled Carbon Nanotube Thin-Film Transistors: Implications for Silane-Treated SiO2 Substrates. ACS Appl Nano Mater 5, 12487–12495 (2022).

16. Cao, C., Andrews, J. B. & Franklin, A. D. Completely Printed, Flexible, Stable, and Hysteresis-Free Carbon Nanotube Thin-Film Transistors via Aerosol Jet Printing. Adv Electron Mater 3, 1700057 (2017).

17. Schnorr, J. M. & Swager, T. M. Emerging Applications of Carbon Nanotubes. Chemistry of Materials 23, 646–657 (2011).

18. Zhang, R. et al. Growth of Half-Meter Long Carbon Nanotubes Based on Schulz–Flory Distribution. ACS Nano 7, 6156–6161 (2013).

19. Dresselhaus, M. S., Dresselhaus, G. & Saito, R. Physics of carbon nanotubes. Carbon N Y 33, 883–891 (1995).

20. Dresselhaus, M. S., Dresselhaus, G., Saito, R. & Jorio, A. Raman spectroscopy of carbon nanotubes. Phys Rep 409, 47–99 (2005).

21. Nikolaev, P. et al. Gas-phase catalytic growth of single-walled carbon nanotubes from carbon monoxide. Chem Phys Lett 313, 91–97 (1999).

22. Arora, N. & Sharma, N. N. Arc discharge synthesis of carbon nanotubes: Comprehensive review. Diam Relat Mater 50, 135–150 (2014).

23. Journet, C. et al. Large-scale production of single-walled carbon nanotubes by the electric-arc technique. Nature 388, 756–758 (1997).

24. Su Kim, K. et al. Large-scale production of single-walled carbon nanotubes by induction thermal plasma. J Phys D Appl Phys 40, 2375 (2007).

25. Wang, H. & Bao, Z. Conjugated polymer sorting of semiconducting carbon nanotubes and their electronic applications. Nano Today 10, 737–758 (2015).

26. Green, A. A. & Hersam, M. C. Nearly Single-Chirality Single-Walled Carbon Nanotubes Produced via Orthogonal Iterative Density Gradient Ultracentrifugation. Advanced Materials 23, 2185–2190 (2011).

27. Zheng, Y. et al. Quantum Light Emission from Coupled Defect States in DNA-Functionalized Carbon Nanotubes. ACS Nano 15, 10406–10414 (2021).

28. Blanch, A. J., Quinton, J. S. & Shapter, J. G. The role of sodium dodecyl sulfate concentration in the separation of carbon nanotubes using gel chromatography. Carbon N Y 60, 471–480 (2013).

29. Flavel, B. S., Moore, K. E., Pfohl, M., Kappes, M. M. & Hennrich, F. Separation of Single-Walled Carbon Nanotubes with a Gel Permeation Chromatography System. ACS Nano 8, 1817–1826 (2014).

30. Samanta, S. K. et al. Conjugated Polymer-Assisted Dispersion of Single-Wall Carbon Nanotubes: The Power of Polymer Wrapping. Acc Chem Res 47, 2446–2456 (2014).

31. Rother, M. et al. Aerosol-Jet Printing of Polymer-Sorted (6,5) Carbon Nanotubes for Field-Effect Transistors with High Reproducibility. Adv Electron Mater 3, 1700080 (2017).

32. Nish, A., Hwang, J.-Y., Doig, J. & Nicholas, R. J. Highly selective dispersion of single-walled carbon nanotubes using aromatic polymers. Nat Nanotechnol 2, 640–646 (2007).

33. Fong, D. & Adronov, A. Recent developments in the selective dispersion of single-walled carbon nanotubes using conjugated polymers. Chem. Sci. 8, 7292–7305 (2017).

34. Lei, T. et al. Low-voltage high-performance flexible digital and analog circuits based on ultrahigh-purity semiconducting carbon nanotubes. Nat Commun 10, 2161 (2019).

35. Ouyang, J. et al. Sorting of Semiconducting Single-Walled Carbon Nanotubes in Polar Solvents with an Amphiphilic Conjugated Polymer Provides General Guidelines for Enrichment. ACS Nano 12, 1910–1919 (2018).

36. Wang, H. et al. Solvent Effects on Polymer Sorting of Carbon Nanotubes with Applications in Printed Electronics. Small 11, 126–133 (2015).

37. Li, Z. et al. Raman microscopy mapping for the purity assessment of chirality enriched carbon nanotube networks in thin-film transistors. Nano Res 8, 2179–2187 (2015).

38. Rice, N. A., Subrahmanyam, A. V, Laengert, S. E. & Adronov, A. The effect of molecular weight on the separation of semiconducting single-walled carbon nanotubes using poly(2,7-carbazole)s. J Polym Sci A Polym Chem 53, 2510–2516 (2015).

39. Ozawa, H., Ide, N., Fujigaya, T., Niidome, Y. & Nakashima, N. One-pot Separation of Highly Enriched (6,5)-Single-walled Carbon Nanotubes Using a Fluorene-based Copolymer. Chem Lett 40, 239–241 (2011).

40. Beaupré, S., Boudreault, P.-L. T. & Leclerc, M. Solar-Energy Production and Energy-Efficient Lighting: Photovoltaic Devices and White-Light-Emitting Diodes Using Poly(2,7-fluorene), Poly(2,7-carbazole), and Poly(2,7-dibenzosilole) Derivatives. Advanced Materials 22, E6–E27 (2010).

41. Li, J. & Grimsdale, A. C. Carbazole-based polymers for organic photovoltaic devices. Chem. Soc. Rev. 39, 2399–2410 (2010).

42. Sotzing, G. A. et al. Multiply Colored Electrochromic Carbazole-Based Polymers. Chemistry of Materials 9, 1578–1587 (1997).

43. Ding, J. et al. Enrichment of large-diameter semiconducting SWCNTs by polyfluorene extraction for high network density thin film transistors. Nanoscale 6, 2328–2339 (2014).

44. Gomulya, W. et al. Semiconducting Single-Walled Carbon Nanotubes on Demand by Polymer Wrapping. Advanced Materials 25, 2948–2956 (2013).

45. Itkis, M. E., Perea, D. E., Jung, R., Niyogi, S. & Haddon, R. C. Comparison of Analytical Techniques for Purity Evaluation of Single-Walled Carbon Nanotubes. J Am Chem Soc 127, 3439–3448 (2005).

46. Hu, B. et al. A Survey on Recent Advances of Medium Voltage Silicon Carbide Power Devices. in 2018 IEEE Energy Conversion Congress and Exposition (ECCE) 2420–2427 (2018). doi:10.1109/ECCE.2018.8558451.

47. Choi, J. Y. & Lee, S. Y. Comprehensive review on the development of high mobility in oxide thin film transistors. Journal of the Korean Physical Society 71, 516–527 (2017).

48. Fadlallah, M., Billiot, G., Eccleston, W. & Barclay, D. DC/AC unified OTFT compact modeling and circuit design for RFID applications. Solid State Electron 51, 1047–1051 (2007).

49. Comeau, Z. J. et al. On-the-Spot Detection and Speciation of Cannabinoids Using Organic Thin-Film Transistors. ACS Sens 4, 2706–2715 (2019).

50. Shichman, H. & Hodges, D. A. Modeling and simulation of insulated-gate field-effect transistor switching circuits. IEEE J Solid-State Circuits 3, 285–289 (1968).

51. Liu, C., Xu, Y. & Noh, Y.-Y. Contact engineering in organic field-effect transistors. Materials Today 18, 79–96 (2015).

52. Dallaire, N. J., Brixi, S., Claus, M., Blawid, S. & Lessard, B. H. Benchmarking contact quality in N-type organic thin film transistors through an improved virtual-source emission-diffusion model. Appl Phys Rev 9, 11418 (2022).

53. Lima, A. A. & Blawid, S. Modeling organic thin-film transistors based on the virtual source concept: A case study. Solid State Electron 161, 107639 (2019).

54. Roy Pik, E. Handbook of Optoelectronic Device Modeling and Simulation. vol. 2 (CRC Press, 2018).

55. Lundstrom, M. S. Transistors! (World Scientific Publishing Company, 2022).

56. Chakraborty, W., Ni, K., Smith, J., Raychowdhury, A. & Datta, S. An Empirically Validated Virtual Source FET Model for Deeply Scaled Cool CMOS. in 2019 IEEE International Electron Devices Meeting (IEDM) 39.4.1-39.4.4 (2019). doi:10.1109/IEDM19573.2019.8993666.

57. Lee, C. .-S., Pop, E., Franklin, A. D., Haensch, W. & Wong, H. .-S. P. A Compact Virtual-Source Model for Carbon Nanotube FETs in the Sub-10-nm Regime—Part I: Intrinsic Elements. IEEE Trans Electron Devices 62, 3061–3069 (2015).

58. Blawid, S., Dallaire, N. J. & Lessard, B. H. Self-Consistent Extraction of Mobility and Series Resistance: A Hierarchy of Models for Benchmarking Organic Thin-Film Transistors. IEEE Journal on Flexible Electronics 1, 114–121 (2022).

59. Liu, C. et al. Universal diffusion-limited injection and the hook effect in organic thin-film transistors. Sci Rep 6, 29811 (2016).

Chapter 3: Benchmarking Contact Quality in N-type Organic Thin Film Transistors through an Improved Virtual-Source Emission-Diffusion Model

Context

After completing my Bachelor's, I decided to continue my work on the organic virtual-source emission diffusion (OVSED) model and use it to benchmark N2200 based OTFTs with various electrode interlayers. Traditionally, due to its air stability and optimal electrical conduction, gold was used as an electrode material in our group. However, it was hypothesized that the use of interlaying metals, between the electrode and the semiconductor, with work functions closer to the LUMO level for *n*-type semiconductors and HOMO level for *p*-type semiconductors, could be used to lower the contact resistance by lowering the energy gap. For this study, devices with three different interlayer types of various thicknesses, none, chromium, and manganese were fabricated. I characterised them using the SH model and the Y-function method to extract the mobility, threshold voltage and the contact resistance. I then fitted the curves using the OVSED model. The extracted parameters matched those extracted from the classically used, SH and Y-function methods but with a better fitting. The work concluded by finding an optimal interlayer type and thickness. This work was published in Applied Physics Reviews on the 22nd of February 2022 and served as proof of the viability of the improved OVSED model.

Contributions

In this work, I performed all the device characterization via the SH model and the Y function method. I fitted the OVSED model to the curves using a MATLAB code I improved from Dr Blawid. I measured the performance of most of the devices. I derived the SH model with contact resistance, along with the mobility extraction with contact resistance. I ensured the stability of the

fit parameters while using the least squares algorithm via repeated runs with different starting values. I authored the manuscript with other co-authors providing editorial contributions. This work was supervised by Karin Hinzer and Benoit Lessard. The following chapter contains minor changes compared to the published version.

3.1. Abstract

Due to nonideal behavior, current organic thin film transistor technologies lack the proper models for essential characterization and thus suffer from a poorly estimated parameter extraction critical for circuit design and integration. Organic thin film transistors are often plagued by contact resistance which is often less problematic in inorganic transistors; consequently, common models used for describing inorganic devices do not properly work with organic thin film transistors. In this work we fabricate poly{[N,N′-bis(2-octyldodecyl)-naphthalene-1,4,5,8-bis(dicarboximide)-2,6-diyl]-alt-5,5′-(2,2′bithiophene)} based organic thin film transistors with reduced contact resistance through the introduction of metallic interlayers between the semiconductor and gold contacts. The addition of 10 nm thick manganese interlayer provides optimal OTFT device performance with the lowest level of contact resistance. Improved organic thin film transistors were characterized using an improved organic virtual source emission diffusion model, which provides a simple and effective method to extract the critical device parameters. The organic virtual-source emission diffusion model led to nearly perfect prediction using effective gate voltages and a gate dependent contact resistance, providing a significant improvement over common metal–oxide–semiconductor field-effect transistor models such as the Shichman-Hodges model.

3.2. Introduction

Organic thin film transistors (OTFT) are solid state switches based on organic semiconductors such as conjugated polymers, which can be manufactured at a low cost using roll-to-roll printing techniques on flexible substrates.[1–3] Unlike conventional metal–oxide–semiconductor field-effect transistors (MOSFETs), OTFTs often suffer from non-ideal device performance due to limited charge injection into the device channel[4]; which often leads to high contact resistance (R_C) and poor estimation of charge mobility (μ) or threshold voltage (V_T).[5–9] The gradual channel approximation (GCA)[10] employed in the Shichman Hodges (SH) model[11], is widely used to characterize MOSFETs however they are inefficient in characterizing OTFTs. This inefficiency stems from the assumptions in the SH model which are often false in OTFTs. Such assumptions include a zero-channel thickness, the μ is independent of the gate or source-drain voltage and there is negligible R_C.[5,12] Therefore, we require a new model that accounts for R_C that is directly related to the energy gap. This gap is between the electrode work function and the semiconductor's highest occupied molecular orbital (HOMO), for hole transport materials, or the lowest unoccupied molecular orbital (LUMO), for electron transport materials.[4,13,14]

Poly{[N,N′-bis(2-octyldodecyl)-naphthalene-1,4,5,8-bis(dicarboximide)-2,6-diyl]-alt-5,5′-(2,2′bithiophene)} (P(NDI2OD-T2)) also known as N2200, has found application in air stable solution processed n-type OTFTs.[13] The addition of an electrode interlayer with a more favourable work function can reduce the R_C and improve apparent values of V_T and μ.[15] In this study, we employ the use of chromium (Cr) and manganese (Mn) as electrode interlayers to reduce the R_C of P(NDI2OD-T2)-based OTFTs as their conductivity is too low to be used by themselves as electrode materials.[16–19] Finally, we characterize the resulting devices using an improved and superior OVSED model compared to the classic SH model. This model is applied to P(NDI2OD-

T2) but could equally be applied to naphthalenetetracarboxylic diimide (NDI)[20,21], phthalocyanines[22,23], oligoacene[24,25] or even carbon nanotube devices[26,27].

3.3. Results and Discussion

3.3.1. Choice of Interlayer

We investigated the effect of different contact interlayers in P(NDI2OD-T2)-based OTFTs in a bottom gate top contact configuration (**Figure 3.1**).

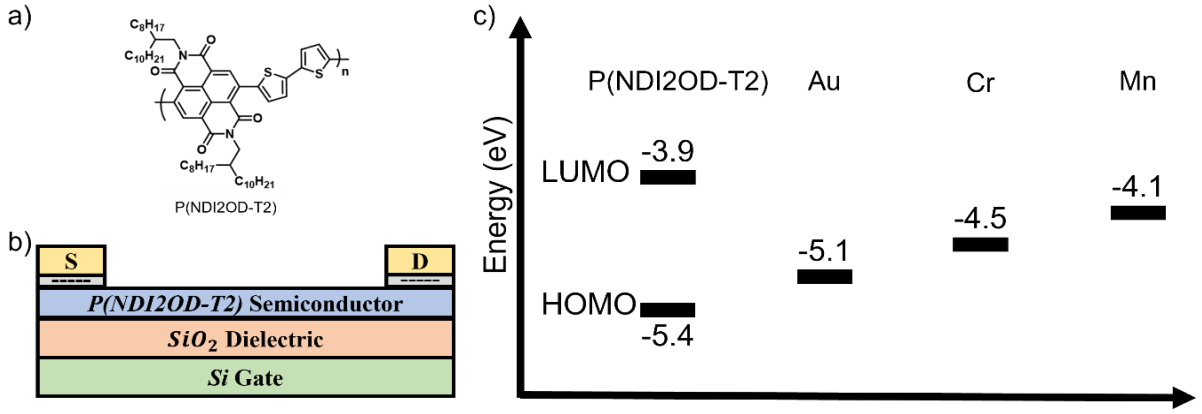

Figure 3.1) *a) A diagram of the P(NDI2OD-T2) molecule. b) A side-view schematic of the organic thin film transistors (OTFT) with the Si gate, SiO_2 dielectric, the P(NDI2OD-T2) semiconductor and source (S) and drain (D) contacts with the interlayer in gray. c) A visual representation of the energy levels for the lowest unoccupied molecular orbital (LUMO), the highest occupied molecular orbital (HOMO) levels of the semiconductor and the work functions levels of the contact metals.*

The source and drain contacts, including the interlayers, were deposited through sequential physical vapour deposition steps where the final layer was gold to increase the electrode conductivity. It has been reported that the addition of the interlayer increases the effective work function of the electrode as a whole, reducing the barrier for charge injection into the LUMO level of the semiconductor, leading to a drop in R_C and improvement in overall device performance.[17–19,28] The LUMO energy level of P(NDI2OD-T2), has been reported to be -3.9 eV.[29] Therefore, we

selected Cr and Mn interlayers with known work functions of -4.5 eV and -4.1 eV respectively compared to Au with a work function of -5.1 eV (**Figure 3.1c**).[15]

To elucidate the effect of the interlayer on the OTFT performance we report characteristic output curves and transfer curves (**Figure 3.2**) in addition, we tabulate the extracted electron mobility (μ_e) in saturation regime, threshold voltage (V_T) and R_C, in **Table 3.1**. A summary of the parameters is also displayed in box plots in **Figure 3.3**. As seen in all the transfer curves, the transistors experienced an ambipolarity, not uncommon for P(NDI2OD-T2) semiconductor[13] and have rather small hysteresis. The μ_e was extracted between 0.001 to 0.015 cm^2/Vs, similar to previous reports of OTFTs fabricated using P(NDI2OD-T)[29,30] and found to seldomly significantly vary between device configuration and predominantly stay within the associated error. This is to be expected, as it is well known that the intrinsic μ_e is primarily determined by the semiconductor microstructure and its morphology and not by R_C.[31] However, the extracted apparent μ_e is influenced by R_C, this influence is discussed in the supporting information and in **Figure 3.S1** and is negligible for optimized contacts. For the μ_e extracted in the linear regime the influence has been discussed in detail and is in general not small[32]. The V_T, which is a function of the ease of turning on the device, extracted using the SH model, decreased from 19 V to as low as 9.8 V with the addition of a 10 nm interlayer of Cr or Mn (**Table 3.1**), with the latter having less variability in their V_Ts (**Figure 3.3**). In addition, the devices with the Mn interlayers display more ideal IV curves with a clear saturating current and less ambipolarity. We then extracted the device's total R_C using the Y-function method,[4] and found that the use of both interlayers led to devices with decreased R_C, which is consistent with the reduced energetic barrier between the LUMO of P(NDI2OD-T2) and the work function of the contact electrodes.[14, 25] Moreover, the variability in R_C for Mn/Au based devices was significantly reduced compared to the use of bare Au or when using Cr/Au

contacts (**Figure 3.3**). In addition to the 10 nm interlayer parameters, a comparison for a 4 nm interlayer of Cr or Mn is presented in **Figure 3.S2** and **Table 3.S1** with similar results to 10 nm but to less of an extent given the lowered thickness. These results suggest Mn as a promising candidate for the improvement of performance of P(NDI2OD-T2)-based OTFT devices.

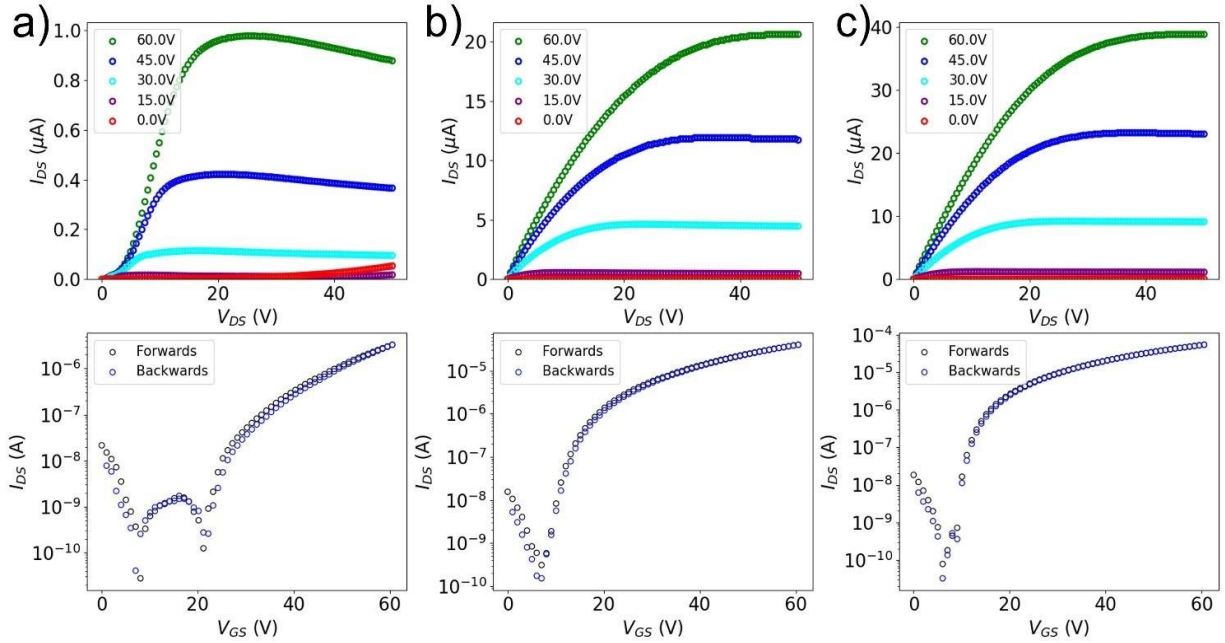

Figure 3.2) *Characteristic output curves of Drain-Source current (I_{DS}) versus Drain-Source voltage (V_{DS}) at a set gate voltage (top) and transfer curves of Drain-Source current (I_{DS}) versus Gate-Source voltage (V_{GS}) with V_{DS} = 50 V (bottom) for P(NDI2OD-T2) bottom gate top contact OTFT devices with gold electrodes and a) no interlayers, b) 10nm of chromium interlayer, c) 10nm of manganese interlayer as the top contacts. All measurements performed in a N_2 environment.*

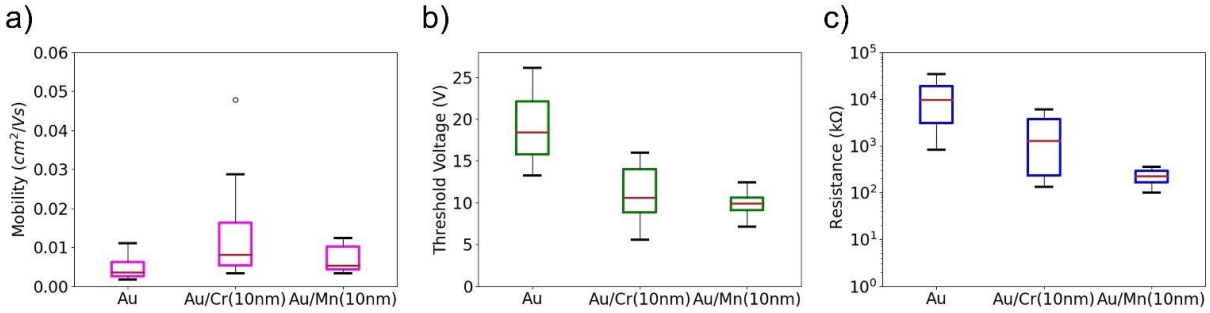

Figure 3.3) *Electrical properties for the saturation region of P(NDI2OD-T2) bottom gate top contact OTFT devices with no interlayers (Au), 10 nm of chromium (Au/Cr(10nm)) and 10 nm of manganese (Au/Mn(10nm)). The graphs display a) the corresponding electron mobility (μ_e), b) the threshold voltages (V_T), c) the contact resistance (R_C). Data is shown in box plots, where the box indicates the interquartile range, the horizontal line (within the box) is the median, vertical lines indicate the difference between the 5th and 95th percentile, with empty circles indicating outliers. All measurements were performed in a N_2 environment.*

Contact[a)]	$\mu_{e\ b)}$ (cm^2/Vs)	$V_{T\,b)}$ (V)	$R_{C\,c)}$ (kΩ)
Au	$(4.6\pm0.8)\times 10^{-3}$	19 ± 1	$(1.3\pm0.3)\times 10^{4}$
Au/Cr(10nm)	$(1.3\pm0.3)\times 10^{-2}$	11.0 ± 0.9	$(2.2\pm0.6)\times 10^{3}$
Au/Mn(10nm)	$(6.7\pm0.7)\times 10^{-3}$	9.8 ± 0.3	$(2.3\pm0.9)\times 10^{2}$

Table 3.1) *a) N2200 based bottom gate top contact OTFT with thermally evaporated electrodes with interlayers: where Au/X(Ynm), where Au = are the gold contacts, X is the type of interlayer and Y is the thickness of that interlayer. All measurements performed in a N_2 environment. b) Electron mobility, μ_e and threshold voltage, V_T obtained from saturation region of the transfer curve based on the Shichman-Hodges model. c)Contact resistance, RC extracted from the Y-function method[4] and the linear transfer curves.*

3.3.2. Effect of Thickness

Since the devices with a Mn interlayer exhibited smaller parameter variability, we further characterized this system by optimizing the thicknesses of the Mn interlayer. The corresponding device performance parameters are displayed in box plot in **Figure 3.4** and their averages with associated error are found in **Table 3.2**. The R_C decreases by almost one order of magnitude for an interlayer ≥10 nm when compared to 4 nm and two orders of magnitude when compared to no interlayers (**Table 3.2**). There is also a clear trend, which seems to saturate, where a thicker Mn interlayer leads to the lowest R_C. However, there is a minimum V_T of 9.8 V at 10 nm of Mn, which

increases for 25 nm of Mn (**Table 3.2**). The devices containing 0 nm, 4 nm and 10 nm of Mn interlayer have similar μ_e values, however, when the thickness reached 25 nm the μ_e increased by roughly an order of magnitude but with significantly more variability (**Table 3.2**). Part of this increase should be caused by the reduced R_C, since the apparent μ_e is reduced from its intrinsic values due to the R_C. However, one should note that for non-ideal electrical characteristics, the SH equations no longer hold and the μ_es are poorly estimated.[8,15] Nonetheless, the simple addition of the Mn interlayer significantly improves the device performance. However, the benefit of a reduced R_C at 25 nm of Mn comes at the cost of a greater V_T when compared to 10 nm. This compromise could stem from the heightened conductivity of gold compared to manganese.[17,19]

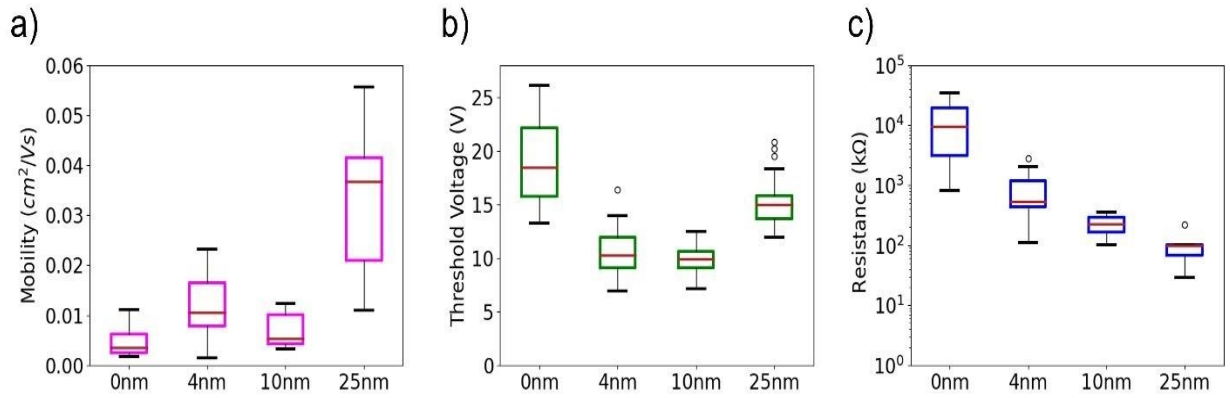

Figure 3.4) *Electrical properties for the saturation region of P(NDI2OD-T2) bottom gate top contact OTFT devices with no interlayers (0 nm) with 4 nm, 10 nm, and 25 nm of manganese. The graphs display the corresponding electron mobility (μ_e), b) threshold voltages (V_T), and c) contact resistances (R_C) . Data is shown in box plots, where the box indicates the interquartile range, the horizontal line (within the box) is the median, vertical lines indicate the difference between the 5th and 95th percentile, with empty circles indicating outliers. All measurements performed in a N_2 environment.*

Table 3.2) Electrical Characterization of N2200 based OTFTs with varying interlayer thickness.

Contact[a)]	μ_e [b)] (cm^2/Vs)	V_T[b)] (V)	Contact Resistance (kΩ)[c)]
Au/Mn(0nm)	$(4.6\pm0.8)\times 10^{-3}$	19 ± 1	$(1.3\pm0.3)\times 10^4$
Au/Mn(4nm)	$(1.2 \pm 0.1)\times 10^{-2}$	10.0 ± 0.6	$(9\pm2)\times 10^2$
Au/Mn(10nm)	$(6.7\pm0.7)\times 10^{-3}$	9.8 ± 0.3	$(2.3\pm0.9)\times 10^2$

Au/Mn(25nm)	$(3.094\pm0.006)\times 10^{-2}$	15.3 ± 0.4	$(1.1\pm0.5)\times 10^{2}$

Table 3.2) *a) N2200 based bottom gate top contact OTFT with thermally evaporated electrodes with interlayers: where Au/X(Ynm), where Au = are the contacts, Mn is manganese interlayer and Y is the thickness of that interlayer. All measurements performed in a N_2 environment. b) Electron mobility, μ_e and threshold voltage, V_T obtained from saturation region of the transfer curve based on the Shichman-Hodges model. c)Contact resistance, RC extracted from the Y-function method[4] and the linear transfer curves.*

3.3.3. Improved OVSED Model

Although the SH model equations are often used to characterize OTFTs, as it was observed in the previous section, these equations often fail to fully describe their behavior causing poor estimation of the device's μ_e and V_T.[5,7–9] Since OTFTs exhibit lower μ_es and a lower charge concentration compared to inorganic semiconductors, it has been theorized that charges are being injected into the channel through the electrodes instead of by polarization, thus the choice of electrodes highly influences the device's performance.[33] Lima et al. proposed the organic virtual source emission diffusion model (OVSED) that utilizes the virtual source concept to describe the IV behavior of the OTFT as a continuous curve rather than two equations for the linear and saturation regime.[34] Originally, the restricted rate of charge injection from the top of the energetic barrier was used in short-channel MOSFETs[35], but since the current at the virtual source is diffusive, the charge injection can be calculated using emission-diffusion (ED) theory and can be also applied to long-channel devices.[36,37] The OVSED model describes the device using 8 intrinsic parameters: V_T, current density (J_T), a model parameter influencing the V_T (δ), a unitless value describing the exponential tail of the density of trap states (l), a gate coupling factor (n), the critical voltage for velocity saturation of charge carriers (V_{gcrit}), the R_c and the ratio between the channel length and the mean free path (λ). The other parameters V_{DS}, V_{GS}, temperature (T) and channel width (W) are controlled and the drain leakage (I_{Dleak}), is treated as a constant and is manually fitted. The model is described in detail in the experimental section. In this study the OVSED model proposed by

Lima et al.[34] was used to model and characterize P(NDI2OD-T2) OTFTs. The black circles represent the experimental points while the solid red line (Top of **Figure 3.5**) and solid blue line (Top of **Figure 3.6**) represent the model fitting of characteristic output curves and the transfer curves, respectively. Under certain conditions the model performed quite well and represented the experimental data accurately (**Figure 3.5b**) however in other instances (**Figure 3.5 a** and **c**) we observe a drop in fitting accuracy for large V_{GS} values.

The OVSED model by Lima et al. can not properly represent OTFT devices that displayed an S-curve in the IV characteristics (**Figure 3.5a**), which is often a result of high or non-ohmic R_C.[14,33] It has been previously experimentally observed that R_C is in fact not constant and depends on the source-drain voltage.[38] An empirical adaption was employed to change the R_C from a maximum value to a minimum value. Therefore, we modified the OVSED model to include R_C which is dependent on V_{DS} as depicted in **Equation 3.1**.

$$R_C = 2R_0 + \frac{R_{max} - R_0}{2} \cdot \left[1 - \tanh\left(\frac{V_{DS} - V_0}{V_{tun}}\right)\right] \tag{3.1}$$

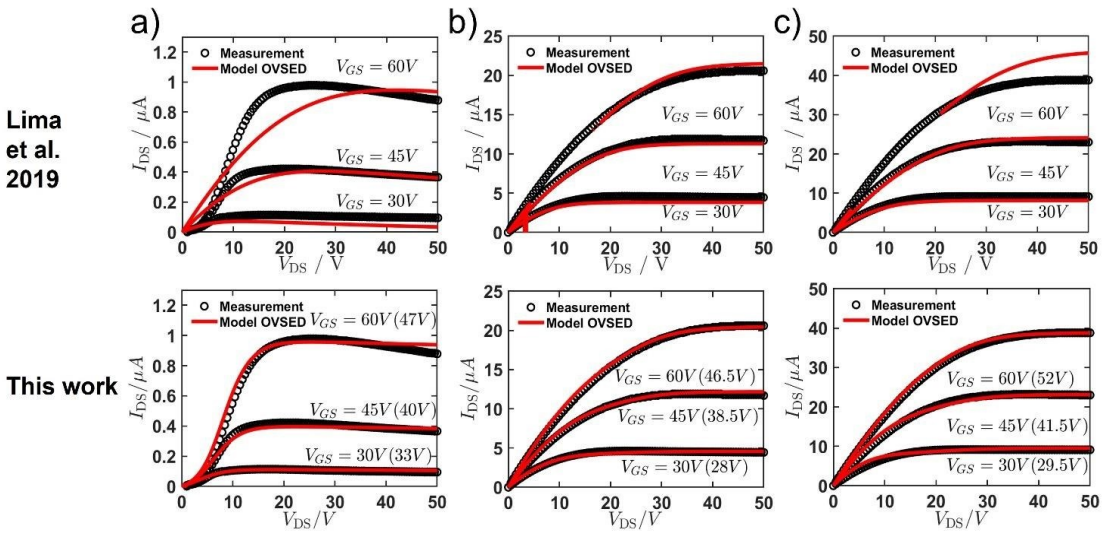

Figure 3.5) *Comparison between model fittings of Lima et al. 2019[34] (Top) to our current model (bottom) with the model output curves in red and the experimental measurements of P(NDI2OD-T2) bottom gate top contact OTFT devices in black for different interlayer types of a) Au (no interlayer), b) Au/Cr (10nm) and c) Au/Mn (10nm). The effective gate-source voltages used for the model are indicated in brackets.*

The values R_o and R_{max} describe the minimum and maximum resistance values, the hyperbolic tangent function facilitates the swift change from the maximum to the minimum. The parameter V_0 describes the source-drain voltage when the switch happens and V_{tun} describes the smoothing of the transition in volts, a greater V_{tun} describes a slow transition and a smaller V_{tun} describes a quick transition. The drain resistance (R_D) is set constant to the minimum. Since the model considers that the resistances are in series, the R_D and R_S can be interchanged. This modification of the OVSED model can now be described using 11 intrinsic parameters, while providing an improved characterization of experimental data with a clear s-curve (**Figure 3.5 and 3.6**).

Second, the experimental drain source current was different between output and transfer curves at the same V_{DS} and V_{GS}, which is problematic for modeling. The OVSED model creates a 3D surface (**Figure S3)** of the currents for all V_{DS} and V_{GS} then assumes that this current output is

independent whether V_{DS} or V_{GS} is constant or swept and independent on the sweeping speed. These assumptions do not always hold and a difference in current between the output and transfer curves could stem from the gate-source or gate-drain capacitance charging or discharging latency[39] or charge trapping. Multiple output curves were obtained at the same gate-source voltage in attempt to fill the charge traps but the discrepancy in experimental and effective voltage persisted. Therefore, we modified the OVSED model with the use of effective V_{GS}s in the output curves instead of the experimentally applied V_{GS}s. These modifications to the OVSED model led to improved fitting of the experimental values (**Figure 3.5 and 3.6**) with the extracted parameters reported on **Table 3.3**.

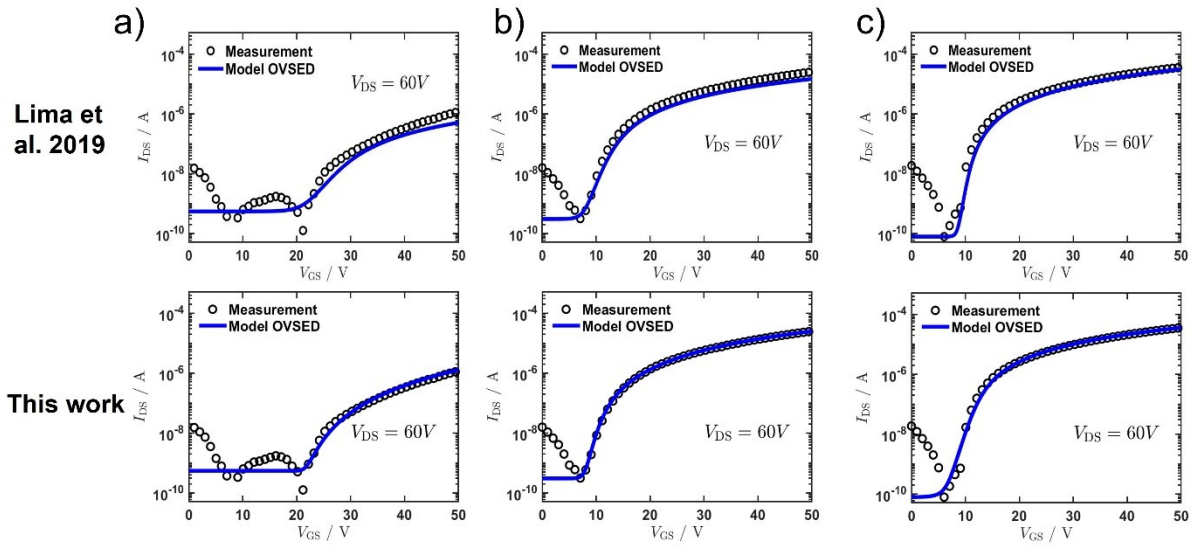

Figure 3.6) *Comparison between model fittings of Lima et al. 2019[34] (Top) to our current model (bottom) with the model transfer curves in blue and the experimental measurements of P(NDI2OD-T2) bottom gate top contact OTFT devices in black for different interlayer types of a) Au (no interlayer), b) Au/Cr (10nm) and c) Au/Mn (10nm).*

When applying the modified OVSED model to the experimental data we observe that the OTFTs with Au electrodes displayed a clear s-curve and lower current resulting in a very large R_{max} which differs significantly from R_o when compared to those with electrodes of Au/Cr(10 nm) and Au/Mn(10 nm) (**Figure 3.5)**. In addition, the V_0 values are greater for Au/Mn(10 nm) and even greater for Au/Cr(10 nm) electrodes when comparing to OTFTs with Au electrodes, this

indicates a slower transition from the R_{max} to R_o and for a very large V_0 we have $R_C \approx R_{max}$ (**Table 3.3**). Similarly, to what is observed with the SH model with R_C, R_{max} is larger for the device with Au electrodes and smaller for the device with Au/Mn(10 nm) contacts. As a result, R_{max} is a viable and more sensitive benchmark parameter for contact engineering. An estimated μ_e is given by $\mu_e = v_{sat}L/V_{temp}\lambda$ using the extracted value of λ, a reported carrier velocity of v_{sat}=1940 m/s[40], the channel length L = 30 μm and the thermal voltage V_{temp} = 25.7 mV; such that we obtain mobilities of 1.04 x10^{-1} cm^2/Vs, 7.47 x10^{-2} cm^2/Vs and 9.26 x10^{-2} cm^2/Vs for the devices with Au, Au/Cr(10 nm) and Au/Mn(10 nm) contacts respectively. The values demonstrate that the μ_e is largely independent of the contact details as expected.[31] We observe that the l parameter approaches 1 for close to ideal contact (**Table 3.3**). An exponent l = 1 indicates that the effective number of free charge carriers available for current flow increases proportional to the total charges accumulated in the semiconductor layer. Contact optimization should reduce the potential barrier for charge injection and thus eliminate charges trapped in the interface and channel access region. Thus, it is plausible that better contacts lead to lower values of l as observed. Overall, the s-curve was strictly observed in the OTFTs with Au contacts, which were also the ones that displayed the greatest resistance range. In addition, OTFTs with Au/Mn(10 nm) contacts have a smaller difference between experimental V_{GS} and their effective V_{GS} when compared devices with Au or Au/Cr electrodes. These results further demonstrate how Mn is a desirable interlayer for n-type OTFTs and that the OVSED model can help in predicting the resulting device behaviour.

Parameters [a]	Au [b]	Au/Cr(10nm) [b]	Au/Mn(10nm) [b]
V_T(V)	19.6	8.99	11.1
δ	8.04 x10^{-3}	1.00 x10^{-6}	5.07 x10^{-7}
n	26.3	40.8	52.5
l	2.25	1.47	1.00
λ	2.19 x10^5	3.04 x10^5	2.45 x10^5
V_{gcrit}(V)	39.0	421	77.7

J_T (mA/cm)	0.00203	0.709	7.83
V_{tun} (V)	5.48	7.69	9.93
V_0 (V)	0.158	24.6	20.3
R_0 (kΩ)	0.418	116	9.93
R_{max} (kΩ)	1.33 x10^5	216	20.9
I_{DSLeak} (nA)	0.540	0.300	0.774

Table 3.3) *Extracted improved OVSED model parameters for N2200 based OTFTs. V_T is the threshold voltage, δ is a unitless parameter that modifies the variable threshold, n is a unitless gate coupling factor, l is a unitless value describing the exponential tail of the density of trap states, λ is the ratio between the channel length and mean free path, V_{crit} is the critical voltage for carrier velocity saturation, J_T is the current density, V_0 is the turning point for the contact resistance, V_{tun} is the smoothing factor for the contact resistance, R_0 is the minimum contact resistance, R_{max} is the maximum contact resistance and I_{DSLeak} is the drain source current leakage. Fitted parameters of OVSED model for N2200 based bottom gate top contact OTFT with thermally evaporated electrodes with interlayers: where Au/X(Ynm), where Au = are the gold contacts, X is the interlayer and is either Mn as manganese or Cr as chromium; and Y is the thickness of that interlayer. Data extracted from* ***Figure 3.5 and 3.6****.*

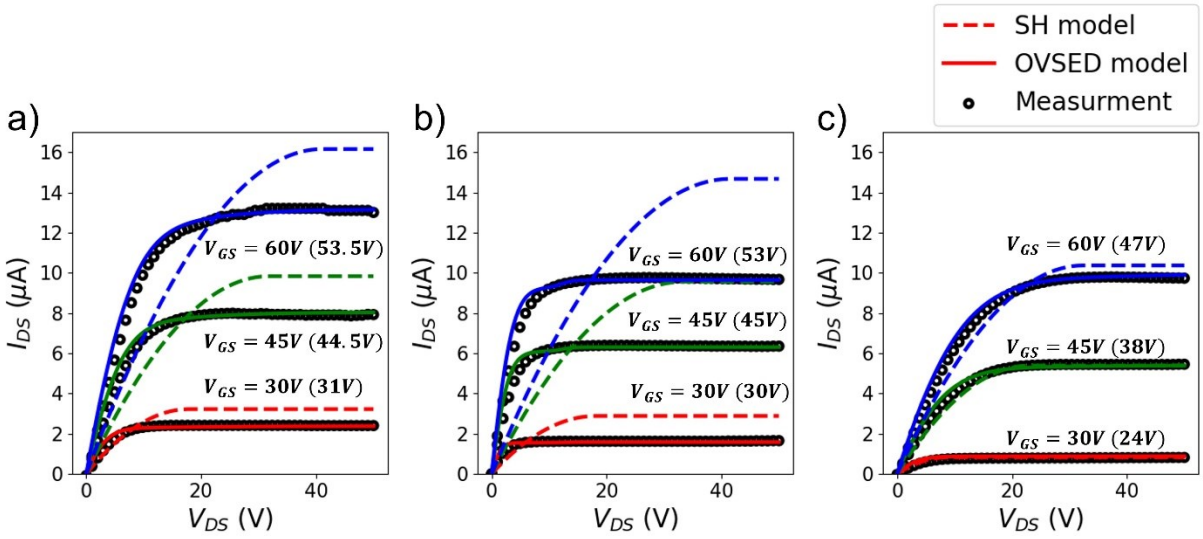

Figure 3.7) *Comparison between model fittings of Shichman-Hodges (SH) model11 (dashed line) to our current OVSED model (solid line) and the experimental measurements are black open circles for P(NDI2OD-T2) bottom gate top contact OTFT devices with 25 nm of Mn interlayer Au/Mn (25 nm). A), B) and C) represent 3 different devices with identical architecture. The fitting is tabulated in Table 3.4.*

	Device 1 (Figure 3.7a)		Device 2 (Figure 3.7b)		Device 3 (Figure 3.7c)	
Models	OVSED	SH	OVSED	SH	OVSED	SH
$V_{Tb)}$ (V)	17.9	13.2	19.0	12.0	15.6	15.1
R_C (kΩ)$^{c)}$	0.75 to 149.5	100.9	0.1 to 89.4	68.5	9.69 to 129	97.4
μ_e (cm_2/Vs)$_{d)}$	5.00 x10^{-2}	3.96 x10^{-2}	7.03 x10^{-2}	3.41 x10^{-2}	5.89 x10^{-2}	4.02 x10^{-2}

Table 3.4) *Electrical Characterization of three Au/Mn(25 nm) a) P(NDI2OD-T2) bottom gate top contact OTFT devices with 25 nm of Mn interlayer Au/Mn (25 nm)using 2 different models**.** a) N2200 based bottom gate top contact OTFT with thermally evaporated electrodes with interlayers: where Au/Mn(Ynm), where Au = are the gold contacts, Mn is manganese interlayer and Y is the thickness of that interlayer. b) Threshold voltage, V_T obtained from saturation region of the transfer curve (SH model) and the extracted values (OVSED model). c) Contact resistance extracted from the linear transfer curves using the Y-function method[4] (SH model) and extracted values (OVSED model). d) Electron mobility, μ_e extracted using the extracted value of λ (**Table 3.S1**) and the reported carrier velocity V_{sat}=1940 m/s[40] (OVSED model) and the saturation region of the transfer curve (SH model).*

The improved OVSED model was then applied to three different OTFTs fabricated with Au/Mn(25 nm) electrodes and plotted along side the SH model with R_C (**Equations 3.9 & 3.10**) and effective V_{GS}s (**Figure** 3.7). The full modeling parameters and the modeled transfer curves are displayed in **Figure 3.S4** and **Table 3.S2.** This direct comparison between the models demonstrates that the OVSED model better predicts the behavior of the OTFTs and thus provides a better extraction of the device parameters. When comparing the parameters (**Figure 3.7** and **Table 3.4**), the SH always evaluated the V_T smaller than what the OVSED model predicted. However, in all the devices, the SH's R_C fell within the bounds of the OVSED's R_C and the calculated μ_e values have the same magnitude as the ones calculated via the SH model. This demonstrates that the SH model can be accurate for ideal devices. Additionally, V_T and R_{max} are smaller for Au/Mn(10 nm) than for Au/Mn(25 nm) suggesting that, similarly to the conclusion from the SH model, the Au/Mn(10 nm) offers the best behavior. The OVSED model suggest that the variability of the Au/Mn(25 nm) devices stems from the V_{gcrit} parameter, specifically by the onset of velocity saturation. Overall, the improved OVSED model provides a better fit over the device's output and transfer curves compared to the classic SH model.

3.4. Conclusion

We demonstrated that the addition of a metal interlayer between the Au electrode and the semiconductor, with a work function closer to the LUMO levels of the P(NDI2OD-T2) semiconductor, provided smaller R_C by up to two order of magnitude and with improved V_T s. A

compromise between R_C and conductivity as the thickness of the Mn interlayer increases led to the optimal thickness of 10 nm of Mn which provided the lowest V_T with predictable μ_e. We improved the OVSED model[34] with the addition of a variable R_C to solve the drain-source-voltage dependent, non-ohmic contact resistance, and enabled the fitting of the s-curves found in devices with high R_C; and the use of effective voltages enable the experimental inconsistencies between output curves and transfer curves. The improved OVSED model was found to outperform the Shichman-Hodges model, commonly used for MOSFETs, by providing better fit to experimental data and thus extract more accurate parameters from the experimental OTFTs. Overall, the devices with Mn provided the most ideal behaviors and the best overall performance. Since n-type OTFTs are often plagued by high R_C, this study demonstrates and effective experimental route to improve device performance, with the use of Mn interlayers, while providing an accurate model for extraction of the contact resistance and the *l* parameter, both of which are viable benchmark quality parameters to test ideal device performance. Finally, models such as our improved OVSED model are critical for the proper characterization of OTFTs needed for their integration into complex circuitry and next generation flexible electronics.

3.5. Experimental

3.5.1. Device Fabrication

Diced Si/SiO_2 wafer chips with 220 nm oxide thickness were sonicated sequentially in water, acetone, and methanol for cleaning. These substrates were then plasma-treated for 15 minutes, rinsed with water and isopropanol, and dried. The treated substrates were then submerged in a solution of 1% (v/v) octyltrichlorosilane (OTS) in toluene for 1 hour at 70 °C. Following the OTS

treatment, the substrates were rinsed with toluene and isopropanol, then dried at 70 °C under vacuum for 1 hour.

A solution of 10 mg/mL P(NDI2OD-T2) (1-Materail Inc., Mw ≈ 160,000 g/mol and dispersity ≈ 3.0, determined using poly(styrene) standards, Lot #YY15042CH) in 1,2-dichlorobenzene was prepared, stirring at 500 rpm at 50 °C for 20 minutes. The solution was spin-cast onto the OTS-treated substrates at 4000 rpm for 90 seconds. The films were then dried under vacuum for 1 hour at 150 °C.

Finally, electrodes were deposited using shadow masks during physical vapour deposition of the required metals. The interlayer metal (Cr or Mn) was deposited first, at a rate of 0.5 Å/s until desired thickness. The Au electrodes were deposited immediately after deposition of the interlayer without moving the substrates or shadow masks, at a rate of 1 Å /s until reaching 50 nm. The shadow masks were designed to provide an OTFT channel length of 30 μm and a width of 1000 μm.

3.5.2. OTFT Characterization

The characterization of the OTFTs was done by analyzing the transistor's IV curves, more specifically the transfer and the output curves. The output curves were measured by sweeping the drain-source voltage (V_{DS}) at constant gate-source voltages (V_{GS}) and the transfer curves are measured by sweeping V_{GS} at constant V_{DS}. Each chip, containing 20 individual OTFT, were placed in a testing apparatus developed by Ossila. The devices were tested in an atmosphere of nitrogen gas (glovebox) at ambient temperature and measured using a LabVIEW program interfacing with voltage regulators (Keithley 2614B) used to measure output current and control voltage. The saturation and linear transfer curves were

obtained by setting the V_{DS} to 50V and 3V respectively while sweeping V_{GS} from 0-60V. Output curves were generated by varying the source-drain voltage (V_{DS}) from 0 to 50 V, while the gate-source voltage (V_{GS}) was varied from 0 to 60V in steps of 15V. The following equations from the Shichman-Hodges (SH) model[11] were used to calculate the mobility and threshold voltage from the transfer curves in the saturation region:

$$I_{DS_{sat}} = \frac{\mu W C_i}{2L}(V_{GS} - V_T)^2 \tag{3.2}$$

$$I_{DS_{lin}} = \frac{\mu V_{DS} W C_i}{L}\left(V_{GS} - V_T - \frac{V_{DS}}{2}\right)^2 \tag{3.3}$$

Where I_{SD} is the source-drain current, W is the channel width, L is the channel length, V_T is the threshold voltage, μ is the mobility, and C_i is the capacitance density of SiO_2 in F/m^2. Using $C_i = k_d \cdot E_o/t$, where k_d is dielectric constant, E_o is the permittivity in vacuum in F/m, and t_t is thickness in m we obtain C_i = 1.57 x 10^{-4} F/m^2. Equation (3.3) can be rearranged to the following form, where the mobility is linearly related to the slope of the $\sqrt{I_{SD}}$ vs. V_{GS} squared.

$$\mu = \frac{2L}{WC_i}\left(\frac{\partial\sqrt{I_{DS}}}{\partial V_{GS}}\right)^2 . \tag{3.4}$$

And V_T is the x-intercept of the linear fit used to calculate the mobility. Although there are other methods to calculate mobility[41], we opted to calculate the apparent saturation mobility. To allow stabilization of these parameters, multiple transfer curves were done and all, but the first curve were used. The contact resistance was obtained via the Y-function method[4] and the linear transfer curves:

$$R_C = \frac{\partial S}{\partial V_{GS}}\left(\frac{\partial Y}{\partial V_{GS}}\right)^{-1} V_{DS} \tag{3.5}$$

$$Y = I_{DS}S \tag{3.6}$$

$$S = \frac{1}{\sqrt{g_m}} \tag{3.7}$$

$$g_m = \frac{\partial I_{DS}}{\partial V_{GS}} \tag{3.8}$$

where g_m is the transconductance. Applying this to the SH model gives us the SH model with contact resistance which was used to compare with the OVESD model:

$$I_{DS_{Sat}} = \frac{-2R_C V_T + 4\chi^{-1} + 2V_{GS}R_C - 4\sqrt{\chi^{-1}(R_C V_{GS} + \chi^{-1} - V_T R_C)}}{R_C^2} \tag{3.9}$$

$$I_{DS_{Lin}} = \frac{V_{DS}\left(V_{GS} - V_T - \frac{V_{DS}}{2}\right)}{R_C\left(\frac{1}{R_C\chi} + V_{GS} - \frac{V_{DS}}{2} - V_T\right)} \tag{3.10}$$

with $\chi = (W\mu C_i)/L$.

3.5.3. OVSED model

The OVSED model was developed by Blawid and Lima[34] and can be summarized by the following equations where J_D, I_D, W, v_{sat}, Q_{free} and F_{sat} are the drain current density, the drain current, the channel width, the high-field bulk saturation velocity, the total charge of the free charges and a function.

$$J_D = I_D/W = v_{sat}Q_{free}F_{sat} \tag{3.11}$$

$$Q_{free} = q\sigma_v \cdot \left(\frac{Q_{tot}}{q\sigma_T}\right)^l \tag{3.12}$$

$$Q_{tot} = C_i V_{temp}\, ln\left[1 + exp\left(\frac{\Psi - V_{GS}}{nV_{temp}}\right)\right] \tag{3.13}$$

$$\Psi = V_T + |\delta|V_{DS} \tag{3.14}$$

The capacitance of the insulator, $C_i = k_d \cdot E_o/t$, where k_d is dielectric constant, E_o is the permittivity in vacuum, and t_t is thickness. The density of valence charge carriers and traps are denoted by σ_V

and σ_T . The thermal voltage V_{temp} can be expressed in terms of the temperature T, the Boltzmann constant k_B and the elementary charge q, $V_{temp} = k_BT/q$. Equation (3.14) is a variable threshold voltage dependent on the source drain voltage (V_{DS}) multiplied by a model parameter δ. Therefore, V_T is the threshold voltage when no voltage is applied across the source and drain. The l variable is a unitless value describing the exponential tail of the density of trap states in equation (3.12). The n is a gate coupling factor or non-ideality factor which determines the effectiveness of the gate bias to control the semiconductor charge. The high-field bulk saturation velocity $v_{sat} = \mu V_{temp}/\lambda_f$ is dependent on the drift mobility μ and the mean free path λ_f. This along with the density of valence charge carriers and traps is included in the current density $J_T = q\sigma_V(C_i n V_{temp}/q\sigma_T)^l$ to simplify the model. The last value in eq (11) is a function that describes the draining of accumulated charge carriers:

$$F_{sat} = \frac{1 - e^{-V_{DS}/V_{temp}}}{1 + 2t + e^{-V_{DS}/V_{temp}}} \tag{3.15}$$

$$t = \frac{2\lambda}{m^2(1-\eta^2)}\left[(1 - m\eta)e^{-m(1-\eta)} - 1 + m\right] \tag{3.16}$$

$$\eta = 1 - tanh\left(\frac{V_{DS}}{mV_{temp}}\right) \tag{3.17}$$

$$m = \frac{V_{GT}/V_{temp}}{1 + \sqrt{\frac{2V_{GT}}{V_{crit}}}} \tag{3.18}$$

$$V_{GT} = Q_{Tot}/C_i \tag{3.19}$$

where t is a unitless unit describing the critical length for diffusion, V_{gcrit} is the critical voltage for velocity saturation v_{sat} and $\lambda = L_G/\lambda_f$ with L_G being the gate length. With this the model can be described using only 7 intrinsic model parameters, J_T, δ, l, n, V_{gcrit}, V_T and λ since V_{DS}, V_{GS}, T and W were controlled. The parasitic values such as the leakage current I_{DLeak} was added to the final current value. And the source and drain electrode resistances (R_S and R_D) were accounted for by

subtracting $I_D(R_S + R_D)$ from V_{DS}. Additions and changes to the model were the following. To compensate for the s-shape originating from devices with a high contact resistance, a voltage dependence resistance replaced the contact resistances (**Equation 3.1**). The values R_O and R_{max} describe the minimum and maximum resistance values while the hyperbolic tangent function allows the swift change from the maximum to the minimum. The parameter V_0 is the source-drain voltage when the switch happens and V_{tun} describes the smoothing of the transition in volts, a bigger V_{tun} describes a slow transition and a smaller V_{tun} describes a quick transition. The drain resistance (R_D) is set constant to the minimum value since, even though the device is symmetric, the electric field's distribution is not. This adds an additional 4 parameters but replaces R_D and R_S. Now the model can be described using 11 model parameters, J_T, δ, l, n, V_{gcrit}, $V_{tun,}$ R_O, R_{max} V_T and λ. The final model modification is the use of effective gate source voltages. Since the current values of the output curves did not perfectly correspond to the current values of the transfer curves for the same V_{DS} and V_{GS} values, the V_{GS} values in the output curves were replaced by the V_{GS} at the same current level from the transfer curve of the same device.

3.6. Acknowledgement

The Natural Sciences and Engineering Research Council of Canada (NSERC RGPIN-2020-04079 to B.H.L) and NSERC CGS to S.B. Infrastructure used to complete this work was acquired using CFI-JELF and NSERC RTI (EQPEQ/ 472921-2015).

3.7. References

1. Minemawari, H. *et al.* Inkjet printing of single-crystal films. *Nature* **475**, 364–367 (2011).
2. Li, J. *et al.* A stable solution-processed polymer semiconductor with record high-mobility for printed transistors. *Sci. Rep.* **2**, 754 (2012).
3. Ong, B. S., Wu, Y., Li, Y., Liu, P. & Pan, H. Thiophene Polymer Semiconductors for Organic Thin-Film Transistors. *Chem. – A Eur. J.* **14**, 4766–4778 (2008).

4. Liu, C., Xu, Y. & Noh, Y.-Y. Contact engineering in organic field-effect transistors. *Mater. Today* **18**, 79–96 (2015).

5. Paterson, A. F. *et al.* Recent Progress in High-Mobility Organic Transistors: A Reality Check. *Adv. Mater.* e1801079 (2018) doi:10.1002/adma.201801079.

6. Reese, C. & Bao, Z. Overestimation of the field-effect mobility via transconductance measurements and the origin of the output/transfer characteristic discrepancy in organic field-effect transistors. *J. Appl. Phys.* **105**, 24506 (2009).

7. McCulloch, I., Salleo, A. & Chabinyc, M. Avoid the kinks when measuring mobility. *Science (80-.).* **352**, 1521–1522 (2016).

8. Bittle, E. G., Basham, J. I., Jackson, T. N., Jurchescu, O. D. & Gundlach, D. J. Mobility overestimation due to gated contacts in organic field-effect transistors. *Nat. Commun.* **7**, 10908 (2016).

9. Donnhäuser, S. *et al.* Impact of injection limitations on the contact resistance and the carrier mobility of organic field effect transistors. *Org. Electron.* **99**, 106343 (2021).

10. Shockley, W. A Unipolar 'Field-Effect' Transistor. *Proc. IRE* **40**, 1365–1376 (1952).

11. Shichman, H. & Hodges, D. A. Modeling and simulation of insulated-gate field-effect transistor switching circuits. *IEEE J. Solid-State Circuits* **3**, 285–289 (1968).

12. Li, H., Li, Y., Li, H. & Brédas, J.-L. Organic Field-Effect Transistors: A 3D Kinetic Monte Carlo Simulation of the Current Characteristics in Micrometer-Sized Devices. *Adv. Funct. Mater.* **27**, 1605715 (2017).

13. Yan, H. *et al.* A high-mobility electron-transporting polymer for printed transistors. *Nature* **457**, 679–686 (2009).

14. Waldrip, M., Jurchescu, O. D., Gundlach, D. J. & Bittle, E. G. Contact Resistance in Organic Field-Effect Transistors: Conquering the Barrier. *Adv. Funct. Mater.* **30**, 1904576 (2020).

15. Melville, O. A. *et al.* Contact Engineering Using Manganese, Chromium, and Bathocuproine in Group 14 Phthalocyanine Organic Thin-Film Transistors. *ACS Appl. Electron. Mater.* **2**, 1313–1322 (2020).

16. Serway, R. A. *Principles of Physics*. (Fort Worth, Texas: Saunders College Publisher, 1998).

17. Cook, J. G. & Meer, M. P. van der. The thermal conductivity and electrical resistivity of gold from 80 to 340 K. *Can. J. Phys.* **48**, 254–263 (1970).

18. Harper, A. F. A., Kemp, W. R. G., Klemens, P. G., Tainsh, R. J. & White, G. K. The thermal and electrical conductivity of chromium at low temperatures. *Philos. Mag. A J. Theor. Exp. Appl. Phys.* **2**, 577–583 (1957).

19. Whittaker, K. C. & Dziwornooh, P. A. The resistivity of α-manganese and some of its transition metal alloys. *J. Low Temp. Phys.* **5**, 447–460 (1971).

20. Bhosale, S. V *et al.* Naphthalene diimides: perspectives and promise. *Chem. Soc. Rev.* **50**, 9845–9998 (2021).

21. Al Kobaisi, M., Bhosale, S. V, Latham, K., Raynor, A. M. & Bhosale, S. V. Functional

Naphthalene Diimides: Synthesis, Properties, and Applications. *Chem. Rev.* **116**, 11685–11796 (2016).

22. Zhou, W., Yutronkie, N. J., Lessard, B. H. & Brusso, J. L. From chemical curiosity to versatile building blocks: unmasking the hidden potential of main-group phthalocyanines in organic field-effect transistors. *Mater. Adv.* **2**, 165–185 (2021).

23. Melville, O. A., Lessard, B. H. & Bender, T. P. Phthalocyanine-Based Organic Thin-Film Transistors: A Review of Recent Advances. *ACS Appl. Mater. Interfaces* **7**, 13105–13118 (2015).

24. Bedel Pereira, E. *et al.* Benzohexacene guide in accurate determination of field effect carrier mobilities in long acenes. *RSC Adv.* **12**, 671–680 (2022).

25. Xie, Z., Bâldea, I., Smith, C. E., Wu, Y. & Frisbie, C. D. Experimental and theoretical analysis of nanotransport in oligophenylene dithiol junctions as a function of molecular length and contact work function. *ACS Nano* **9**, 8022–8036 (2015).

26. Rice, N. A. *et al.* Polycarbazole-Sorted Semiconducting Single-Walled Carbon Nanotubes for Incorporation into Organic Thin Film Transistors. *Adv. Electron. Mater.* **5**, 1800539 (2019).

27. Zorn, N. F. & Zaumseil, J. Charge transport in semiconducting carbon nanotube networks. *Appl. Phys. Rev.* **8**, 41318 (2021).

28. Minagawa, M., Kim, Y., Claus, M. & Bao, Z. Reducing the contact resistance in bottom-contact-type organic field-effect transitors using an {AgO} x interface layer. **10**, 91601 (2017).

29. Brixi, S. *et al.* Air and temperature sensitivity of n-type polymer materials to meet and exceed the standard of N2200. *Sci. Rep.* **10**, 1–10 (2020).

30. Chen, Z., Zheng, Y., Yan, H. & Facchetti, A. Naphthalenedicarboximide- vs Perylenedicarboximide-Based Copolymers. Synthesis and Semiconducting Properties in Bottom-Gate N-Channel Organic Transistors. *J. Am. Chem. Soc.* **131**, 8–9 (2009).

31. Shukla, D. *et al.* Thin-film morphology control in naphthalene-diimide-based semiconductors: high mobility n-type semiconductor for organic thin-film transistors. *Chem. Mater.* **20**, 7486–7491 (2008).

32. Klauk, H. Will We See Gigahertz Organic Transistors? *Adv. Electron. Mater.* **4**, 1700474 (2018).

33. Liu, C. *et al.* Universal diffusion-limited injection and the hook effect in organic thin-film transistors. *Sci. Rep.* **6**, 29811 (2016).

34. Lima, A. A. & Blawid, S. Modeling organic thin-film transistors based on the virtual source concept: A case study. *Solid. State. Electron.* **161**, 107639 (2019).

35. Khakifirooz, A., Nayfeh, O. M. & Antoniadis, D. A Simple Semiempirical Short-Channel MOSFET Current–Voltage Model Continuous Across All Regions of Operation and Employing Only Physical Parameters. *IEEE Trans. Electron Devices* **56**, 1674–1680 (2009).

36. Rakheja, S., Lundstrom, M. & Antoniadis, D. A physics-based compact model for FETs from diffusive to ballistic carrier transport regimes. in *2014 IEEE International Electron*

Devices Meeting 35.1.1-35.1.4 (2014). doi:10.1109/IEDM.2014.7047172.

37. Lundstrom, M., Datta, S. & Sun, X. Emission–Diffusion Theory of the MOSFET. *IEEE Trans. Electron Devices* **62**, 4174–4178 (2015).

38. Chianese, F. *et al.* Linear conduction in N-type organic field effect transistors with nanometric channel lengths and graphene as electrodes. *Appl. Phys. Lett.* **112**, 213301 (2018).

39. Lin, Y.-J., Tsai, C.-L. & Huang, B.-C. Discrepancy in mobility extracted from transfer and output characteristics of organic thin film transistors. *Appl. Phys. Lett.* **97**, 203509 (2010).

40. Perinot, A. *et al.* Direct-written polymer field-effect transistors operating at 20 MHz. *Sci. Rep.* **6**, 38941 (2016).

41. Choi, H. H., Cho, K., Frisbie, C. D., Sirringhaus, H. & Podzorov, V. Critical assessment of charge mobility extraction in FETs. *Nat. Mater.* **17**, 2–7 (2018).

3.8. Supplementary Information

Note that we used in the SH model the apparent values of the mobility obtained from Eq. (4) and did not try to de-embed the contact resistance. However, the SH model only depends weakly on Rc for the technology considered here as shown in **Figure 3.S1**. Thus, the use of the apparent instead of the de-embedded values will not change the conclusion that the SH model only poorly describes the measured.

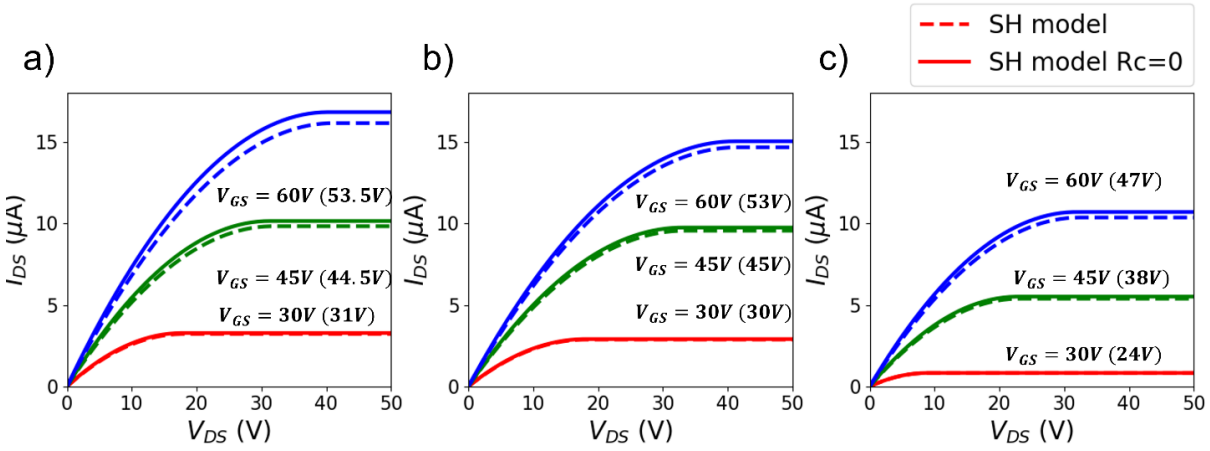

Figure 3.S1) *A graphical representation of the difference between the SH model with contact resistance (straight line) and without contact resistance (dotted lines), using the parameters of the Au/Mn(25nm) devices from* ***Figure 3.S4.***

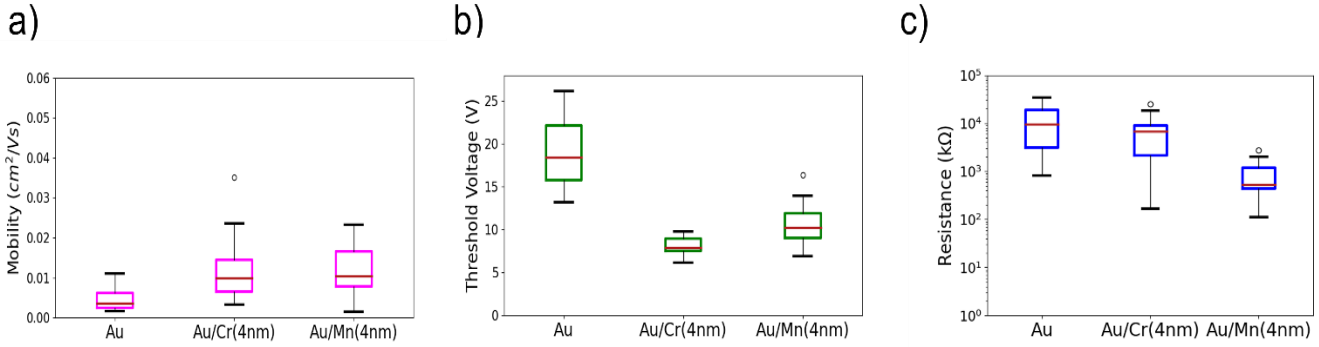

Figure 3.S2) *Properties for the saturation region of the devices with no interlayers, 4 nm of chromium and 4 nm of manganese. The graphs display a) the mobility, b) the threshold voltages, c) the contact resistance in a box plot with the red line indicating the median and empty circles indicating outliers.*

Contact[a)]	μ_e [b)] (cm^2/Vs)	V_T[b)] (V)	R_C[c)] (kΩ)
Au	$(4.6\pm0.8)\times 10^{-3}$	19 ± 1	$(1.3\pm0.3)\times 10^{4}$
Au/Cr(4nm)	$(1.2\pm0.2)\times 10^{-2}$	8.1 ± 0.2	$(7\pm1)\times 10^{3}$
Au/Mn(4nm)	$(1.2\pm0.1)\times 10^{-2}$	10.7 ± 0.6	$(9\pm2)\times 10^{2}$

Table 3.S1) Electrical Characterization of N2200 based OTFTs with varying interlayer composition. a) N2200 based bottom gate top contact OTFT with thermally evaporated electrodes with interlayers: where Au/X(Ynm), where Au = are the gold contacts, X is the type of interlayer and Y is the thickness of that interlayer. b) Electron mobility, µe and threshold voltage, VT obtained from saturation region of the transfer curve. c) Contact resistance extracted from the Y-function method[55] and the linear transfer curves.

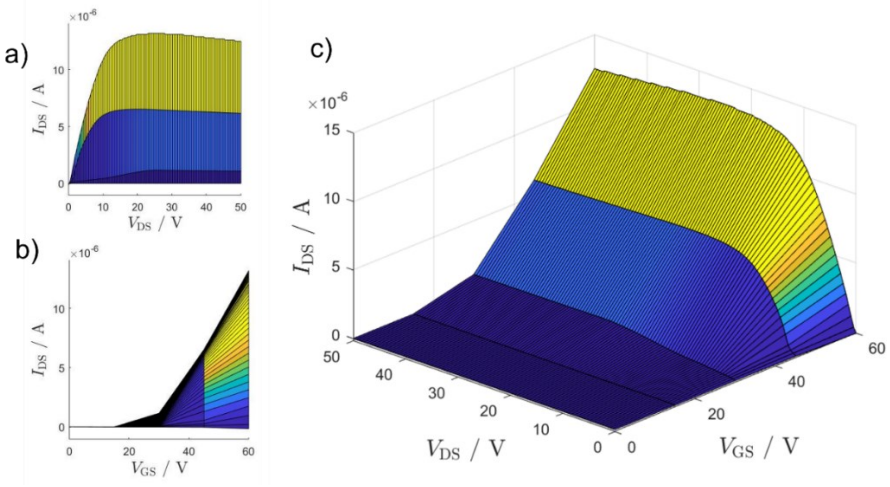

Figure 3.S3*) A 3D characteristic plot of the drain source current at different drain source voltages and different gate source voltages for a bottom gate top contact device with a P(NDI2OD-T2) semiconductor and Au electrodes and 25nm of Mn as an interlayer between the Au and the P(NDI2OD-T2). The output curve a) and transfer curve b) view which form the 3D plot c).*

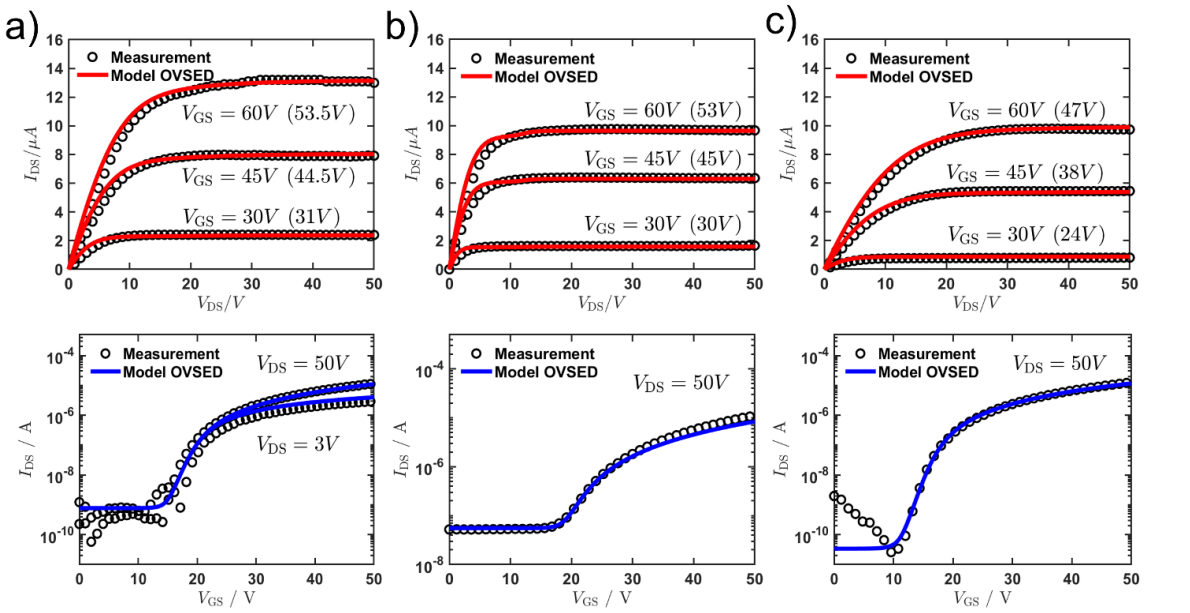

Figure 3.S4*) The improved OVSED model fittings after the modification with the modeled output curves in red, modeled forward transfer curves in blue, the measurements in black and the effective gate-source voltage indicated in brackets for three different N2200-based OTFT devices with Au/Mn(25nm) electrodes. Fitting is tabulated in* ***Table 3.S2.***

	Device 1 (Figure 3.8a)	Device 2 (Figure 3.8b)	Device 3 (Figure 3.8c)
V_T (V)	17.9	19.0	15.6
δ	1.02 x10^{-8}	1.30 x10^{-8}	1.00 x10^{-8}
n	55.5	56.1	53.3
l	1.00	1.01	1.00
λ	4.54 x10^{5}	3.23 x10^{5}	3.87 x10^{5}
V_{gcrit}(V)	23.4	2.23	204
J_T (mA/cm)	9.15	12.2	4.31
V_{tun} (V)	16.7	1.97	60
V_0 (V)	15.3	12.2	59.9
R_0 (kΩ)	0.750	0.1	9.69
R_{max} (kΩ)	149.5	89.4	129
I_{DSLeak} (nA)	0.774	55.7	0.0339

Table 3.S2) *Extracted improved OVSED model parameters for three characteristic N2200 based OTFTs with Au/Mn(25nm) electrodes. a) V_T is the threshold voltage, δ is a unitless parameter that modifies the variable threshold, n is a unitless gate coupling factor, l is a unitless value describing the exponential tail of the density of trap states, λ is the ratio between the channel length and mean free path, $V_{g\,crit}$ is the critical voltage, J_T is the current density, V_0 is the turning point for the contact resistance, V_{tun} is the smoothing factor for the contact resistance, R_0 is the minimum contact resistance, R_{max} is the maximum contact resistance and I_{DSLeak} is the drain source current leakage. b) Fitted parameters of OVSED model for N2200 based bottom gate top contact OTFT with thermally evaporated electrodes with interlayers: where Au/Mn(25nm), where Au = are the gold contacts, the interlayer is Mn; and 25nm is the thickness of that interlayer. Data extracted from* ***Figure 3.S4****.*

The OVSED model was also applied to three different OTFTs fabricated with Au/Mn(25nm) electrodes (**Figure 3.S4**) to characterize the consistency of the parameters and to further apply the model against top performing devices. Unlike the earlier devices, the bipolarity was less common in these devices and only appeared in sample **Figure 3.S4c**). The l parameter is very close to 1 with a maximum at 1.01 and a minimum at 1 (**Table 3.S4**), indicating that these devices expressed a linear increase in free charge carrier density (**Equation 3.12**). According to the modified OVSED model, the drain current density of all the devices were very similar, with the last device (c) experiencing a slightly lower value. This can be clearly observed in **Figure 3.S4**. All the devices experienced similar resistance minimums from 7.5 kΩ to 10 kΩ. and maximums from 68 kΩ to 100 kΩ. The V_{gcrit} parameter contains a large variability for the Au/Mn(25nm), this may indicate a device dependent internal electric field which hinders performance reproducibility. As previously stated λ is the ratio between the channel length and the mean free path, thus a large λ, as reported in **Table 3.3** and **Table 3.S2**, indicates that devices operate in the diffusive and not the ballistic limit. It is important to note that the devices with Au/Cr and Au/Mn contacts can also be modeled with good accuracy by the OVSED model with a bias independent series resistance when using effective voltages.

3.9. Continued Work and Additional Literature Contributions

After the publication of the paper in Applied Physics Reviews, our collaborator in Brazil, Stefan Blawid, who derived the first implementation of the OVSED model in his paper "Modeling organic thin-film transistors based on the virtual source concept: A case study" by Lima A. and Blawid S. in 2019, thought that the work on the model deserved to be in its own paper. Therefore, instead of putting an additional chapter in the paper submitted in Applied Physics, a new manuscript was written by Stefan which illuminated the progress made on the model. The

manuscript discussed a roadmap for device characterization, leading from the OVSED model to the SH model. The manuscript's OVSED model did not include the bias dependent contact resistance, but instead incorporated the Y-function method to extract the contact resistance. The paper included my N2200 device fittings and discussed our conclusions about the model. It was published in March of 2022 in IEEE Journal on Flexible Electronics under the title "Self-Consistent Extraction of Mobility and Series Resistance: A Hierarchy of Models for Benchmarking Organic Thin-Film Transistors".

Chapter 4: Conjugated Wrapping Polymer Influences Photoexcitation of Single-Walled Carbon Nanotube-based Thin Film Transistors

Context

The previous work showed promising results with the improved OVSED model. The model fitted the data quite well, and therefore I felt it would be well suited to help solve a different issue with single walled carbon nanotube (SWNT) based TFTs. In our group, the separation of semiconducting and metallic carbon nanotubes for our TFTs is done using selective polymer dispersion. I found that very little work has been done on the effect of the dispersion polymer when using the SWNT for photodetection in TFTs. I decided to isolate the SWNT and polymer effects by illuminating them at their individual absorption peaks. Our collaborators (Dr. Fong and Prof. Adronov) synthesized novel copolymers, which have previously been reported as viable dispersion polymers for SWNT in TFT. Using two of these polymers along with PFO-BPy, I could investigate if the effects I observed were polymer dependent. I could subsequently use the OVSED model to pin-point which parameter is affected by the exposure. This manuscript was published in Materials Chemistry C in 2023. The following chapter contains minor changes compared to the published version.

Contributions

For this work, I prepared the semiconducting SWNT dispersions using the three different polymers. I performed UV-Vis-NIR spectroscopy of the dispersions. I fabricated all of the devices and carried out all of the device characterization and analysis. I assembled the optical setup and wrote the manuscript with input from the co-authors.

4.1. Abstract

The fabrication of high-purity semiconducting single-walled carbon nanotubes (sc-SWNTs) often utilizes conjugated polymers to isolate the semiconducting from the metallic species. These polymers preferentially sort and disperse certain sc-SWNT chiralities and often remain wrapped around sc-SWNTs during device integration. In this study, we expose three different SWNT based thin film transistors (TFT), each with a different dispersion polymer Poly(carbazole-co-fluorene) (PCF), poly(fluorene-co-dimethoxybenzene) (PFMB), or poly(fluorene-co-bipyridine) (PFO-BPy), to three different laser wavelengths. The wavelengths were selected to overlap both the optical transitions of the polymer-wrapped sc-SWNTs and the polymer absorption maxima. We report fundamental TFT metrics to monitor changes after light exposure, such as the current profile, the threshold voltage, and the mobility. We show that two phases emerge. An initial soak, where the devices change after an initial exposure which permanently increases the mobility. The second phase, the photo cycling, produces repeatable device performance between exposures “On Cycling” and post exposures “Off Cycling”, such as consistent threshold voltage shifts with an overall average shift of 3.6±0.6 V, highly dependant on the wavelength and polymer, thus providing greater motivation for tunable SWNT-based TFT photodetectors. Although the general behavior is shared among most TFT types and wavelengths, discrepancies in intensity emerge, especially when exciting the polymer. Hence, we show the importance of polymer choice when considering desirable parameters, in addition to their selected SWNT chirality.

Keywords

High-purity semiconducting single-walled carbon nanotubes (sc-SWNTs); Thin film transistors (TFT); Photodetector; Conjugated polymer wrapping; Photoexcitation.

4.2. Introduction

High-performing flexible semiconductors are essential for developing wearable sensors. Single-walled carbon nanotubes (SWNTs) combine desirable optical and electronic properties with outstanding mechanical strength,[1] making them uniquely suited for flexible photosensors integrated with textiles.[2] Recent photonic applications of SWNTs include single-photon emitters,[3,4] SWNT electroluminescence,[5] room temperature lasing[6], infrared detectors[7], and even diodes[8]. Many SWNT photonic applications require semiconductor purity. SWNT synthesis produces a mixture of chiralities and diameters; this results in a mixture of metallic and semiconducting SWNTs, with about one-third being metallic.[9] For semiconducting applications, it is essential that semiconducting SWNTs (sc-SWNTs) are extracted from the mixture and separated from metallic SWNTs (m-SWNTs). Selective dispersion using conjugated polymers is fast, inexpensive, scalable, and facilitates reliable isolation of sc-SWNTs.[10–14] Several conjugated homo- and co-polymers with different functional groups have been reported to sort and disperse sc-SWNTs with purities over 99 %,[14–17] and even purities as high as 99.99 %.[14] To date, SWNTs have been incorporated into electronic and sensing applications including thin-film transistors (TFT),[15,18–23] pressure detectors,[24,25] pH sensors,[26] chemical sensors,[27,28] and other applications.[29] SWNT-based TFTs with photosensitive semiconductor materials can be used as phototransistors, key components of optoelectronic circuits,[30] enabling the detection of light, and bolometric effect based photodetectors.[2,31]

Reported examples of SWNT TFT-based photodetectors include light polarity detectors,[32] near-infra-red detectors,[33] and flexible photodetectors.[2] However, the photogating effect of the conjugated polymer conjugated wrapping polymer on transistor properties have yet to be investigated and are sometimes assumed to have negligible impact on device performance due to the non-covalent interaction between the polymer and sc-SWNTs. Although, SWNTs have been

shown to work in conjunction with wrapping and non wrapping polymers such as poly(3-hexylthiophene) (P3HT) to improve photocurrent through exciton splitting[34–37]. In addition, the electronic nature of the polymer backbone can affect the efficacy of sc-SWNT extraction. Adronov and coworkers showed that tuning the conjugated polymer backbone to be more electron-rich biased selectivity towards electron-poor sc-SWNTs, and inversely for m-SWNTs.[38,39] The wrapping polymer can also affect polymer-SWNT film morphology,[40] which can make it difficult to determine whether the polymer effect is due to differences in film morphology (e.g., SWNT bundling) or to an electronic interaction between the polymer and SWNT. Ferguson and co-workers studied the effect of wrapping polymer on exciton transport in monochiral (6,5) and (7,5) sc-SWNT networks.[41] The authors demonstrated that removal of the wrapping polymer resulted in increased SWNT bundling which had two effects: excitons could move between SWNTs in neighbouring bundles, and the downhill energy transfer of excitons resulted in increased exciton trapping within bundles. Zaumseil and co-workers showed direct evidence of photoinduced charge transfer from (6,5) SWNTs to the wrapping polymer, PFO-BPy, *via* the S_{33} and S_{22} energetic transitions.[37] Additionally, Xiaohui and co-authors have investigated photoconductivity in semiconducting carbon nanotubes and have concluded that their devices experienced an increased photocurrent when illuminating at the second van Hove transition with most of the generated current consisting of split excitons.[42]

In this study, we provide insight into the development and engineering of high-performing SWNT TFT-based photodetectors. We used three different conjugated co-polymers with different chromophores to prepare sc-SWNT dispersions for incorporation into TFTs. Fluorene and carbazole moieties have been shown to have applications in light emission,[43] organic photovoltaics,[44] and electrochromic devices.[45] Poly(carbazole-*co*-fluorene) (PCF), poly(fluorene-

co-dimethoxybenzene) (PFMB), and poly(fluorene-*co*-bipyridine) (PFO-BPy) (**Figure 4.1**) have been reported to produce ultra-pure sc-SWNTs and corresponding high-performing TFTs.[16,40,46] However, the unique structures of the conjugated polymers caused different optical absorption which could affect device performance under irradiation. We evaluated essential transistor metrics to investigate the effect of polymer structure on device performance, including charge carrier mobility, threshold voltage, and current characteristics as a function of light exposure (intensity and wavelength). To comprehensively assess the effect of each polymer and generate more excitons we utilized laser sources with wavelengths matching the absorption transition of each copolymer and the SWNTs (**Figure 4.1 and 4.E1**).

4.3. Results and Discussion

Given the quasi-one-dimensionality of the nanotubes, the optical absorption peaks of SWNTs can be described using the Van Hove singularities. This gives rise to energy optical transition peaks S_{11}, S_{22} and S_{33} for semiconducting tubes and M_{11} for metallic tubes. The transition energies for the optical peaks are dependent on the chirality of the nanotubes, thus the polymer used during extraction will affect the positions of these peaks based on the polymer's selected chiralities.[11] For our nanotube dispersions, the selected chiralities are of similar diameters since the positions of the optical transition peaks are in proximity of each other. The dispersions show multiple peaks for each unique chirality's optical transition peak, indicating the range in the polymer's selected chiralities. Three excitation wavelengths were chosen near the absorption peaks of all three dispersions, each with their own polymer **(Figure 4.1 and 4.E1)**. The first wavelength, 405 nm, corresponds to the absorption peak of the polymers, while the other two, 532 nm and 980 nm, correspond to the S_{33} and S_{22} SWNT energetic transitions, respectively. The S_{11} transition is also visible on the absorption plot, around 1600 nm, but was not chosen as an absorption

wavelength. This is because the position and intensity of the S_{11} peaks are unstable due to its small bandgap and closeness to the Fermi level which increases its susceptibility to doping effects. It is important to note that the absorption profile was taken before the removal of excess polymers *via* rinsing, although our lab has shown, using Raman spectroscopy, that rinsing the polymer-SWNT film removes most of the unbound polymer, leaving only the polymer-wrapped SWNTs.[40] After excess polymer removal *via* solvent rinsing, we expect lower, but still present, polymer absorption. Thus the 405 nm laser would mainly excite the polymer on the nanotube, rather than excess unbounded polymer remnants. This would allow us to better examine charge interactions and transistor properties during polymer excitation.

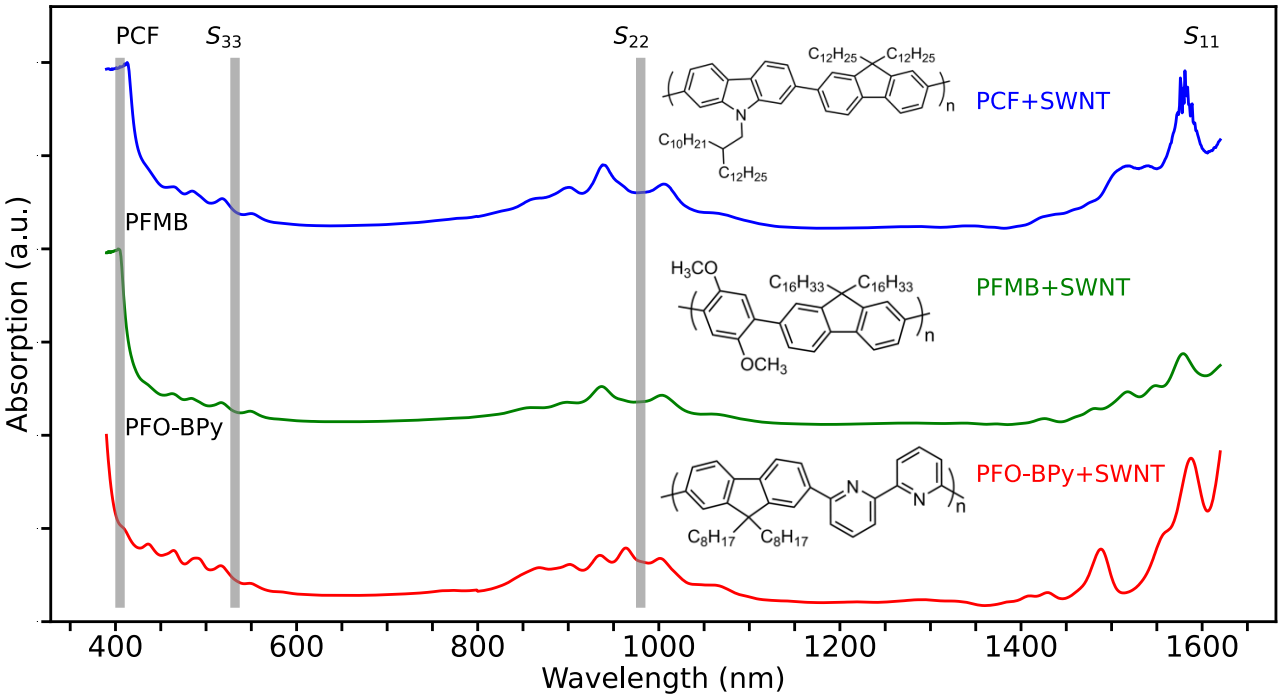

Figure 4.1)*: Absorption profiles of the sc-SWNTs for all three dispersions, each using a different polymer whose structure is displayed over each corresponding absorption spectrum.*

The SWNT TFT-based devices were fabricated using a bottom gate top contact morphology. The base consists of a dielectric SiO_2 layer followed by a Si gating layer. Atop the base, a single layered, randomly aligned sc-SWNT film lay within a 20 µm channel, deposited via machine drop casting, provides the semiconductor function of the TFT. Au electrodes with a Mn interlayer were used, with the Mn providing better adhesion to the wafer. Contact to the electrodes was facilitated via probe pins.

Two main phases were evaluated from the measurements. The first compares the device performance before exposure to that after its first exposure: this section is referred to as the Soaking phase and marks an irreversible change. The second phase, after the Soak, compares the performance of repeated exposures with performance after all exposures. This is called the Photo Cycling phase and marks reversible and reproducible behavior **(Figure 4.2)**.

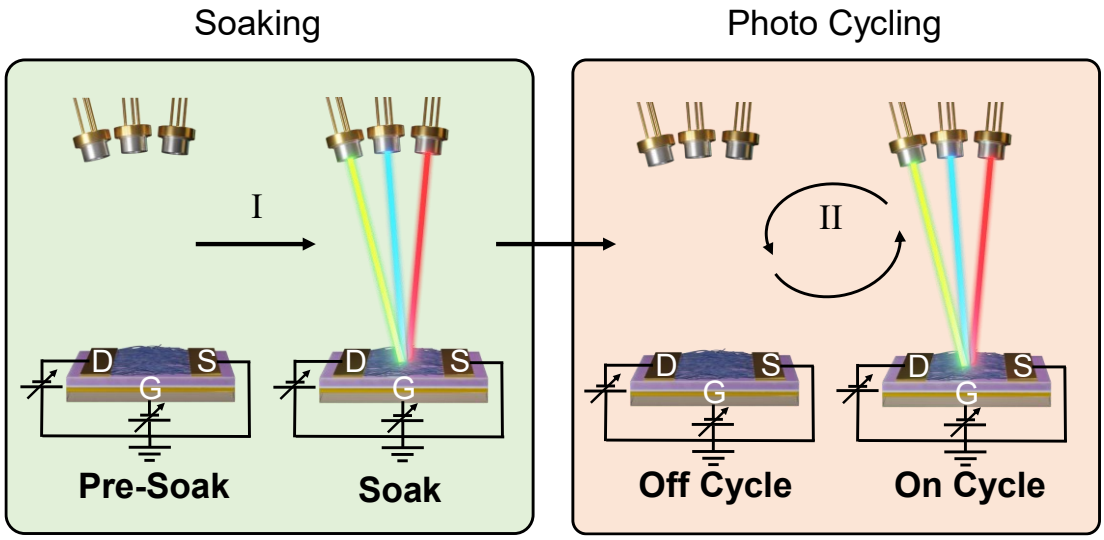

Figure 4.2)*: A procedural schematic of the Soaking and Photo Cycling processes along with a circuit diagram containing the device gate (G), drain (D), source (S), and power connections to measure I-V curve characteristics.*

During both processes the off current (I_{OFF}), threshold voltage (V_T) and charge carrier mobility (μ) were analysed. To elucidate the impact of the different states, such as "Pre-Soak" and "Soak", the difference between both were taken for each device, and then normalized using the pre-exposure value for the current and the mobility. The V_T was not normalized to illustrate the absolute shift rather than a percentage change, this was calculated as follows:

$$\Delta V_T = V_{T_{illuminated}} - V_{T_{Non-illuminated}} \quad (4.1)$$

For both phases "illuminated" represents the Soak or On Cycling and "Non-illuminated" represents the Pre-Soak or the Off Cycling, depending on the phase being evaluated. For each condition, nine to eighteen devices were tested, each in air as *p*-type transistors.

4.3.1. Soaking

The Soaking is the first phase, where we compare the pre-exposure devices to their performance after the first exposure. During this phase we observe a large change in performance, especially in the current profile and V_T. The wrapping polymer not only influences the dispersed semiconducting chiralities, but also the performance of the SWNT TFTs after light exposure. In all cases the V_T shifts to more positive voltages during the soak (**Figure 4.3c**). This represents a decrease in threshold voltage once the device is illuminated. This could be because the presence of additional charge carriers, due to addition of photocurrent charges generated from split excitons, requires a weaker field effect to surpass the activation energy. The photoexcitation is displacing charge carriers from the valence bands to the conduction bands; thus, a weaker gate voltage is required to activate the TFT and the mobility saturates at a lower gate voltage. This photogating effect is well known and has previously been studied.[34]

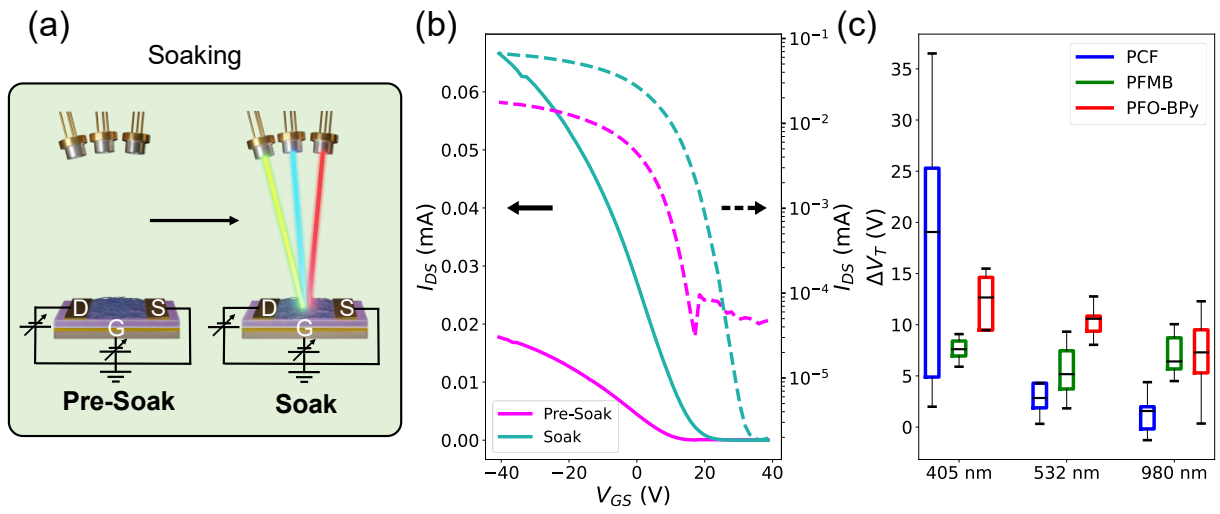

Figure 4.3)*: The difference in performance between Pre-Soak and Soak at 4 W/cm². (a) A procedural schematic of the Soaking process. (b) Characteristic transfer curves of a PFMB-SWNT device illuminated at 405 nm, linear curve (solid line) and the logarithmic (dashed line) with V_{DS} = -3 V. (c) Box plot of the average ΔV_T.*

When the exposure excites the polymer at 405 nm, the ΔV_T varies depending on the dispersion polymer. For PCF, the shift was highly variable compared to the other two polymers. For PCF and PFO-BPy, a decrease in V_T shift is observed when the wavelength is increased; this could be a result of lowering the photon energy. However, for the PFMB the shift is comparatively stable for each wavelength. The mobility tends to increase after exposure, with PFO-BPy at 532 nm nearly reaching an increase of 100 %. This is shown as an increase in the linear transfer curve's slope going from positive to negative. Once again, the PCF-SWNT devices had a highly variable shift when illuminating the polymer's absorption compared to illuminating at the nanotube's absorption (**Figure 4.E2**). The I_{OFF} decreases slightly after exposure for each condition and the I_{ON} increases, which results in a higher On/Off current ratio during illumination. Overall, once a device is exposed, the V_T decreases, the μ increases and the I_{OFF} decreases for most devices and wavelengths. The magnitude of each shift varies depending on the wavelength and polymer used. It is worth noting that SWNTs participate in an electrochemical redox reaction involving adsorbed oxygen and moisture which is likely occurring alongside this process. At low and neutral pH levels,

the O_2/H_2O redox reaction extracts electrons from the SWNT valence band causing hole doping. Although unintentional, this may explain the change in mobility, as p-doping has been found to slightly change the *I-V* curve.[47,48] Another possible explanation for the soaking effect could be a laser annealing process discussed by Mucklich and co-workers.[49] While these authors used a significantly stronger laser, they report a decrease in channel resistance through removal of defects; such changes would permanently increase mobility such as in our case. Thus a possible semi-permanent annealing process maybe occurring.

4.3.2. Photo Cycling

In the second (Photo Cycling) phase, the devices have already been exposed and have passed through the Soaking phase. We compare the performance during re-exposures and after those exposures. After the Soaking phase, the devices behaved differently but consistently during and after subsequent exposures.

The mobility scarcely changes when comparing re-exposures during the cycling phase. The normalized differences in μ remain near zero, although at the polymer's absorption, 405 nm, μ seems to decrease slightly, hinting at differences between polymer absorption and nanotube absorption. Since the μ of sc-SWNTs depend on the density, number of junctions or contacts, and channel resistance, the addition of photo-induced excitons should not change μ.[50] The V_T continues to decrease when illuminated with an overall ΔV_T average of 3.4±0.5 V, but does not return to its pre-exposed level. The shift is larger when exposing the devices to 405 nm, the polymer's peak, compared to exposure at the nanotube's absorption peaks. In all cases except for the PFO-BPy devices at 980 nm, the I_{OFF} decreased during exposure. The I_{OFF} can also be defined as dark current as it is the current that passes while reverse biased, thus it can be said that the light seems to suppress the dark current in the TFTs. The dark current is large when there is a large trap density

which allows charge carriers to pass even in reverse bias.[51] This could indicate that there is a creation of unbound excitons *via* wavelength-dependent light exposure, which fills the charge traps through charge separation, which in turn suppress the dark current[52–54]. It is important to mention the repeatability between multiple re-illuminations with the laser ON and after illuminations with the laser OFF. This reproducibility can be observed in **Figure 4.4b** where the inset shows the eight lines present that almost completely superimpose each other.

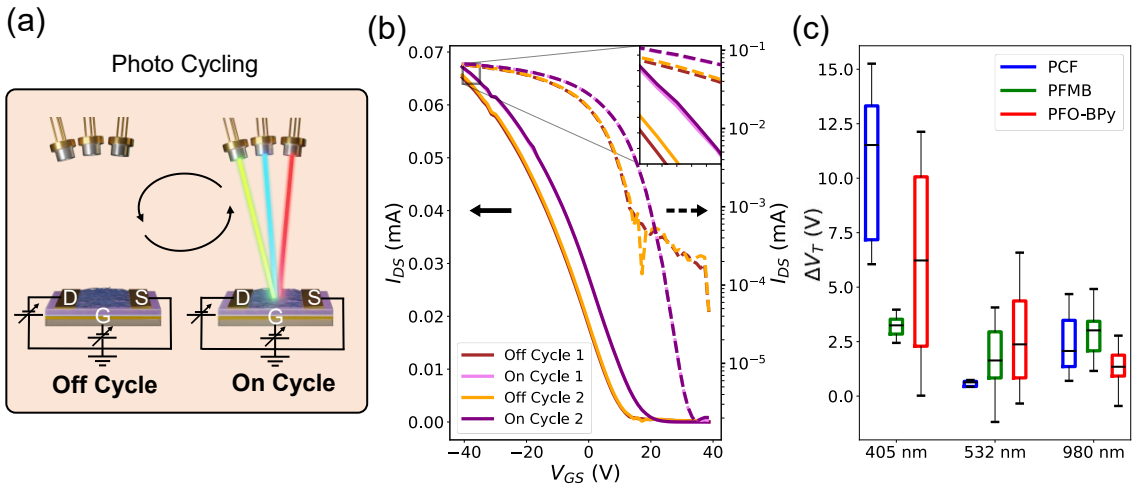

Figure 4.4)*: Difference in performance between Off Cycle and On Cycle at 4 W/cm². (a) A procedural schematic of the Photo Cycling process. (b) Characteristic transfer curves of a PFMB-SWNT device illuminated at 405 nm, linear curve (solid line) and logarithmic (dashed line) with V_{DS} = -3 V. (c) Box plot of the average ΔV_T.*

Atomic force microscopy (AFM) of the devices was performed, and although each polymer dispersion seems to extract similar nanotube diameters and was prepared identically, there are differences in the AFM images (**Figure 4.E5**). The nanotube density was highest for PCF and lowest for PFMB. Additionally, the AFM images give an insight into the leftover polymer or unbounded polymer that was not fully washed away. These are the white dots among the nanotubes. From this, we can tell that the PFO-BPy had the most leftover polymer, and the PCF had the least. These differences between samples may help explain certain changes between devices. For instance, the dark current is not only dependent on charge traps, but also on carbon

nanotube densities, with higher densities having higher dark currents.[51] Thus, this may explain why the off current in PCF is higher than in other devices.

Because of their higher nanotube density and decreased unbounded polymer, measurements of varying intensity and wavelengths were conducted on new PCF devices (**Figure 4.E4**). From these, regardless of the laser intensity, similar trends were extracted. Light exposure decreases V_T semi-permanently, increases mobility, and reduces the dark current. In addition, most of the device variability arose from the polymer's absorption, 405 nm, further displaying that the polymer interacts differently than the rest of the nanotube.

The overall effect of illumination is a rise in mobility, without significant change after the Soaking, a decrease in the threshold voltage and a lowered off current. The intensity of each greatly depends on the wavelength and the type of polymer. The changes in the ON current and the ON/OFF current ratio were recorded, but these were not significant as the results often remained near zero. These results show a potential for semiconducting SWNTs to be used as photodetectors, and the use of conjugated polymer dispersions and their chiral selection as a way to tune the desired response intensity. For instance, if the threshold voltage is the detection mechanism around 405 nm, then PCF might be a preferred polymer due to its larger shift. Alternatively, the chiralities dispersed using the PFO-BPy would be preferred for 532 nm detection via threshold voltage.

4.3.3. OVSED Modeling

In the previous section, the characterizations were determined using the Shichman-Hodges model[55] as it is classically used and sometimes called the Metal Oxide Semiconducting Field Effect Transistor (MOSFET) model. However, recent works have discussed its potential pitfalls and the benefits of using the MOSFET model in collaboration with more advanced models. [56–59] Thus, for

better completeness, 4-6 devices for each wavelength and polymer type were analysed using the Organic Virtual Source Emission Diffusion model (OVSED) .[60–62] The model provides the extraction of more parameters and better curve fitting.

Table 4.1 shows the average differences for each parameter from the model during both phases, averaged over all wavelengths and dispersion types. All parameters except for the V_T are normalized using their pre-soaked values. From this model, there are 2 parameters of interest, V_T and λ, both will help validate the previously observed trends, since V_T has a similar definition as the voltage-independent threshold voltage and λ is directly related to μ_e and the mean free path λ_f:

$$\lambda = L_G/\lambda_f \tag{4.2}$$

$$\mu = \frac{\nu_T}{2V_{temp}}\lambda_f \tag{4.3}$$

Where L_G is the gate length, υ_T is the carrier velocity and V_{temp} is the thermal voltage. Table 4.E2 and E3 show these two parameters for each wavelength and each polymer.

Model Parameter Differences	Soaking	Photo Cycling
V_T (V)	7.9±0.9	3.6±0.6
λ	-0.13±0.06	0.07±0.03

Table 4.1) *Average difference in extracted OVSED model parameters for all three SWNT based TFTs. V_T is the threshold voltage, λ is the ratio between the channel length and mean free path. The λ parameter is normalized using the pre-soaked value. Data extracted from 4-6 devices for each wavelength and polymer, totalling 46 devices, all were illuminated using an intensity of 4W/cm^2.*

From these results we can conclude that the model is in good agreement with the results using the SH model. The threshold voltage drastically increases during the initial exposure, the Soaking, and again during repeated exposures, the Photo Cycling, but to less of an extent. The λ decreases by 13 % during the soaking, this is equivalent to an increase in mobility of 13 % with other parameters

staying constant. Since the gate length stays constant, this indicates that the mean free path increases after being exposed. During the Photo Cycling, λ doesn't change as much, similarly to the mobility calculated via the SH model. It has been reported that annealing multiwalled carbon nanotubes, decreases the number of defects and improves crystallinity, thus increasing the mean free path.[63,64] This further drives the concept that the laser is potentially simulating a semi-permanent annealing.

4.4. Conclusion

In conclusion, we measured critical transistor metrics for several polymer-dispersed SWNT TFTs pre- and post-exposure to repeated selective wavelengths and have demonstrated that choice of wrapping polymer and SWNT chirality both matter. After an initial exposure, the Soaking, the devices reported higher mobilities, lower V_T, and lower off-current or reversed bias/dark currents. The exposure to light in combination with a gate voltage releases unbound excitons, which in turn may reduce the activation energy required to activate the device, thus V_T decreases after exposure. This was observed whenever the devices were exposed. In addition, the decreased dark currents could be attributed to excitons, which can fill charge traps in the channel through charge separation.[51–54] The drastic shift in mobility during the soaking process could be attributed to minor laser annealing which has been reported to reduce the channel resistance.[49] After the Soaking, the devices continued to behave similarly when the laser was On (On Cycling) with reduced V_T and dark current. The mobilities did not significantly change during the post-exposure periods. Although most devices performed similarly, the three different types of polymer-sc-SWNTs were influenced to different degrees of intensity due to slight differences in dispersed SWNT chirality, depending on the laser's wavelength. This was observed when the laser's wavelength was closer to the polymer's excitation, implying that choice of wrapping polymer, in addition to SWNT

chirality, matters when considering TFT performance. Further research should compare results from SWNT-based TFTs with a different separation technique and control for possible air dopants. A note should also be made in terms of the reproducibility of the behavior after the soak. Each repeated exposure measurement followed the same exposure *I-V* curve and post-exposure continued to show the same post-exposure curve. This gives great motivation for SWNT based TFT photodetectors for integration in textiles or flexible electronics.

4.5. Materials and Methods

4.5.1. Wafer Preparation

Pre-diced Si/SiO_2 wafers with 300 nm oxide (purchased from Ossila) were sonicated for five minutes each in a solution of Alconex detergent and water, deionized water, acetone, and methanol using a 2.8 L VWR Ultrasonic Cleaner Bath Sonicator. The substrates were subsequently dried using N_2 gas and treated in air plasma for fifteen minutes. Next, the wafers were rinsed with deionized water and isopropanol and dried with N_2. The wafers were immersed in a solution of 1% (v/v) octyltrichlorosilane (OTS) in anhydrous toluene, both purchased from Sigma-Aldrich, and heated at 70°C for 12 hrs before rinsing with toluene and drying under vacuum for an hour.

4.5.2. Single-Walled Carbon Nanotube Dispersion Preparation

Raw plasma-torch synthesized single-walled carbon nanotubes (SWNTs) were purchased from Raymor Nanointegris (Batch: RNB738-120, diameter: 0.9 − 1.5 nm, length: 0.3 − 4 μm). PCF and PFMB were synthesized using previously reported procedures.[63] Poly[(9,9-dioctylfluorenyl-2,7-diyl)-alt-co-(6,6′-{2,2′-bipyridine})] (PFO-BPy) was purchased from American Dye Source. The

polymers' molecular weights and dispersities are 65 kg/mol and 2.7 for PCF, 89 kg/mol and 1.9 for PFMB, and 43 kg/mol and 1.9 for PFO-BPy.

Raw SWNTs and polymer were combined in a vial with 20 mL of toluene at a specific polymer: SWNT weight ratio (0.8: 1 for PCF, 1.2: 1 for PFMB, and 0.8: 1 for PFO-BPy).[13] The samples were sonicated for 90 minutes (chilled with ice) and centrifuged for 15 minutes at 15,000 g and 10ºC (Thermo Scientific Sorvall ST 16R centrifuge, equipped with a Fiberlite F15 Fixed Angle rotor). The supernatant was removed, which consisted of polymer-wrapped sc-SWNTs and excess unbound wrapping polymer was dissolved in toluene. A silica gel treatment was incorporated as a further purification step.[65] 20-25 mg of silica gel was added to each sc-SWNT dispersion. The dispersions were sonicated for 45 minutes (chilled), left on the lab bench for three hours in ambient conditions, and centrifuged (15,000 g, 15 minutes, 10ºC). Raman spectroscopy was used to confirm sc-SWNT purity (Renishaw InVia Laser Raman Spectrometer) with 514, 633, and 785 nm laser excitation wavelengths.[15,66] Samples for Raman spectroscopy were prepared by drop-casting sc-SWNT dispersion onto a cleaned SiO_2 wafer until a dense mat of SWNTs was observed. Raw SWNT samples were prepared by sonicating in chloroform and drop-casting onto SiO_2 wafers.

Prior to TFT fabrication, the SWNT concentration was adjusted by adding toluene and measuring the UV-vis-NIR absorption spectra (Cary 5000 spectrometer in dual-beam mode, 10 mm quartz cuvette) until the S_{22} peak intensity at ~937 nm reached 2.0 a.u. The dispersion was sonicated for 10 minutes. SWNT dispersion was drop-casted onto OTS-treated wafers in 0.5 μL drops using a Musashi SHOT Mini 200Sx equipped with a Nano Master SMP-III dispenser (one drop per TFT, 20 TFTs per wafer). After drop-casting, each wafer was blown dry with a steady

stream of N_2 and rinsed with toluene four times in 1 mL increments at a ~45º angle, blowing dry with N_2 between each rinse. Previous work from our group showed that a toluene rinse was sufficient to remove most of the excess, unbound wrapping polymer from the sc-SWNT film.[79] The sc-SWNT films were annealed in air at 200ºC for one hour. Source-drain contacts were deposited on top of the sc-SWNT films *via* physical vapour deposition (Angstrom Engineering EvoVac Thermal Evaporator) with shadow masks (L = 30 μm, W = 1000 μm, purchased from Ossila). 10 nm of Mn was deposited to improve adhesion followed by 50 nm of Au (99.99 %, Angstrom Engineering, Inc.)[15] at a rate of 1 Å/s for both metals. All solvents were purchased from commercial suppliers and used as received, unless otherwise specified.

4.5.3. Sample Characterization and Exposure

Atomic Force Microscopy scans of each device type were taken using a ScanAsyst Air tip in Bruker ScanAsyst mode using a Dimension Icon Atomic Force Microscope at a rate of 1 Hz with a resolution of 512 scans per line. The scan area is 5 x 5 μm with a maximum height of 7.5 nm (**Figure 4.E6**).

The optical setup is composed of three continuous-wave lasers: the first laser (λ = 405 nm) has a maximum power of 200 mW and a beam diameter of 2.5 mm; the second (λ = 532 nm) is 400 mW and 0.7 mm; and the third (λ = 980 nm) is 2 W and 5 mm × 8 mm. A beam expander consisting of a Galilean telescope, a variable neutral density (ND) filter, and a photodiode were used to maintain a consistent beam size and intensity. The laser intensity on the sample was 0.04-4 W/cm^2 with 0.04 and 0.4 W/cm^2 only being displayed in the SI.

Current-voltage (*I-V*) output and transfer characteristics were measured for each device using a Keithley 2614B Sourcemeter with a custom LabVIEW program. Four transfer curves were collected for each device. Output curves were measured by sweeping the drain-source voltage

(V_{DS}) from 10 V to -30 V at a constant gate-source (V_{GS}) voltage, and repeating the V_{DS} sweep for an incremental increase in V_{GS} (V_{GS} range: 10 V to -30 V in 10 V increments). Transfer curves were measured in the linear regime by sweeping the V_{GS} from 60 V to -60 V (V_{DS} = -3 V). Baseline *p*-type characteristics for each device were measured in air at room temperature, without laser exposure. After the baselines were measured, the first TFT was exposed to a laser at a chosen wavelength and intensity, then measured during exposure with the same *I-V* parameters as the baseline. After the *I-V* curves were measured under the exposed conditions, the beam was blocked, and the device's *I-V* profile was measured again. Each exposure lasted only as long as the measurement time, approximately 1 minute. The process was repeated until three exposure profiles and two post-exposure profiles were recorded. To calculate the mobility and the threshold voltage, the well-established Shichman-Hodges[55] model (SH) model was used.

$$I_{DS_{sat}} = \frac{\mu W C_i}{2L}(V_{GS} - V_T)^2 \tag{4.4}$$

$$I_{DS_{lin}} = \frac{\mu W C_i V_{DS}}{L}\left(V_{GS} - V_T - \frac{V_{DS}}{2}\right) \tag{4.5}$$

$$C_i = k_d \cdot \varepsilon_o / t_t \tag{4.6}$$

I_{DS} is the source-drain current, L is the channel length, W is the channel width, V_T is the threshold voltage, μ is the charge carrier mobility, and C_i is the capacitance density, k_d is the dielectric constant, ε_o is the vacuum permittivity, and t_t is the dielectric thickness. The mobility was extracted from the slope of the transfer curve at high V_{GS} ($\partial I_{DS}/\partial V_{GS}$, Equation 4.5) with corrected channel lengths and widths measured via optical microscope. The threshold voltage was calculated from the x-intercept of the extrapolated linear fit.

$$\mu = \frac{L}{WC_iV_{DS}}\left(\frac{\partial I_{DS}}{\partial V_{GS}}\right) \tag{4.7}$$

The OVSED model was applied using least squares fit programmed in python code using the equations as described in the manuscripts by Dallaire et al. and Blawid et al.[60,61]

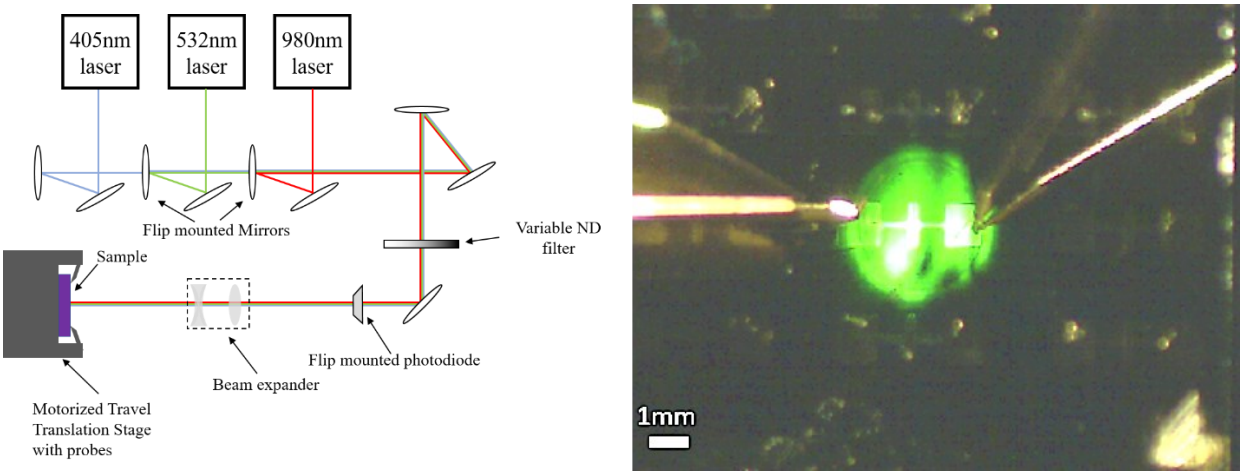

***Figure 4.5**: a) Top-view schematic of the optical setup used in this work. The motorized travel translation state with probes is attached to a Keithley and a computer to measure the performance and control the movement. b) An image of a single walled carbon nanotube device being irradiated with the 532 nm laser.*

4.6. References

(1) Schnorr, J. M.; Swager, T. M. Emerging Applications of Carbon Nanotubes. *Chemistry of Materials* **2011**, *23* (3), 646–657. https://doi.org/10.1021/cm102406h.

(2) Zhang, S.; Cai, L.; Wang, T.; Miao, J.; Sepúlveda, N.; Wang, C. Fully Printed Flexible Carbon Nanotube Photodetectors. *Appl Phys Lett* **2017**, *110* (12), 123105. https://doi.org/10.1063/1.4978935.

(3) Zheng, Y.; Kim, Y.; Jones, A. C.; Olinger, G.; Bittner, E. R.; Bachilo, S. M.; Doorn, S. K.; Weisman, R. B.; Piryatinski, A.; Htoon, H. Quantum Light Emission from Coupled Defect States in DNA-Functionalized Carbon Nanotubes. *ACS Nano* **2021**, *15* (6), 10406–10414. https://doi.org/10.1021/acsnano.1c02709.

(4) Ma, X.; Hartmann, N. F.; Baldwin, J. K. S.; Doorn, S. K.; Htoon, H. Room-Temperature Single-Photon Generation from Solitary Dopants of Carbon Nanotubes. *Nat Nanotechnol* **2015**, *10* (8), 671–675. https://doi.org/10.1038/nnano.2015.136.

(5) Li, M.-K.; Riaz, A.; Wederhake, M.; Fink, K.; Saha, A.; Dehm, S.; He, X.; Schöppler, F.; Kappes, M. M.; Htoon, H.; Popov, V. N.; Doorn, S. K.; Hertel, T.; Hennrich, F.; Krupke, R. Electroluminescence from Single-Walled Carbon Nanotubes with Quantum Defects. *ACS Nano* **2022**, *16* (8), 11742–11754. https://doi.org/10.1021/acsnano.2c03083.

(6) Chen, J.-S.; Dasgupta, A.; Morrow, D. J.; Emmanuele, R.; Marks, T. J.; Hersam, M. C.; Ma, X. Room Temperature Lasing from Semiconducting Single-Walled Carbon Nanotubes. *ACS Nano* **2022**, *16* (10), 16776–16783. https://doi.org/10.1021/acsnano.2c06419.

(7) Huang, H.; Wang, F.; Liu, Y.; Wang, S.; Peng, L.-M. Plasmonic Enhanced Performance of an Infrared Detector Based on Carbon Nanotube Films. *ACS Appl Mater Interfaces* **2017**, *9* (14), 12743–12749. https://doi.org/10.1021/acsami.7b01301.

(8) Lee, J. U. Photovoltaic Effect in Ideal Carbon Nanotube Diodes. *Appl Phys Lett* **2005**, *87* (7), 073101. https://doi.org/10.1063/1.2010598.

(9) Saito, R.; Fujita, M.; Dresselhaus, G.; Dresselhaus, M. S. Electronic Structure of Chiral Graphene Tubules. *Appl Phys Lett* **1992**, *60* (18), 2204–2206. https://doi.org/10.1063/1.107080.

(10) Gomulya, W.; Costanzo, G. D.; de Carvalho, E. J. F.; Bisri, S. Z.; Derenskyi, V.; Fritsch, M.; Fröhlich, N.; Allard, S.; Gordiichuk, P.; Herrmann, A.; Marrink, S. J.; dos Santos, M. C.; Scherf, U.; Loi, M. A. Semiconducting Single-Walled Carbon Nanotubes on Demand by Polymer Wrapping. *Advanced Materials* **2013**, *25* (21), 2948–2956. https://doi.org/https://doi.org/10.1002/adma.201300267.

(11) Mistry, K. S.; Larsen, B. A.; Blackburn, J. L. High-Yield Dispersions of Large-Diameter Semiconducting Single-Walled Carbon Nanotubes with Tunable Narrow Chirality Distributions. *ACS Nano* **2013**, *7* (3), 2231–2239. https://doi.org/10.1021/nn305336x.

(12) Li, Z.; Ding, J.; Finnie, P.; Lefebvre, J.; Cheng, F.; Kingston, C. T.; Malenfant, P. R. L. Raman Microscopy Mapping for the Purity Assessment of Chirality Enriched Carbon Nanotube Networks in Thin-Film Transistors. *Nano Res* **2015**, *8* (7), 2179–2187. https://doi.org/10.1007/s12274-015-0725-y.

(13) Nish, A.; Hwang, J.-Y.; Doig, J.; Nicholas, R. J. Highly Selective Dispersion of Single-Walled Carbon Nanotubes Using Aromatic Polymers. *Nat Nanotechnol* **2007**, *2* (10), 640–646. https://doi.org/10.1038/nnano.2007.290.

(14) Lei, T.; Shao, L.-L.; Zheng, Y.-Q.; Pitner, G.; Fang, G.; Zhu, C.; Li, S.; Beausoleil, R.; Wong, H.-S. P.; Huang, T.-C.; Cheng, K.-T.; Bao, Z. Low-Voltage High-Performance Flexible Digital and Analog Circuits Based on Ultrahigh-Purity Semiconducting Carbon Nanotubes. *Nat Commun* **2019**, *10* (1), 2161. https://doi.org/10.1038/s41467-019-10145-9.

(15) Rice, N. A.; Bodnaryk, W. J.; Mirka, B.; Melville, O. A.; Adronov, A.; Lessard, B. H. Polycarbazole-Sorted Semiconducting Single-Walled Carbon Nanotubes for Incorporation into Organic Thin Film Transistors. *Adv Electron Mater* **2019**, *5* (1), 1800539. https://doi.org/https://doi.org/10.1002/aelm.201800539.

(16) Liu, F.; Chen, X.; Xi, M.; Wei, N.; Bai, L.; Peng, L.; Cao, Y.; Liang, X. Comparative Study of the Extraction Selectivity of PFO-BPy and PCz for Small to Large Diameter Single-Walled Carbon Nanotubes. *Nano Res* **2022**, *15* (9), 8479–8485. https://doi.org/10.1007/s12274-022-4425-0.

(17) Wang, H.; Bao, Z. Conjugated Polymer Sorting of Semiconducting Carbon Nanotubes and Their Electronic Applications. *Nano Today* **2015**, *10* (6), 737–758. https://doi.org/https://doi.org/10.1016/j.nantod.2015.11.008.

(18) Brady, G. J.; Way, A. J.; Safron, N. S.; Evensen, H. T.; Gopalan, P.; Arnold, M. S. Quasi-Ballistic Carbon Nanotube Array Transistors with Current Density Exceeding Si and GaAs. *Sci Adv* **2016**, *2* (9), e1601240. https://doi.org/10.1126/sciadv.1601240.

(19) Ouyang, J.; Ding, J.; Lefebvre, J.; Li, Z.; Guo, C.; Kell, A. J.; Malenfant, P. R. L. Sorting of Semiconducting Single-Walled Carbon Nanotubes in Polar Solvents with an Amphiphilic Conjugated Polymer Provides General Guidelines for Enrichment. *ACS Nano* **2018**, *12* (2), 1910–1919. https://doi.org/10.1021/acsnano.7b08818.

(20) Park, S.; Pitner, G.; Giri, G.; Koo, J. H.; Park, J.; Kim, K.; Wang, H.; Sinclair, R.; Wong, H.-S. P.; Bao, Z. Large-Area Assembly of Densely Aligned Single-Walled Carbon Nanotubes Using Solution Shearing and Their Application to Field-Effect Transistors. *Advanced Materials* **2015**, *27* (16), 2656–2662. https://doi.org/https://doi.org/10.1002/adma.201405289.

(21) Cao, C.; Andrews, J. B.; Franklin, A. D. Completely Printed, Flexible, Stable, and Hysteresis-Free Carbon Nanotube Thin-Film Transistors via Aerosol Jet Printing. *Adv Electron Mater* **2017**, *3* (5), 1700057. https://doi.org/https://doi.org/10.1002/aelm.201700057.

(22) Bucella, S. G.; Salazar-Rios, J. M.; Derenskyi, V.; Fritsch, M.; Scherf, U.; Loi, M. A.; Caironi, M. Inkjet Printed Single-Walled Carbon Nanotube Based Ambipolar and Unipolar Transistors for High-Performance Complementary Logic Circuits. *Adv Electron Mater* **2016**, *2* (6), 1600094. https://doi.org/https://doi.org/10.1002/aelm.201600094.

(23) Rother, M.; Brohmann, M.; Yang, S.; Grimm, S. B.; Schießl, S. P.; Graf, A.; Zaumseil, J. Aerosol-Jet Printing of Polymer-Sorted (6,5) Carbon Nanotubes for Field-Effect Transistors with High Reproducibility. *Adv Electron Mater* **2017**, *3* (8), 1700080. https://doi.org/https://doi.org/10.1002/aelm.201700080.

(24) Doshi, S. M.; Thostenson, E. T. Thin and Flexible Carbon Nanotube-Based Pressure Sensors with Ultrawide Sensing Range. *ACS Sens* **2018**, *3* (7), 1276–1282. https://doi.org/10.1021/acssensors.8b00378.

(25) García Núñez, C.; Manjakkal, L.; Dahiya, R. Energy Autonomous Electronic Skin. *npj Flexible Electronics* **2019**, *3* (1), 1. https://doi.org/10.1038/s41528-018-0045-x.

(26) Maroto, A.; Balasubramanian, K.; Burghard, M.; Kern, K. Functionalized Metallic Carbon Nanotube Devices for PH Sensing. *ChemPhysChem* **2007**, *8* (2), 220–223. https://doi.org/https://doi.org/10.1002/cphc.200600498.

(27) Schroeder, V.; Savagatrup, S.; He, M.; Lin, S.; Swager, T. M. Carbon Nanotube Chemical Sensors. *Chem Rev* **2019**, *119* (1), 599–663. https://doi.org/10.1021/acs.chemrev.8b00340.

(28) Lapointe, F.; Ding, J.; Lefebvre, J. Carbon Nanotube Transistors as Gas Sensors: Response Differentiation Using Polymer Gate Dielectrics. *ACS Appl Polym Mater* **2019**, *1* (12), 3269–3278. https://doi.org/10.1021/acsapm.9b00707.

(29) Wang, C.; Takei, K.; Takahashi, T.; Javey, A. Carbon Nanotube Electronics – Moving Forward. *Chem. Soc. Rev.* **2013**, *42* (7), 2592–2609. https://doi.org/10.1039/C2CS35325C.

(30) Mitin, D.; Berdnikov, Y.; Vorobyev, A.; Mozharov, A.; Raudik, S.; Koval, O.; Neplokh, V.; Moiseev, E.; Ilatovskii, D.; Nasibulin, A. G.; Mukhin, I. Optimization of Optoelectronic Properties of Patterned Single-Walled Carbon Nanotube Films. *ACS Appl Mater Interfaces* **2020**, *12* (49), 55141–55147. https://doi.org/10.1021/acsami.0c14783.

(31) Zhang, S.; Cai, L.; Wang, T.; Shi, R.; Miao, J.; Wei, L.; Chen, Y.; Sepúlveda, N.; Wang, C. Bolometric-Effect-Based Wavelength-Selective Photodetectors Using Sorted Single Chirality Carbon Nanotubes. *Sci Rep* **2015**, *5* (1), 17883. https://doi.org/10.1038/srep17883.

(32) Hao, J.; Lu, H.; Mao, L.; Chen, X.; Beard, M. C.; Blackburn, J. L. Direct Detection of Circularly Polarized Light Using Chiral Copper Chloride–Carbon Nanotube Heterostructures. *ACS Nano* **2021**, *15* (4), 7608–7617. https://doi.org/10.1021/acsnano.1c01134.

(33) Yin, H.; Zhang, L.; Zhu, M.; Chen, Y.; Tian, T.; Zhang, Y.; Hu, N.; Yang, Z.; Su, Y. High-Performance Visible–Near-Infrared Single-Walled Carbon Nanotube Photodetectors via Interfacial Charge-Transfer-Induced Improvement by Surface Doping. *ACS Appl Mater Interfaces* **2022**, *14* (38), 43628–43636. https://doi.org/10.1021/acsami.2c12415.

(34) He, X.; Léonard, F.; Kono, J. Uncooled Carbon Nanotube Photodetectors. *Adv Opt Mater* **2015**, *3* (8), 989–1011. https://doi.org/https://doi.org/10.1002/adom.201500237.

(35) Stranks, S. D.; Weisspfennig, C.; Parkinson, P.; Johnston, M. B.; Herz, L. M.; Nicholas, R. J. Ultrafast Charge Separation at a Polymer−Single-Walled Carbon Nanotube Molecular Junction. *Nano Lett* **2011**, *11* (1), 66–72. https://doi.org/10.1021/nl1036484.

(36) Kahmann, S.; Salazar Rios, J. M.; Zink, M.; Allard, S.; Scherf, U.; dos Santos, M. C.; Brabec, C. J.; Loi, M. A. Excited-State Interaction of Semiconducting Single-Walled Carbon Nanotubes with Their Wrapping Polymers. *J Phys Chem Lett* **2017**, *8* (22), 5666–5672. https://doi.org/10.1021/acs.jpclett.7b02553.

(37) Kuang, Z.; Berger, F. J.; Lustres, J. L. P.; Wollscheid, N.; Li, H.; Lüttgens, J.; Leinen, M. B.; Flavel, B. S.; Zaumseil, J.; Buckup, T. Charge Transfer from Photoexcited Semiconducting Single-Walled Carbon Nanotubes to Wide-Bandgap Wrapping Polymer. *The Journal of Physical Chemistry C* **2021**, *125* (15), 8125–8136. https://doi.org/10.1021/acs.jpcc.0c10171.

(38) Hwang, J.-Y.; Nish, A.; Doig, J.; Douven, S.; Chen, C.-W.; Chen, L.-C.; Nicholas, R. J. Polymer Structure and Solvent Effects on the Selective Dispersion of Single-Walled Carbon Nanotubes. *J Am Chem Soc* **2008**, *130* (11), 3543–3553. https://doi.org/10.1021/ja0777640.

(39) Fong, D.; Bodnaryk, W. J.; Rice, N. A.; Saem, S.; Moran-Mirabal, J. M.; Adronov, A. Influence of Polymer Electronics on Selective Dispersion of Single-Walled Carbon Nanotubes. *Chemistry – A European Journal* **2016**, *22* (41), 14560–14566. https://doi.org/https://doi.org/10.1002/chem.201602722.

(40) Mirka, B.; Rice, N. A.; Williams, P.; Tousignant, M. N.; Boileau, N. T.; Bodnaryk, W. J.; Fong, D.; Adronov, A.; Lessard, B. H. Excess Polymer in Single-Walled Carbon Nanotube Thin-Film Transistors: Its Removal Prior to Fabrication Is Unnecessary. *ACS Nano* **2021**, *15* (5), 8252–8266. https://doi.org/10.1021/acsnano.0c08584.

(41) Arias, D. H.; Sulas-Kern, D. B.; Hart, S. M.; Kang, H. S.; Hao, J.; Ihly, R.; Johnson, J. C.; Blackburn, J. L.; Ferguson, A. J. Effect of Nanotube Coupling on Exciton Transport in Polymer-Free Monochiral Semiconducting Carbon Nanotube Networks. *Nanoscale* **2019**, *11* (44), 21196–21206. https://doi.org/10.1039/C9NR07821E.

(42) Qiu, X.; Freitag, M.; Perebeinos, V.; Avouris, P. Photoconductivity Spectra of Single-Carbon Nanotubes: Implications on the Nature of Their Excited States. *Nano Lett* **2005**, *5* (4), 749–752. https://doi.org/10.1021/nl050227y.

(43) Beaupré, S.; Boudreault, P.-L. T.; Leclerc, M. Solar-Energy Production and Energy-Efficient Lighting: Photovoltaic Devices and White-Light-Emitting Diodes Using Poly(2,7-Fluorene), Poly(2,7-Carbazole), and Poly(2,7-Dibenzosilole) Derivatives. *Advanced Materials* **2010**, *22* (8), E6–E27. https://doi.org/https://doi.org/10.1002/adma.200903484.

(44) Li, J.; Grimsdale, A. C. Carbazole-Based Polymers for Organic Photovoltaic Devices. *Chem. Soc. Rev.* **2010**, *39* (7), 2399–2410. https://doi.org/10.1039/B915995A.

(45) Sotzing, G. A.; Reddinger, J. L.; Katritzky, A. R.; Soloducho, J.; Musgrave, R.; Reynolds, J. R.; Steel, P. J. Multiply Colored Electrochromic Carbazole-Based Polymers. *Chemistry of Materials* **1997**, *9* (7), 1578–1587. https://doi.org/10.1021/cm960630t.

(46) Ozawa, H.; Ide, N.; Fujigaya, T.; Niidome, Y.; Nakashima, N. One-Pot Separation of Highly Enriched (6,5)-Single-Walled Carbon Nanotubes Using a Fluorene-Based Copolymer. *Chem Lett* **2011**, *40* (3), 239–241. https://doi.org/10.1246/cl.2011.239.

(47) Aguirre, C. M.; Levesque, P. L.; Paillet, M.; Lapointe, F.; St-Antoine, B. C.; Desjardins, P.; Martel, R. The Role of the Oxygen/Water Redox Couple in Suppressing Electron Conduction in Field-Effect Transistors. *Advanced Materials* **2009**, *21* (30), 3087–3091. https://doi.org/https://doi.org/10.1002/adma.200900550.

(48) Ding, J.; Li, Z.; Lefebvre, J.; Du, X.; Malenfant, P. R. L. Mechanistic Consideration of PH Effect on the Enrichment of Semiconducting SWCNTs by Conjugated Polymer Extraction. *The Journal of Physical Chemistry C* **2016**, *120* (38), 21946–21954. https://doi.org/10.1021/acs.jpcc.6b05965.

(49) Souza, N.; Roble, M.; Diaz-Droguett, D. E.; Mücklich, F. Scaling up Single-Wall Carbon Nanotube Laser Annealing: Effect on Electrical Resistance and Hydrogen Adsorption. *RSC Adv.* **2017**, *7* (9), 5084–5092. https://doi.org/10.1039/C6RA27794B.

(50) T Dürkop; B M Kim; M S Fuhrer. Properties and Applications of High-Mobility Semiconducting Nanotubes. *Journal of Physics: Condensed Matter* **2004**, *16* (18), R553. https://doi.org/10.1088/0953-8984/16/18/R01.

(51) Jang, W.; Kim, B. G.; Seo, S.; Shawky, A.; Kim, M. S.; Kim, K.; Mikladal, B.; Kauppinen, E. I.; Maruyama, S.; Jeon, I.; Wang, D. H. Strong Dark Current Suppression in Flexible Organic Photodetectors by Carbon Nanotube Transparent Electrodes. *Nano Today* **2021**, *37*, 101081. https://doi.org/https://doi.org/10.1016/j.nantod.2021.101081.

(52) Zhu, X.-Y.; Yang, Q.; Muntwiler, M. Charge-Transfer Excitons at Organic Semiconductor Surfaces and Interfaces. *Acc Chem Res* **2009**, *42* (11), 1779–1787. https://doi.org/10.1021/ar800269u.

(53) Sista, S.; Yao, Y.; Yang, Y.; Tang, M. L.; Bao, Z. Enhancement in Open Circuit Voltage through a Cascade-Type Energy Band Structure. *Appl Phys Lett* **2007**, *91* (22), 223508. https://doi.org/10.1063/1.2817935.

(54) Ravirajan, P.; Peiró, A. M.; Nazeeruddin, M. K.; Graetzel, M.; Bradley, D. D. C.; Durrant, J. R.; Nelson, J. Hybrid Polymer/Zinc Oxide Photovoltaic Devices with Vertically Oriented ZnO Nanorods and an Amphiphilic Molecular Interface Layer. *J Phys Chem B* **2006**, *110* (15), 7635–7639. https://doi.org/10.1021/jp0571372.

(55) Shichman, H.; Hodges, D. A. Modeling and Simulation of Insulated-Gate Field-Effect Transistor Switching Circuits. *IEEE J Solid-State Circuits* **1968**, *3* (3), 285–289. https://doi.org/10.1109/JSSC.1968.1049902.

(56) Paterson, A. F.; Singh, S.; Fallon, K. J.; Hodsden, T.; Han, Y.; Schroeder, B. C.; Bronstein, H.; Heeney, M.; McCulloch, I.; Anthopoulos, T. D. Recent Progress in High-Mobility Organic Transistors: A Reality Check. *Adv Mater* **2018**, e1801079. https://doi.org/10.1002/adma.201801079.

(57) McCulloch, I.; Salleo, A.; Chabinyc, M. Avoid the Kinks When Measuring Mobility. *Science (1979)* **2016**, *352* (6293), 1521–1522. https://doi.org/10.1126/science.aaf9062.

(58) Bittle, E. G.; Basham, J. I.; Jackson, T. N.; Jurchescu, O. D.; Gundlach, D. J. Mobility Overestimation Due to Gated Contacts in Organic Field-Effect Transistors. *Nat Commun* **2016**, *7* (1), 10908. https://doi.org/10.1038/ncomms10908.

(59) Donnhäuser, S.; Pacheco-Sanchez, A.; Haase, K.; Mannsfeld, S. C. B.; Claus, M.; Blawid, S. Impact of Injection Limitations on the Contact Resistance and the Carrier Mobility of Organic Field Effect Transistors. *Org Electron* **2021**, *99*, 106343. https://doi.org/https://doi.org/10.1016/j.orgel.2021.106343.

(60) Blawid, S.; Dallaire, N. J.; Lessard, B. H. Self-Consistent Extraction of Mobility and Series Resistance: A Hierarchy of Models for Benchmarking Organic Thin-Film Transistors. *IEEE Journal on Flexible Electronics* **2022**, *1* (2), 114–121. https://doi.org/10.1109/JFLEX.2022.3165140.

(61) Dallaire, N. J.; Brixi, S.; Claus, M.; Blawid, S.; Lessard, B. H. Benchmarking Contact Quality in N-Type Organic Thin Film Transistors through an Improved Virtual-Source Emission-Diffusion Model. *Appl Phys Rev* **2022**, *9* (1), 11418. https://doi.org/10.1063/5.0078907.

(62) Lima, A. A.; Blawid, S. Modeling Organic Thin-Film Transistors Based on the Virtual Source Concept: A Case Study. *Solid State Electron* **2019**, *161*, 107639.

(63) Kajiura, H.; Nandyala, A.; Bezryadin, A. Quasi-Ballistic Electron Transport in as-Produced and Annealed Multiwall Carbon Nanotubes. *Carbon N Y* **2005**, *43* (6), 1317–1319. https://doi.org/https://doi.org/10.1016/j.carbon.2004.12.004.

(64) Elsehly, E. M.; Ibrahim, E. M. M.; El-Hadek, M. A.; El-Khouly, A.; Khovaylo, V.; Elqahtani, Z. M.; Chechenin, N. G.; Adam, A. M. Annealing Effect on the Thermoelectric Properties of

Multiwall Carbon Nanotubes. *Physica E Low Dimens Syst Nanostruct* **2023**, *146*, 115566. https://doi.org/https://doi.org/10.1016/j.physe.2022.115566.

(65) Ding, J.; Li, Z.; Lefebvre, J.; Cheng, F.; Dunford, J. L.; Malenfant, P. R. L.; Humes, J.; Kroeger, J. A Hybrid Enrichment Process Combining Conjugated Polymer Extraction and Silica Gel Adsorption for High Purity Semiconducting Single-Walled Carbon Nanotubes (SWCNT). *Nanoscale* **2015**, *7* (38), 15741–15747. https://doi.org/10.1039/C5NR04851F.

(66) Mirka, B.; Fong, D.; Rice, N. A.; Melville, O. A.; Adronov, A.; Lessard, B. H. Polyfluorene-Sorted Semiconducting Single-Walled Carbon Nanotubes for Applications in Thin-Film Transistors. *Chemistry of Materials* **2019**, *31* (8), 2863–2872. https://doi.org/10.1021/acs.chemmater.8b05357.

(67) Mirka, B.; Rice, N. A.; Richard, C. M.; Lefebvre, D.; King, B.; Bodnaryk, W. J.; Fong, D.; Adronov, A.; Lessard, B. H. Contact Engineering in Single-Walled Carbon Nanotube Thin-Film Transistors: Implications for Silane-Treated SiO2 Substrates. *ACS Appl Nano Mater* **2022**, *5* (9), 12487–12495. https://doi.org/10.1021/acsanm.2c02052.

4.7. Supporting Information

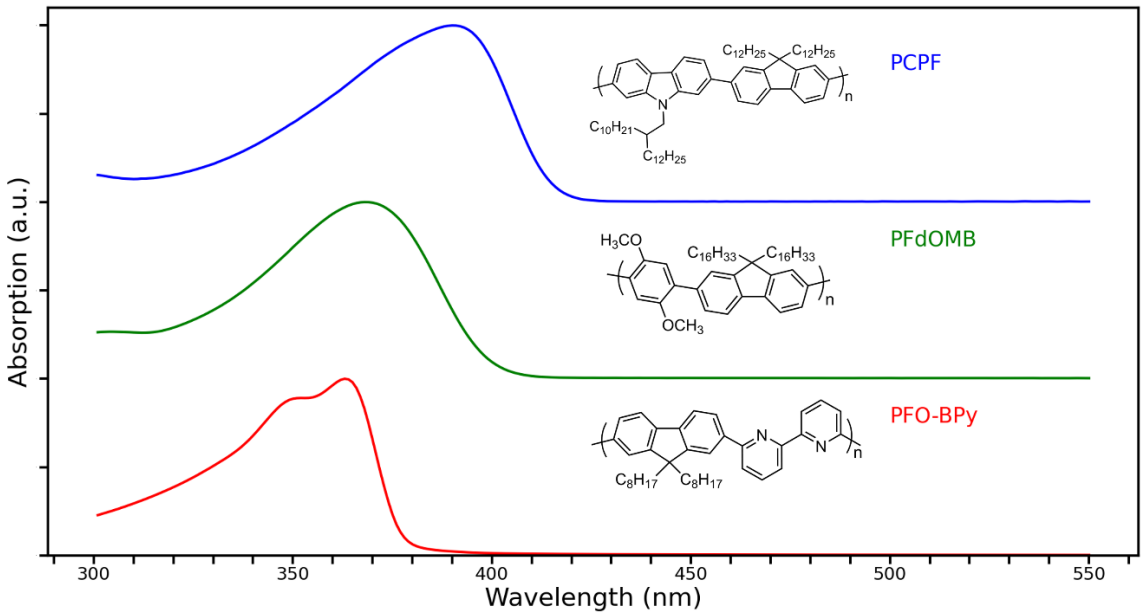

Figure 4.E1)*: Absorption Profile of each polymer. The polymer's structure is displayed over each corresponding absorption spectra.*

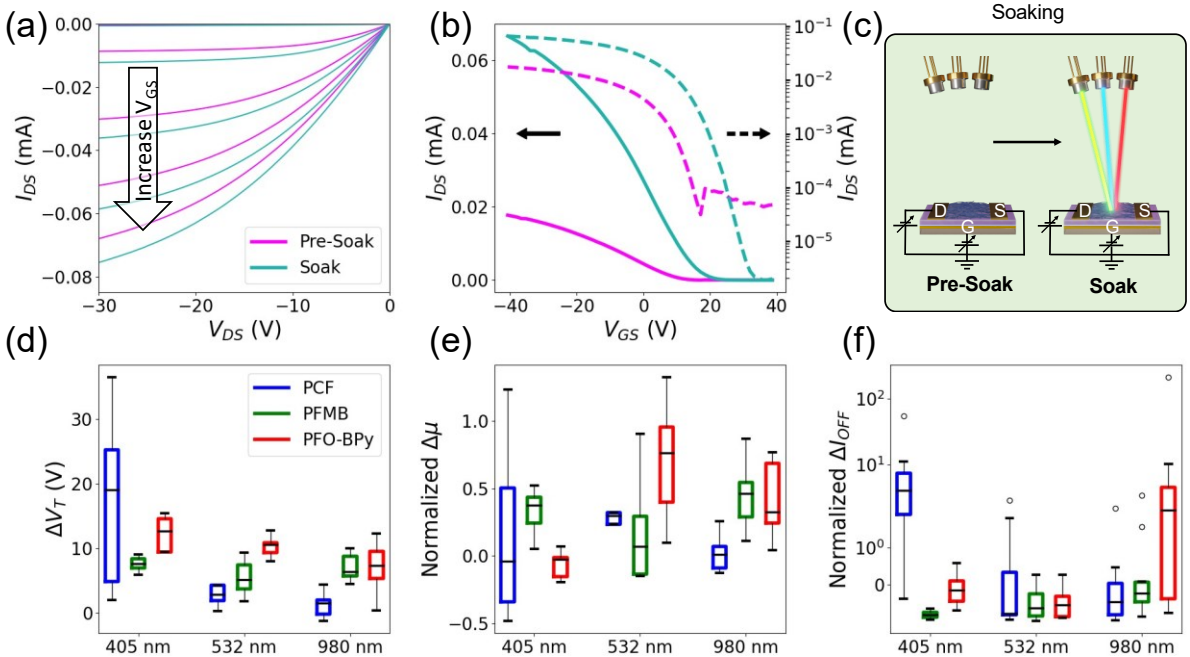

Figure 4.E2): Difference in performance between Off Cycling and On Cycling at 4W/cm^2. Characteristic output curves with gate voltages (10, 0, -10, -20 and -30 V) (a). Characteristic transfer curves of a PFMB-SWNT device illuminated at 405 nm,

linear curve (solid line) and logarithmic (dashed line) with V_{DS} = -3 V. (b). A procedural schematic of the Soaking process (c). Box plots of the average ΔV_T (d), average normalized $\Delta\mu$ (e) and the average normalized OFF current (f).

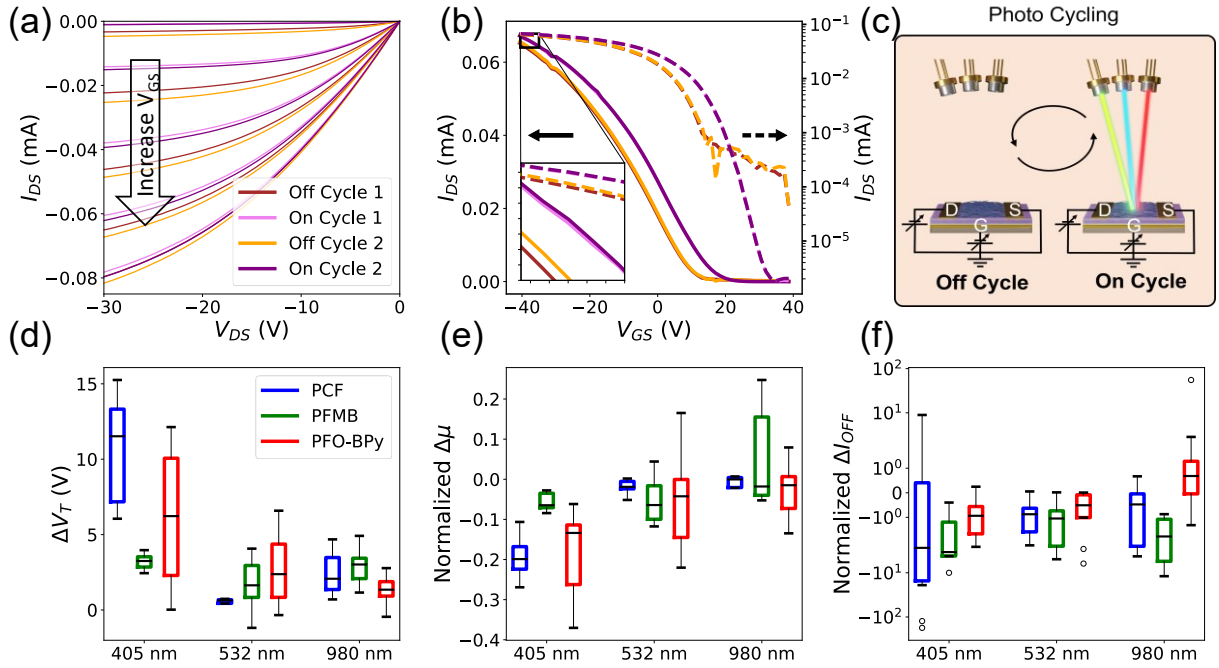

Figure 4.E3): Difference in performance between Pre-Soak and Soak at 4W/cm^2. Characteristic output curves with gate voltages (10, 0, -10, -20 and -30 V) (a). Characteristic transfer curves of a PFMB-SWNT device illuminated at 405 nm, linear curve (solid line) and logarithmic (dashed line) with V_{DS} = -3 V. (b). A procedural schematic of the Soaking process (c). Box plots of the average ΔV_T (d), average normalized $\Delta\mu$ (e) and the average normalized OFF current (f).

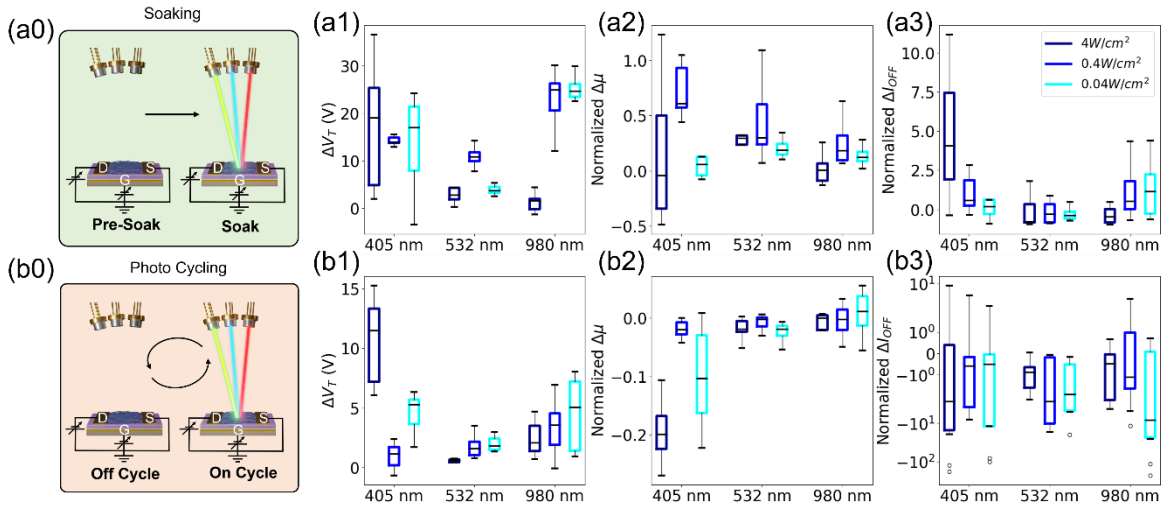

Figure 4.E4): Difference in performance between Pre-Soak and during Soak (a) and the difference in performance between Off and On exposure cycling at different intensities (b). (0) The procedural schematics of both processes. (1) The average

difference between the threshold voltage (2). The normalized difference for the mobility and (3) the average OFF current. All tests performed on SWNT OTFT using the PCF dispersion.

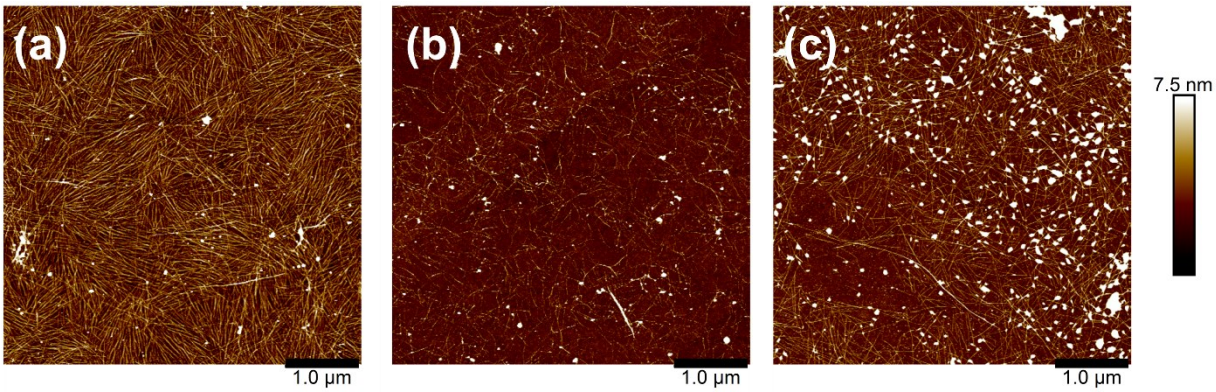

Figure 4.E5): Atomic force microscopy images of the SWNT devices, PCF (a), PFMB (b) and PFO-BPy (c), on Si wafers. The scans were performed using a ScanAsyst Air tip in Bruker ScanAsyst mode using a Dimension Icon Atomic Force Microscope at a rate of 1 Hz with a resolution of 512 scans per line. The scan area is 5 x 5 µm with a maximum height of 7.5 nm.

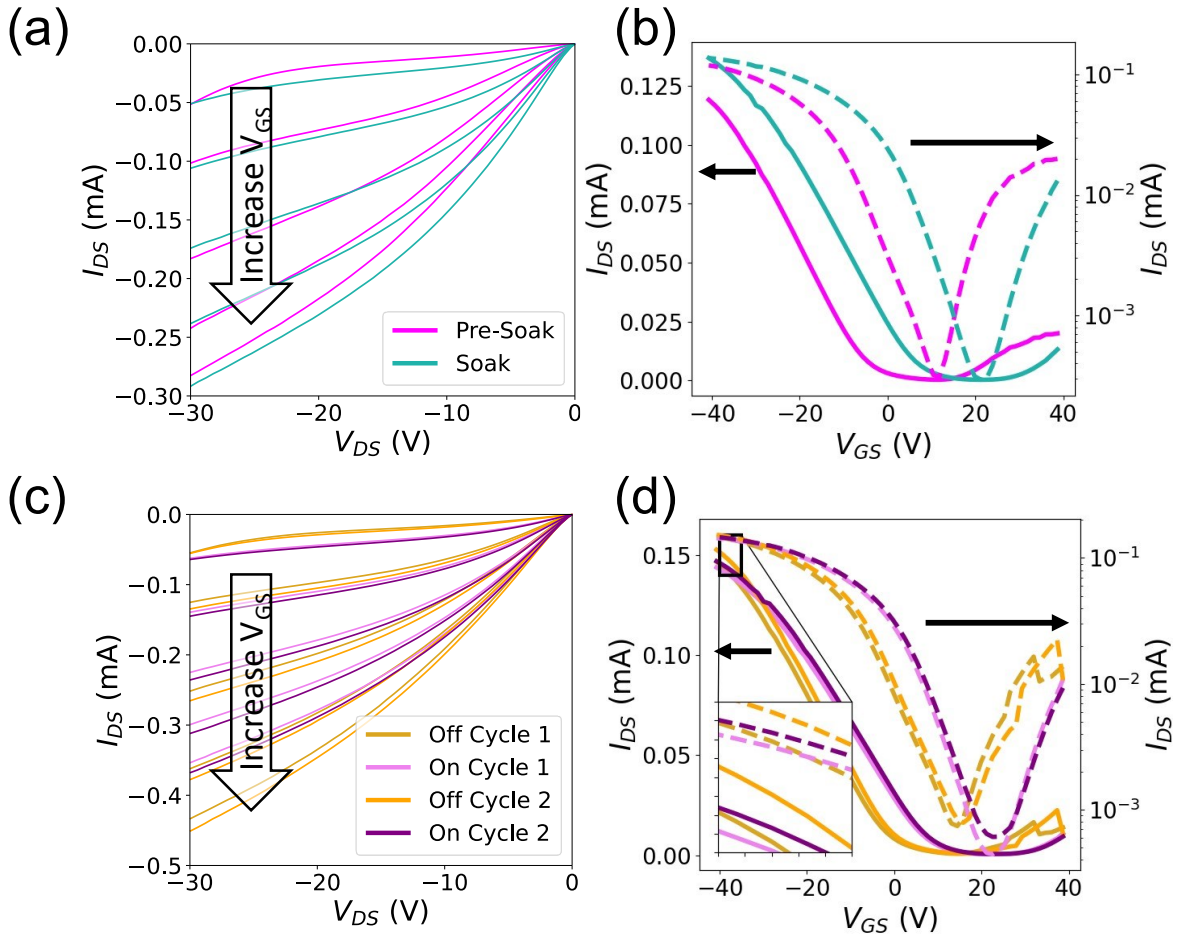

Figure 4.E6): Characteristic output and transfer curves of a PFO-BPy+SWNT device with exposure at 405 nm and 4W/cm^2 (a) The output curves during the Soaking phase with gate voltages (10, 0, -10, -20 and -30 V) (b) . The transfer curves with during the Soaking phase V_{DS}=-3 V . (c) The output curves during the Cycling phase with gate voltages (10, 0, -10, -20 and -30 V). (d) The transfer curves with during the Cycling phase V_{DS}=-3 V .

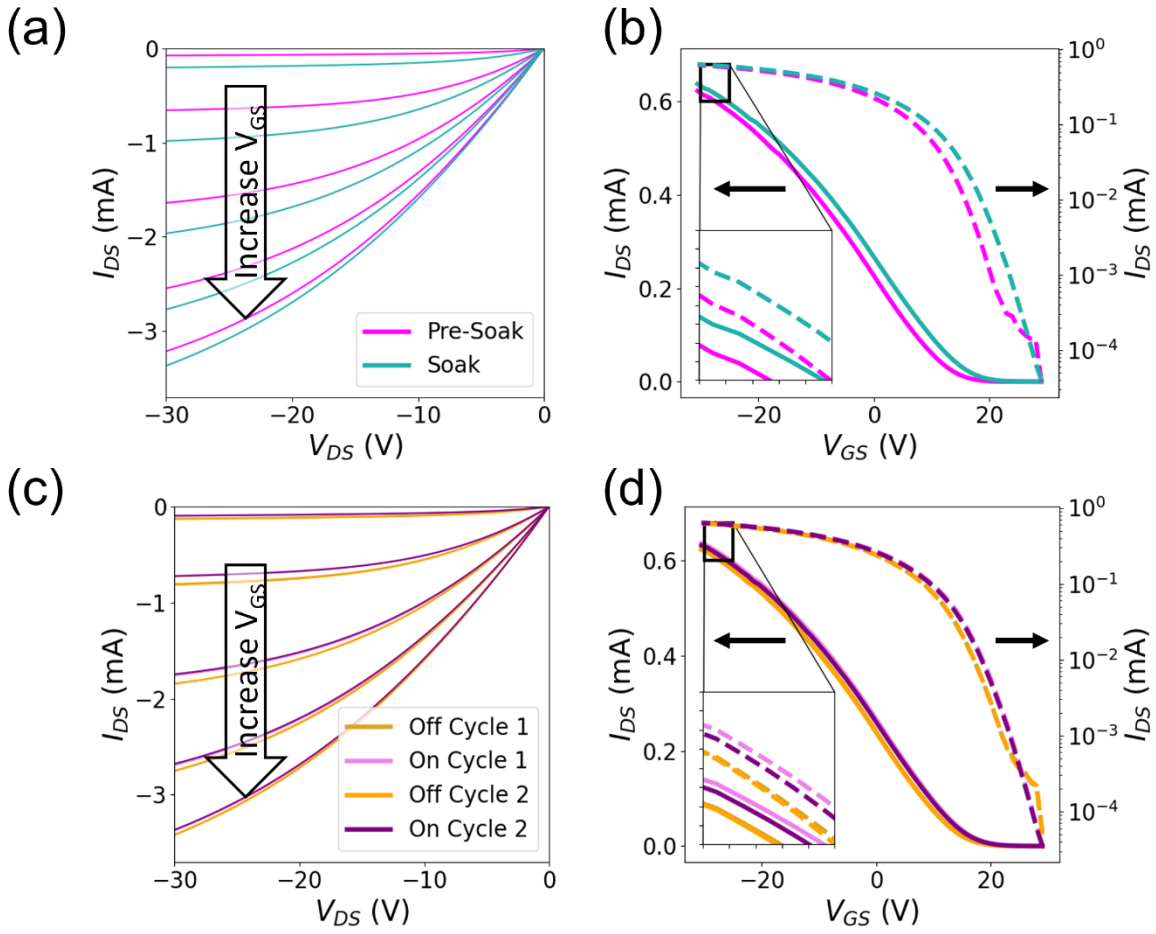

Figure 4.E7): Characteristic output and transfer curves of a PCF+SWNT device with exposure at 980 nm and 4W/cm^2 (a) The output curves during the Soaking phase with gate voltages (10, 0, -10, -20 and -30 V) (b) . The transfer curves with during the Soaking phase V_{DS}=-3 V . (c) The output curves during the Cycling phase with gate voltages (10, 0, -10, -20 and -30 V). (d) The transfer curves with during the Cycling phase V_{DS}=-3 V .

Model Parameter Differences	Soaking	Photo Cycling
V_T (V)	7.9±0.9	3.6±0.6
δ	5±3 x 10^7 E+07	3±2 x 10^7
n	0.05±0.06	-0.09±0.07
l	0.02±0.04	0.01±0.02
λ	-0.13±0.06	0.07±0.03
V_{gcrit}	130±70	30±40
J_T	4±3	-2±1
V_{tun}	4±3	-1±1
V_0	3000±3000	-300±200
R_0	60±40	-30±30

R_{max}	0.06±0.09	0.05±0.05

Table 4.E1) *Average Difference in extracted OVSED model parameters for all three SWNT based TFTs. V_T is the threshold voltage, δ a variable threshold constant, n is a gate coupling factor, l is a constant dependent on the density of trap states, λ is the ratio between the channel length and mean free path, V_{gcrit} is the critical voltage for carrier velocity saturation, J_T is the current density, V_0 is the turning point for the contact resistance, V_{tun} is the smoothing factor for the contact resistance, R_0 is the minimum contact resistance, R_{max} is the maximum contact resistance. All values except for V_T were normalized using their respective pre-soaked values. Data extracted from 4-6 devices for each wavelength and polymer, totalling 46 devices, all were illuminated using an intensity of 4W/cm^2.*

Model parameter differences	Soaking phase 405nm			Soaking phase 532nm			Soaking phase 980nm		
	PCF	PFMB	PFO-BPy	PCF	PFMB	PFO-BPy	PCF	PFMB	PFO-BPy
V_T (V)	17 ± 7	5 ± 3	10 ± 3	5 ± 1	7 ± 2	8.9±0.9	5.9 ± 0.6	8 ± 3	8 ± 2
λ	0.1±0.2	-0.28±0.6	-0.06±0.04	-0.07±0.06	-0.13±0.04	-0.6±0.2	0.3 ± 0.1	0.2±0.1	-0.05±0.04

Table 4.E2) *Average difference in extracted OVSED model parameters for all three SWNT based TFTs during the Soaking phase. V_T is the threshold voltage, λ is the ratio between the channel length and mean free path. The λ parameter is normalized using the pre-soaked value. Data extracted from 4-6 devices for each wavelength and polymer, totalling 46 devices, all were illuminated using an intensity of 4W/cm^2.*

Model parameter differences	Photo Cycling phase 405nm			Photo Cycling phase 532nm			Photo Cycling phase 980nm		
	PCF	PFMB	PFO-BPy	PCF	PFMB	PFO-BPy	PCF	PFMB	PFO-BPy
V_T (V)	11 ± 3	4 ± 1	4 ± 2	2 ± 1	3.4±0.6	1.0±0.2	3.5±0.9	2.6±0.7	2.6±0.8
λ	-0.17±0.09	-0.03±0.02	0.03±0.02	0.02±0.06	0.00±0.03	-0.01±0.02	0.3±0.2	-0.03±0.06	-0.01±0.05

Table 4.E3) *Average difference in extracted OVSED model parameters for all three SWNT based TFTs during the Photo Cycling phase. V_T is the threshold voltage, λ is the ratio between the channel length and mean free path. The λ parameter is normalized using the pre-soaked value. Data extracted from 4-6 devices for each wavelength and polymer, totalling 46 devices, all were illuminated using an intensity of 4W/cm^2.*

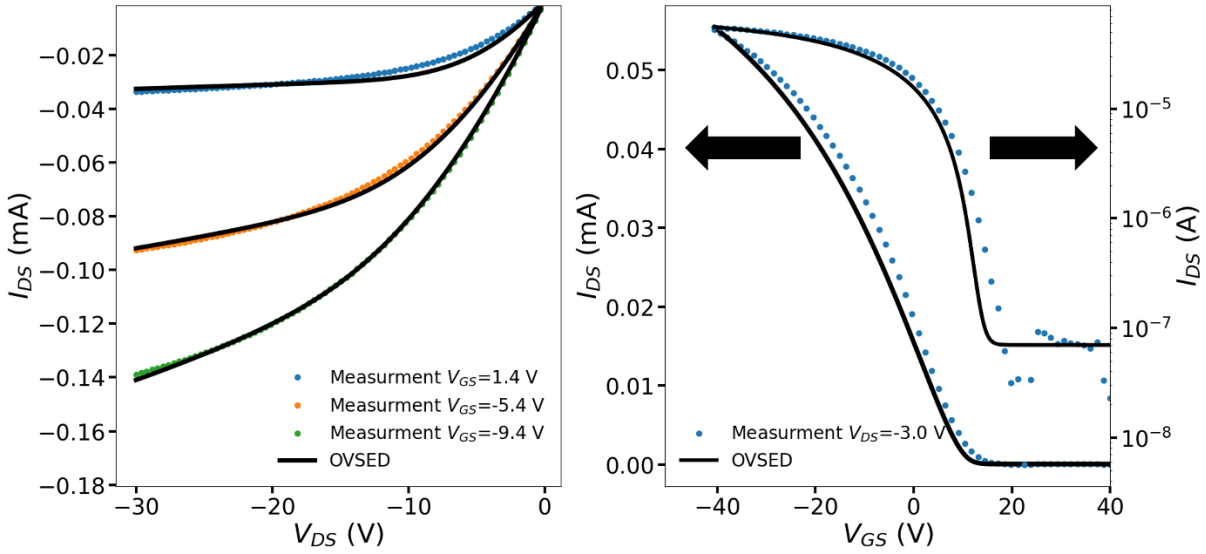

Figure 4.E8) *Characteristic output and transfer curve for a PFMB+SWNT pre-Soak device with the OVSED model fitting.*

Chapter 5: OVSED Modeling of SWNT TFTs

5.1. Context

From the previous three works, the OVSED model has shown promising outcomes by providing better curve fittings compared to the SH model, along with extracting new parameters giving further insight on the innerworkings of TFTs. This section provides a connection between the two thesis chapters by applying the OVSED to SWNT TFT data, comparing it to N2200 based TFTs and included improved user interface through more accessible Python code.

5.2. Introduction

In this work I applied the organic virtual source emission diffusion (OVSED) model to SWNTs TFT with three different dispersion polymers and compared the result to the N2200 from the previous study in chapter 3. Although the SWNT TFTs were tested as a *p*-type and the N2200 based OTFTs as an *n*-type, therefore, the charge carriers are holes in one and electrons in the other, the parameters can still be compared by characterizing common factors such as current density, the density of trapped states and the voltage dependent contact resistance. The Virtual Source model, a sub-model incorporated in the OVSED model, has previously been used on SWNT based TFTs with promising results.[1,2] Modeling the SWNT based TFT using the OVSED model enables benchmarking these materials to other organic semiconductors who cannot be modeled simply using the Virtual Source sub-model, while still containing the Virtual Source limit embedded in

the OVSED model. Four different samples were compared using the OVSED model: three SWNT TFTs using different types of polymer wrappings, PCF, PFMB and PFO-BPy, were compared to a N2200 based TFT.

5.3. Results and Discussion

Figure 5.1 shows a characteristic plot of the SWNT device fittings and he summary of the results from this study is displayed in **Table 5.1** with the average value for each parameter along with their standard error. Although, the SWNT devices were tested as p-type, the V_T is heavily shifted in the positive regime. From the δ values, we can see that SWNT's variable V_T has higher dependence on the source drain voltage than the N2200.

Model Parameters	PCF+SWNT	PFMB+SWNT	PFO-BPy+SWNT	N2200
V_T (V)	18.6±0.8	19±1	17±1	17.5±0.8
δ	0.021±0.009	0.016±0.006	0.0021±0.0009	1.11±0.08 x 10^{-8}
n	138±9	100±10	68±2	55±0.7
l	2.4±0.1	2.1±0.1	2.3±0.2	1.003±0.003
λ	10±1 x 10^5	40±3 x 10^5	9±3 x 10^5	3.9±0.3 x 10^5
V_{gcrit}(V)	22±9 x 10^5	5±8 x 10^4	8±3 x 10^5	80±50
J_T (A/cm)	0.37±0.09	0.23±0.06	0.07±0.03	0.009±0.002
V_{tun} (V)	-13±3	-15±2	-8±2	30±10
V_0 (V)	-14±5	-39±3	-19±4	30±10
R_0 (kΩ)	1.1±0.3	2.8±0.6	2.0±0.5	4±3
R_{max} (kΩ)	12±3	60±10	30±10	120±10

Table 5.1) *Average extracted OVSED model parameters for all three SWNT based TFTs and a N2200 based OTFT, all with Au/Mn contacts. V_T is the threshold voltage, δ a variable threshold constant, n is a gate coupling factor, l density of trap states constant, λ is the ratio between the gate length and mean free path, V_{crit} is the critical voltage for carrier velocity saturation, J_T is the current density, V_0 is the turning point for the contact resistance, V_{tun} is the smoothing factor for the contact resistance, R_0 is the minimum contact resistance, R_{max} is the maximum contact resistance. Data extracted from 15-16 devices for each polymer and 3 N2200, totalling 49 devices.*

The *n* and *l* elucidate the charge trap condition, with both having 1 indicating a negligible density of charge traps. From this we surmise that the SWNT have more charge traps which could

be a result of excess conjugated polymer, absorbed oxygen, absorbed moisture or other defects leading to charge trapping, with the PCF wrapped SWNT containing the most traps. Unlike the SWNT films, N2200 would make a solid polymer film which could be more resistant to moisture and oxygen permeation. The λ is directly related to mobility, μ, and the mean free path λ_f:

$$\lambda = L_G/\lambda_f \tag{5.1}$$

$$\mu = \frac{\nu_T}{2V_{temp}}\lambda_f \tag{5.2}$$

Where L_G is the gate length (~20 μm), which stays constant, υ_T is the carrier velocity and V_{temp} is the thermal voltage. Thus, the model suggests SWNT TFTs have a larger carrier mean free path and greater μ compared to the N2200 TFTs, which is consistent with reports on these two semiconductors[3-6]. The $V_{g\ crit}$ is a lot larger for SWNT, suggesting it may tend towards infinity, which indicates they are not plagued by a limited drift velocity in the channel[7] compared to the N2200. The current density, J_T, is considerably larger for SWNT, with PCF having the largest density, this is also expected, as SWNT have larger μ s. The V_{tun} designates how fast the change from R_{max} to R_{min} takes place, and V_0 determines where along the V_{DS} the middle of the change happens. Since the absolute value V_0 is above zero, there is a change in contact resistance and the resistance in all the devices are dependent on the source drain voltage. V_{tun} is negative with the SWNT devices, indicating that rather than decreasing the contact resistance as a function of V_{DS}, the R_C increases. R_o is surprisingly similar for all types, although R_{max} is larger for N2200 suggesting a faster current saturation and a larger contact resistance.

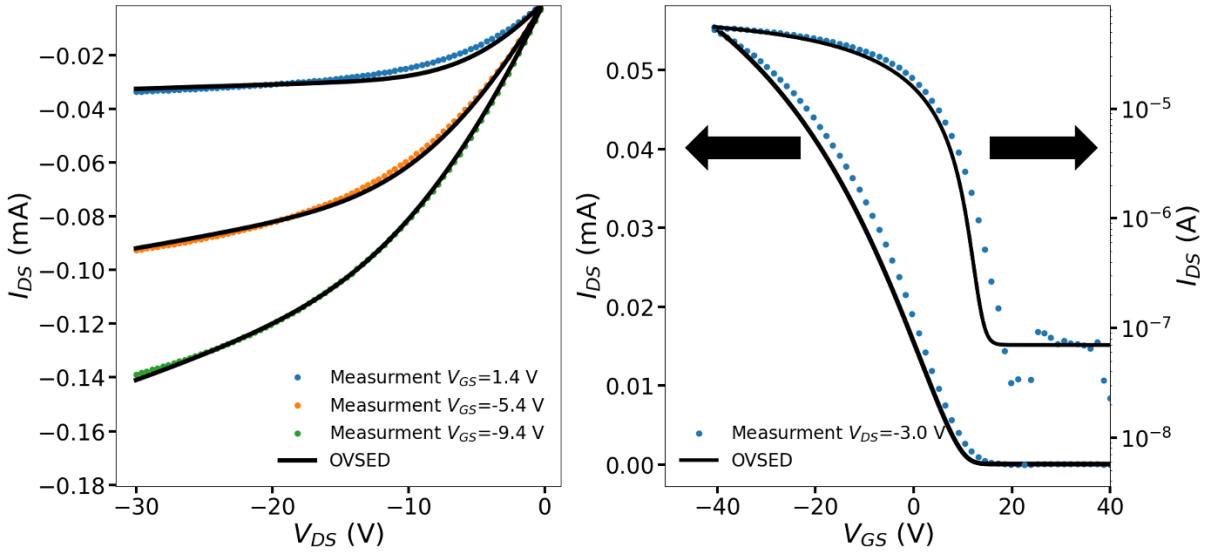

Figure 5.1) *Characteristic output and transfer curve for a PFMB+SWNT device with the OVSED model fitting.*

When comparing the SWNT devices, they all had similar V_T, $V_{g\ crit}$ and contact resistance characteristics, V_{tun}, R_0, V_0 and R_{max}, although, V_0 was larger for PFMB devices, indicating that the change in contact resistance occurs further along the V_{DS}. The PCF wrapped SWNT TFT has a larger source drain voltage dependent V_T, indicated by the larger δ. Similarly, the model seems to suggest a larger charge trap density for PCF, when comparing the n and l parameters. The model also shows a larger charge density for PCF and PFMB. This concurs with the nanotube diameters as PFO-BPy is well known for dispersing smaller diameter semiconducting SWNT with a preference towards the (6,5) chirality[8,9], and polymers with larger alkyl groups, such as PCF and PFMB, preferentially disperse larger diameter nanotubes [10]. Overall these results demonstrate that the OVSED is a powerful tool for comparing different semiconductors and their resulting TFT performance.

5.4. Conclusion

In conclusion, the OVSED model provides good fits and provides further insight into TFT performance. In particular, the model gives a better understanding on carrier mean free path, source

drain voltage dependent contact resistance and V_T, charge carrier velocity saturation and density of charge traps, all of which are very important when benchmarking novel TFT and OTFTs. When comparing the SWNT based devices to the N2200 devices, the model suggests that the SWNT TFTs contain a larger charge trap density, which could indicate more defects and impurities. The model also shows that they have a larger current density, mean free path and μ, all of which agree with current reports. When comparing the SWNT devices, the PCF dispersed devices seem to offer better current density but contain a larger concentration of defects and charge traps. In addition to being a great benchmarking tool, the model provides a method to diagnose OTFTs and TFTs alike and paves a path for OTFT researchers to helps improve their designs.

5.5. Methods

The fabrication of the SWNT TFT has been described in the methodology section of Chapter 4, while the equations for the OVSED model is included in the methodology section of Chapter 3. The model code in python has been included below for convenience.

5.5.1. Model Code

The code was originally written in MATLAB, but as an effort of adopting more open-source software, the code was re-written in python using the numpy, scipy, pandas and matplotlib.pyplot libraries. The entire python code has been inserted bellow.

```
#%% Import
import pandas as pd
import numpy as np
import matplotlib.pyplot as plt
from scipy import optimize as sci_op
#%% functions
def Extract_O_Data(file):
    '''Extracts the x and y data from a txt file'''
```

```
    data_og=pd.read_csv(file, sep='\t', lineterminator='\n')
    data=data_og.to_numpy()
    Vds=data[:,0]
    Vgs=(np.array(data_og.columns,dtype='str'))[1:]
    Ids=np.transpose(data[:,1:])
    Vgs=np.char.replace(Vgs,'\r','')
    Vgs=np.char.replace(Vgs,'V','')
    Vgs=np.array(Vgs,dtype="float")
    return Vds, Ids, Vgs

def Extract_T_Data(file):
    '''Extracts the x and y data from a txt file'''
    data_og=pd.read_csv(file, sep='\t', lineterminator='\n',header=None,encoding = "cp1252")
    data_og=data_og[~data_og[0].isnull()]# get rid of nan
    #separate info
    MainInfo=np.array(data_og.iloc[::6, 0:11],dtype="str")
    ForwardInfo=np.array(data_og.iloc[1::6, 0:5],dtype="str")
    BackwardInfo=np.array(data_og.iloc[2::6, 0:5],dtype="str")
    Vgs=np.array(data_og.iloc[3::6,1:-1],dtype="float")
    Vgs=Vgs[:,Vgs[0]==Vgs[0]]
    Ids=np.array(data_og.iloc[4::6,1:-1],dtype="float")
    Ids=Ids[:,Ids[0]==Ids[0]]
    Igs=np.array(data_og.iloc[5::6,1:-1],dtype="float")
    Igs=Igs[:,Igs[0]==Igs[0]]
    return MainInfo, ForwardInfo, BackwardInfo, Vgs, Ids, Igs
def Sep(Vgs,Ids,typ):
    '''Seperates forward/backwards'''
    if typ==1:
        index=(np.where(Vgs[0][1:]-Vgs[0][:-1]<=0))[0][1]                #forwards to backwards
    else:
        index=(np.where(Vgs[0][1:]-Vgs[0][:-1]>=0))[0][1]
    VgsF=np.transpose(Vgs[:,:index])
    VgsB=np.transpose(Vgs[:,index:])
    IdsF=np.transpose(Ids[:,:index])   #Forward currents
    IdsB=np.transpose(Ids[:,index:])   #Backwards currents
    Forward=[VgsF,IdsF]
    Backward=[VgsB,IdsB]
    return Forward, Backward

def Output_config(Vds,Ids,typ):
    '''separates the data to only get FET range based off type'''
    min_index=np.where(Vds==(Vds[np.abs(Vds)==np.min(np.abs(Vds))][0]))[0][0]
    if typ==-1 and Vds[min_index]>0:  #make sure the start is in the range if the min isnt
        min_index+=1
    elif typ==1 and Vds[min_index]<0:
        min_index-=1
    new_Vds=Vds[min_index :]*typ
    new_Ids=Ids.T[min_index :]*typ
    return new_Vds, new_Ids.T


def effec_Volt(Vds_T, Vgs_T, Vds_O, Ids_O, Ids_T):
    '''Calculates the effective gate voltages'''
    Diff=abs(Vds_O-Vds_T)
    index=np.where(Diff==min(Diff))[0][0]  #index where Vds_O=Vds_T
    Ids_Vds=abs(Ids_O[:,index])
    Ids_T_mat=np.ones((len(Ids_Vds),len(Ids_T)))*Ids_T #matrix of Ids_T to compare
    Ids_Vds_mat=np.outer(Ids_Vds, np.ones(len(Ids_T)))#matrix of Ids_Vds values
    Diff2=abs(Ids_T_mat-Ids_Vds_mat)   #difference
    mins=np.outer(np.min(Diff2,1), np.ones(len(Ids_T)))  #find the row minimums and make a matrix
    indicies=np.where(Diff2==mins)[1]  #find all the indicies, one per row
    effec_volt=Vgs_T[indicies]+1     #get the effective voltages from Vgs_T and round up
    N=len(effec_volt)
    eff_Volt_label=[]
    for z in range(N):   #to check if they're actually over what I can see
        if indicies[z]==len(Vgs_T)-1 or indicies[z]==0:
            eff_Volt_label.append("over")
        else:
            eff_Volt_label.append(str(np.round(effec_volt[z],decimals=1)))
    return effec_volt
```

```
def OVSED_fit(Vv, Vtho,delta,n,l,lam,Vgcrit,Jth,Rso,Vtun,V0,Rmax):
    for i in range(5):
        if i<2:
            Vds = Vdsp[i]  #simulate transfer
            Vgs = Vv[i]
        else:
            Vds = Vv[i]     #simulate output
            Vgs = Vgsp[i-2]



        #Drain impact
        Vtp=Vtho+Vds*delta
        #Total charge (normalized)
        nphit=n*phit
        theta=(Vgs-Vtp)/(nphit)
        qtot = np.log(1+np.exp(theta))
        #Fsat calculation - Long channel device
        Vgt = nphit*qtot
        Vgn = 2*Vgt/(1+np.sqrt(2*Vgt/Vgcrit))
        x = Vds/Vgn
        eta = 1-np.tanh(2*x)
        y = Vgn/phit
        if type(Vds)==np.ndarray:
            if Vds[0] == 0:  #fix a devide by 0 error
                ll = (2*lam/(y[1:]*y[1:]*(1-eta[1:]*eta[1:])))*(np.exp(y[1:]*(eta[1:]-1))*(1-y[1:]*eta[1:])-(1-y[1:]))
                ll = np.append(lam,ll)
            else:
                ll = (2*lam/(y*y*(1-eta*eta)))*(np.exp(y*(eta-1))*(1-y*eta)-(1-y))
        else:
            ll = (2*lam/(y*y*(1-eta*eta)))*(np.exp(y*(eta-1))*(1-y*eta)-(1-y))
        tau = 1/(1+ll)
        at = tau/(2-tau)
        #1/(1+2*ll)
        Fsat = at*(1 - np.exp(-Vds/phit))/(1 + at*np.exp(-Vds/phit))


        try:
            Fsat[np.isnan(Fsat)]=0
        except TypeError:
            continue
        #Current calculation
        Jfree = Jth*qtot**l
        #Final
        Idx = Idleak + W*Jfree*Fsat
        Idxx=Idleak
        Rs = Rso + 0.5*(Rmax-Rso)*(1-np.tanh((Vds-V0)/Vtun))
        Rd = Rso
        dvg=Idx*Rs
        dvd=Idx*Rd
        count=1
        while np.max(np.abs((Idx-Idxx)/Idx))<1e-10:#error condition
            count=count+1
            if count>500:
                break
            Idxx=Idx
            #dvg=(Idx*Rs+dvg)/2
            #dvd=(Idx*Rd+dvd)/2; CHANGE
            #dvds=dvg+dvd;
            dvg=0.2*Idx*Rs+0.8*dvg
            dvd=0.2*Idx*Rd+0.8*dvd
            dvds=dvg+dvd
            Vdsi=np.maximum(Vds-dvds,0)   #n-type solution
            Vgsi=np.maximum(Vgs-dvg,0)
            #Drain impact
            Vtp=Vtho+Vdsi*delta

            #Total charge (normalized)
            nphit=n*phit
```

```
            theta=(Vgsi-Vtp)/(nphit)
            qtot = np.log(1+np.exp(theta))
            #Fsat calculation - Long channel device
            Vgt = nphit*qtot
            Vgn = 2*Vgt/(1+np.sqrt(2*Vgt/Vgcrit))
            x = Vdsi/Vgn
            eta = 1-np.tanh(2*x)
            y = Vgn/phit
            if type(Vds)==np.ndarray and type(y)==np.ndarray and type(eta)==np.ndarray:
               if Vds[0] == 0:  #fix a devide by 0 error
                  ll = (2*lam/(y[1:]*y[1:]*(1-eta[1:]*eta[1:])))*(np.exp(y[1:]*(eta[1:]-1))*(1-y[1:]*eta[1:])-(1-y[1:]))
                  ll = np.append(lam,ll)
               else:
                  ll = (2*lam/(y*y*(1-eta*eta)))*(np.exp(y*(eta-1))*(1-y*eta)-(1-y))
            else:
               ll = (2*lam/(y*y*(1-eta*eta)))*(np.exp(y*(eta-1))*(1-y*eta)-(1-y))
            tau = 1./(1+ll)
            at = tau/(2-tau)
            #1/(1+2*ll)
            Fsat = at*(1 - np.exp(-Vdsi/phit))/(1 + at*np.exp(-Vdsi/phit))
            try:
               Fsat[np.isnan(Fsat)]=0
            except TypeError:
               pass


            #Current calculation
            Jfree = Jth*qtot**l
            #Final
            Idx = Idleak + W*Jfree*Fsat
            #Wrapping up
         if i<2:
            #Id[i] = np.log10(Idx)
            Id[i] = Idx
         else:
            Id[i] = Idx
      Id_array=np.array([])
      for i in range(5):
         Id_array=np.append(Id_array,Id[i])
      return Id_array
   def OVSED_fit_plot(Vv, Vtho,delta,n,l,lam,Vgcrit,Jth,Rso,Vtun,V0,Rmax):
      Id=[0,0,0,0,0] #transfer x2, output x3
      for i in range(5):
         if i<2:
            Vd = Vdsp[i]  #simulate transfer
            Vg = Vv[i]
            Vs=0   #change if Vs isn't ground
            direc=np.sign(Vd-Vs)
            Vds=np.abs(Vd-Vs)

            Vgs=np.maximum((Vg-Vs),(Vg-Vd))
         else:
             Vd = Vv[i]     #simulate output
             Vg = Vgsp[i-2]
             Vs=0   #change if Vs isn't ground
             direc=np.sign(Vd-Vs)
             Vds=np.abs(Vd-Vs)

             Vgs=np.maximum((Vg-Vs),(Vg-Vd))
         #Drain impact
         Vtp=Vtho+Vds*delta
         #Total charge (normalized)
         nphit=n*phit
         theta=(Vgs-Vtp)/(nphit)
         qtot = np.log(1+np.exp(theta))
         #Fsat calculation - Long channel device
         Vgt = nphit*qtot
         Vgn = 2*Vgt/(1+np.sqrt(2*Vgt/Vgcrit))
         x = Vds/Vgn
         eta = 1-np.tanh(2*x)
```

```
y = Vgn/phit
if type(Vds)==np.ndarray:
    if Vds[0] == 0:  #fix a devide by 0 error
        ll = (2*lam/(y[1:]*y[1:]*(1-eta[1:]*eta[1:])))*(np.exp(y[1:]*(eta[1:]-1))*(1-y[1:]*eta[1:])-(1-y[1:]))
        ll = np.append(lam,ll)
    else:
        ll = (2*lam/(y*y*(1-eta*eta)))*(np.exp(y*(eta-1))*(1-y*eta)-(1-y))
else:
    ll = (2*lam/(y*y*(1-eta*eta)))*(np.exp(y*(eta-1))*(1-y*eta)-(1-y))

tau = 1/(1+ll)
at = tau/(2-tau)
#1/(1+2*ll)
Fsat = at*(1 - np.exp(-Vds/phit))/(1 + at*np.exp(-Vds/phit))
try:
    Fsat[np.isnan(Fsat)]=0
except TypeError:
    print('error')
    pass
#Current calculation
Jfree = Jth*qtot**l
#Final
Idx = Idleak + W*Jfree*Fsat

Idxx=Idleak
Rs = Rso + 0.5*(Rmax-Rso)*(1-np.tanh((Vds-V0)/Vtun))
Rd = Rso
dvg=Idx*Rs
dvd=Idx*Rd
count=1
while np.max(np.abs((Idx-Idxx)/Idx))<1e-10:#error condition <1e-10
    count=count+1
    if count>500:
        print('break')
        print(i)
        break
    Idxx=Idx
    #dvg=(Idx*Rs+dvg)/2
    #dvd=(Idx*Rd+dvd)/2; CHANGE
    #dvds=dvg+dvd;
    dvg=0.2*Idx*Rs+0.8*dvg
    dvd=0.2*Idx*Rd+0.8*dvd
    dvds=dvg+dvd
    Vdsi=np.maximum(Vds-dvds,1e-9)   #n-type solution
    Vgsi=np.maximum(Vgs-dvg,1e-9)
    #Drain impact
    Vtp=Vtho+Vdsi*delta
    #Total charge (normalized)
    nphit=n*phit
    theta=(Vgsi-Vtp)/(nphit)
    qtot = np.log(1+np.exp(theta))
    #Fsat calculation - Long channel device
    Vgt = nphit*qtot
    Vgn = 2*Vgt/(1+np.sqrt(2*Vgt/Vgcrit))
    x = Vdsi/Vgn
    eta = 1-np.tanh(2*x)
    y = Vgn/phit
    if type(Vds)==np.ndarray and type(y)==np.ndarray and type(eta)==np.ndarray:
        if Vds[0] == 0:  #fix a devide by 0 error
            ll = (2*lam/(y[1:]*y[1:]*(1-eta[1:]*eta[1:])))*(np.exp(y[1:]*(eta[1:]-1))*(1-y[1:]*eta[1:])-(1-y[1:]))
            ll = np.append(lam,ll)
        else:
            ll = (2*lam/(y*y*(1-eta*eta)))*(np.exp(y*(eta-1))*(1-y*eta)-(1-y))
    else:
        ll = (2*lam/(y*y*(1-eta*eta)))*(np.exp(y*(eta-1))*(1-y*eta)-(1-y))
    tau = 1./(1+ll)
    at = tau/(2-tau)
    #1/(1+2*ll)
    Fsat = at*(1 - np.exp(-Vdsi/phit))/(1 + at*np.exp(-Vdsi/phit))
```

```
            try:
                Fsat[np.isnan(Fsat)]=0
            except TypeError:
                pass
            #Current calculation
            Jfree = Jth*qtot**l
            #Final
            Idx = Idleak + W*Jfree*Fsat

            #Wrapping up


        Id[i] = Idx*direc

    return Id

#%% parameters
Sample=40
Device=20
phase='L'

path=FILE PATH HERE
FolderT="transfer"
FolderO="output"
endT="transfer"
endO="output"

fileT1=path+"\\{}\\{}\\30L_{}{}.{}".format(FolderT,Sample,Device,phase,endT)
fileT2=path+"\\{}\\{}\\30L_{}{}.{}".format(FolderT,Sample,Device,phase,endT)
fileO=path+"\\{}\\{}\\30L_{}{}.{}".format(FolderO,Sample,Device,phase,endO)

Curves=[1,2,3] #which output curves do you want, count starts at 0
typ=-1 #type of transistor. nFET type=1; pFET type=-1
bounds="yes"  #did you want bounds?
Effective_V="yes"
guess='yes'
Eff_trans=1 #what transfer curve to base the effective volatges (0 or 1)
Tran_run=-1 #last =-1
#First guess

Vtho=18.50686279
delta=1.80568E-08
n=68.23064188
l=1.499152193
lam=3535929.22
Vgcrit=88718.90268
Jth=0.522018976
Rso=5968.512004
Vtun=-16.28353495
V0=-25.35274402
Rmax=27669.46106
Idleak=7e-8
W=0.09      #transistor width (cm)
kB=8.617e-5        # Boltzmann constant [eV/K]
Tjun=293           #Junction temperature [K].
phit = kB*Tjun
shift='max'     #max if you just want to shift the whole thing, a number if if want to be spacific
# err = 1
# i = 0
# resnorm1min = 1
# resnorm2min = 1
#[    Vtho, delta, n,   l, lam, Vgcrit, Jth, Rso, Vtun, V0, Rmax]
lb = [15.00, 1e-10, 1e1, 1, 1e1, 0.000, 1e-6, 0.0,-60.0,-60, 6.2e3]# lower bound constraints
ub = [45.00, 1.00, 2.0e2, 5, 3e7, 4e7, 1.00, 6.2e3, 0.00, 0., 5e5]# upper bound constraints
const=[Idleak,W,phit]
Value_names=['Vtho', 'delta', 'n','l', 'lam','Vgcrit','Jth','Rso','Vtun','V0','Rmax']
First_guess=np.array([Vtho,delta,n,l,lam,Vgcrit,Jth,Rso,Vtun,V0,Rmax])
#Graph param
```

```
top=0.82
bottom=0.101
left=0.1
right=0.91
hspace=0.27
wspace=0.225
#%% bound test
for i in range(len(First_guess)):
    if First_guess[i]<lb[i] or First_guess[i]>ub[i]:
        print('invalid {}'.format(Value_names[i]))
#%% data setup
#output
Vds_O_og, Ids_O_og, Vgs_O=Extract_O_Data(fileO)
Vds_O, Ids_O=Output_config(Vds_O_og,Ids_O_og,typ)
#transfer

MainInfo_1, ForwardInfo_1, BackwardInfo_1, Vgs_T1, Ids_T1, Igs_T1=Extract_T_Data(fileT1)
MainInfo_2, ForwardInfo_2, BackwardInfo_2, Vgs_T2, Ids_T2, Igs_T2=Extract_T_Data(fileT2)

Vds_T1=int(MainInfo_1[0,6][4:-1])*typ
Vds_T2=int(MainInfo_2[0,6][4:-1])*typ
Run1_F, Run1_B=Sep(Vgs_T1,Ids_T1,typ) #sep forward and backwards
Vgs_T1F=Run1_F[0]
Ids_T1F=Run1_F[1]
Run2_F, Run2_B=Sep(Vgs_T2,Ids_T2,typ) #sep forward and backwards
Vgs_T2F=Run2_F[0]
Ids_T2F=Run2_F[1]
#implementing the shift
if shift=='max':
    shift=np.max(Vgs_T1F*typ*-1)*typ*-1 #gets the opposite voltage maximum for each type

Vgs_T1F=(Vgs_T1F-shift)*typ
Vgs_T2F=(Vgs_T2F-shift)*typ  #flips it if it's n-type

lb[0]=(lb[0]-shift)
ub[0]=(ub[0]-shift)

lb[8],ub[8]=ub[8]*typ,(lb[8]*typ)
First_guess[8]=First_guess[8]*typ
lb[9],ub[9]=ub[9]*typ,(lb[9]*typ)
First_guess[9]=First_guess[9]*typ

if typ==-1:
    ub[0],lb[0]=(lb[0])*-1,ub[0]*-1  #shift and switch



First_guess[0] = (First_guess[0]-shift)*typ

Vv=[0,0,0,0,0]  #list of all the sweeping voltages, transfer Vgs 1 & 2 then output Vds 1-3
Id=[0,0,0,0,0]  #both transfer and last 3 output curves
num_transfer_pts= 60
num_output_pts=60
Vv[0]=np.linspace(np.min(Vgs_T1F),np.max(Vgs_T1F),num_transfer_pts)
Id[0]=np.interp(Vv[0],Vgs_T1F[:,Tran_run],Ids_T1F[:,Tran_run])
#Id[0]=np.log10(np.interp(Vv[0],Vgs_T1F[:,Tran_run],Ids_T1F[:,Tran_run]))
Vv[1]=np.linspace(np.min(Vgs_T2F),np.max(Vgs_T2F),num_transfer_pts)
Id[1]=np.interp(Vv[1],Vgs_T2F[:,Tran_run],Ids_T2F[:,Tran_run])
#Id[1]=np.log10(np.interp(Vv[1],Vgs_T2F[:,Tran_run],Ids_T2F[:,Tran_run]))

Vv[2]=Vv[3]=Vv[4]=np.linspace(np.min(Vds_O),np.max(Vds_O),num_output_pts)
Id[2]=np.interp(Vv[2],Vds_O,Ids_O[Curves[0]])
Id[3]=np.interp(Vv[3],Vds_O,Ids_O[Curves[1]])
Id[4]=np.interp(Vv[4],Vds_O,Ids_O[Curves[2]])
for i in range(2,5):
    if Vv[i][0]==0:
        Id[i][0]=0
```

```
if ("y" in Effective_V) or ("Y" in Effective_V): #implement the effective voltages
    Vds_T_lst=[Vds_T1,Vds_T2]
    Vgs_T_lst=[Vgs_T1F,Vgs_T2F]
    Ids_T_lst=[Ids_T1F,Ids_T2F]
    Vgs_O=effec_Volt(Vds_T_lst[Eff_trans], np.transpose(Vgs_T_lst[Eff_trans])[Tran_run], Vds_O, Ids_O,
np.transpose(Ids_T_lst[Eff_trans])[Tran_run])
else:
    Vgs_O=(Vgs_O-shift)*typ #using effective voltages shitches it automatically
Vdsp=[abs(Vds_T1), abs(Vds_T2)]
Vgsp=[abs(Vgs_O[Curves[0]]), abs(Vgs_O[Curves[1]]), abs(Vgs_O[Curves[2]])] #list of the set voltages, transfer then output
Id_array=np.array([])
for i in range(5):
    Id_array=np.append(Id_array,Id[i]) #put them all in one (will split latter)
Id_arrayPreModel=Id_array.copy()
#%% now curve fit
Verbose=2 #display steps, 0 none, 1 final only, 2 each step
Ftol=1e-7# function tolerances min=2.22e-16
Xtol=1e-7# step tolerances min=2.22e-16 defult 1e-9
max_Eval=1000 #maximum number of evaluations if tolerances aren't reached
Gtol=1e-7

if ("y" in guess) or ("Y" in guess): #implement the first guess or not

    if ("y" in bounds) or ("Y" in bounds): #implement the bounds
        popt,pcov=sci_op.curve_fit(OVSED_fit, Vv, Id_arrayPreModel,max_nfev=max_Eval,
        p0=First_guess, verbose=2, ftol=Ftol, xtol=Xtol, gtol=Gtol, bounds=(lb, ub))
    else:
        popt,pcov=sci_op.curve_fit(OVSED_fit, Vv, Id_arrayPreModel,
        p0=First_guess, ftol=Ftol, xtol=Xtol, gtol=Gtol)

else:
    if ("y" in bounds) or ("Y" in bounds): #implement the bounds
        popt,pcov=sci_op.curve_fit(OVSED_fit, Vv, Id_arrayPreModel,max_nfev=max_Eval,
        p0=None, verbose=2, ftol=Ftol, xtol=Xtol, gtol=Gtol, bounds=(lb, ub))
    else:
        popt,pcov=sci_op.curve_fit(OVSED_fit, Vv, Id_arrayPreModel,
        p0=None, ftol=Ftol, xtol=Xtol, gtol=Gtol)
Error=np.sqrt(np.diag(pcov)) #standard deviation error
#%%plot

LabelSize=30
TickSize=25
linewidth=5

Vtho = popt[0]
delta = popt[1]
n = popt[2]
l = popt[3]
lam = popt[4]
Vgcrit = popt[5]
Jth = popt[6]
Rso = popt[7]
Vtun = popt[8]
V0 = popt[9]
Rmax = popt[10]

Vv_plot=[0,0,0,0,0]

Vv_plot[0]=Vv_plot[1]=np.arange(np.min(Vgs_T1F.T[0]),np.max(Vgs_T1F.T[0]),0.1)

#Vv_plot[0]=Vv_plot[1]=np.arange(20,90.5,0.1)


Vv_plot[2]=Vv_plot[3]=Vv_plot[4]=np.arange(np.min(Vds_O),np.max(Vds_O),0.1)


print('''Vtho={} \ndelta={} \nn={} \nl={} \nlam={} \nVgcrit={} \nJth={} \nRso={}
Vtun={} \nV0={} \nRmax={}'''.format(Vtho*typ+shift,delta,n,l,lam,Vgcrit,Jth,Rso,Vtun*typ,V0*typ,Rmax))

print('''\n\n\n{} \n{} \n{} \n{} \n{} \n{} \n{}
```

```
{} \n{} \n{}'".format(Vtho*typ+shift,delta,n,l,lam,Vgcrit,Jth,Rso,Vtun*typ,V0*typ,Rmax))
Id_plot=OVSED_fit_plot(Vv_plot,Vtho,delta,n,l,lam,Vgcrit,Jth,Rso,Vtun,V0,Rmax)
Id_plot_O1=np.array(Id_plot[2]).T*1000
Id_plot_O2=np.array(Id_plot[3]).T*1000
Id_plot_O3=np.array(Id_plot[4]).T*1000
Id_plot_T1=np.array(Id_plot[0]).T
Id_plot_T2=np.array(Id_plot[1]).T
fig1, ax = plt.subplots(1,2)
plt.subplots_adjust(left=left, bottom=bottom, right=right, top=top, wspace=wspace, hspace=hspace)
ax[0].plot(Vds_O*typ, Ids_O[Curves[0]]*typ*1000, 'o', label=r"Measurment $V_{GS}$="+"{:.1f} V".format(Vgs_O[Curves[0]]*typ+shift))
ax[0].plot(Vds_O*typ, Ids_O[Curves[1]]*typ*1000, 'o', label=r"Measurment $V_{GS}$="+"{:.1f} V".format(Vgs_O[Curves[1]]*typ+shift))
ax[0].plot(Vds_O*typ, Ids_O[Curves[2]]*typ*1000, 'o', label=r"Measurment $V_{GS}$="+"{:.1f} V".format(Vgs_O[Curves[2]]*typ+shift))
ax[0].plot(Vv_plot[2]*typ, Id_plot_O1*typ, '-', label="OVSED", color='black', linewidth=linewidth)
ax[0].plot(Vv_plot[2]*typ, Id_plot_O2*typ, '-', color='black', linewidth=linewidth)
ax[0].plot(Vv_plot[2]*typ, Id_plot_O3*typ, '-', color='black', linewidth=linewidth)
ax[0].set_ylabel(r"$I_{DS}$ (mA)",fontsize=LabelSize)
ax[0].set_xlabel(r"$V_{DS}$ (V)",fontsize=LabelSize)
ax[0].tick_params(axis='y', labelcolor="black",labelsize=TickSize)  #label colour
ax[0].tick_params(axis='x', labelcolor="black",labelsize=TickSize)  #label colour
ax[0].legend(fontsize=LabelSize-10, framealpha=0)
ax[0].xaxis.set_tick_params(width=3,length=8)
ax[0].yaxis.set_tick_params(width=3,length=8)
ax[0].set_ylim(typ*max(Ids_O[Curves[2]]*1000)*1.3,typ*min(Ids_O[Curves[0]]*1000)*1.1)
#ax[0].set_ylim(typ*max(Ids_O[Curves[2]])*1.3,0)
t = ax[0].yaxis.get_offset_text()
t.set_size(LabelSize-5)

ax[1].plot(Vgs_T1F.T[0]*typ+shift, Ids_T1F.T[0]*1000, 'o', label=r"Measurment $V_{DS}$="+"{:.1f} V".format(Vds_T1*typ))
#ax[1].plot(Vgs_T2F.T[0]*typ+shift, Ids_T2F.T[0]*1000, 'o', label=r"Measurment $V_{DS}$="+"{:.1f} V".format(Vds_T2*typ))
ax[1].plot(Vv_plot[0]*typ+shift, Id_plot_T1*1000,'-',label="OVSED", color='black', linewidth=linewidth)
ax[1].plot(Vv_plot[0]*typ+shift, Id_plot_T2*1000,'-',color='black', linewidth=linewidth)
ax[1].set_ylabel(r"$I_{DS}$ (mA)",fontsize=LabelSize)
ax[1].set_xlabel(r"$V_{GS}$ (V)",fontsize=LabelSize)
ax[1].tick_params(axis='y', labelcolor="black",labelsize=TickSize)  #label colour
ax[1].tick_params(axis='x', labelcolor="black",labelsize=TickSize)  #label colour
ax[1].xaxis.set_tick_params(width=3,length=8)
ax[1].yaxis.set_tick_params(width=3,length=8)
ax[1].set_xlim(min(Vv_plot[0]*typ+shift)-10,max(Vv_plot[0]*typ+shift))


ax2 = ax[1].twinx()
#ax2.plot(Vgs_T1F.T[0]*typ+shift, Ids_T1F.T[0], 'o', label=r"Measurment $V_{DS}$="+"{:.1f} V".format(Vds_T1*typ))
ax2.plot(Vgs_T2F.T[0]*typ+shift, Ids_T2F.T[0], 'o', label=r"Measurment $V_{DS}$="+"{:.1f} V".format(Vds_T2*typ))
ax2.plot(Vv_plot[0]*typ+shift, Id_plot_T1,'-',label="OVSED", color='black', linewidth=4)
ax2.plot(Vv_plot[0]*typ+shift, Id_plot_T2,'-',color='black', linewidth=4)
ax2.set_ylabel(r"$I_{DS}$ (A)",fontsize=LabelSize)
ax2.tick_params(axis='y', labelcolor="black",labelsize=TickSize)  #label colour
ax2.yaxis.set_tick_params(width=3,length=8)
ax2.set_yscale('log')
ax2.legend(fontsize=LabelSize-10, framealpha=0)
```

5.6. References

1. Lee, C.-S. & Wong, H.-S. P. Stanford Virtual-Source Carbon Nanotube Field-Effect Transistors Model. Preprint at https://doi.org/doi:/10.4231/D3BK16Q68 (2015).

2. Lee, C.-S., Pop, E., Franklin, A. D., Haensch, W. & Wong, H.-S. P. A Compact Virtual-Source Model for Carbon Nanotube FETs in the Sub-10-nm Regime—Part II: Extrinsic

Elements, Performance Assessment, and Design Optimization. *IEEE Trans Electron Devices* **62**, 3070–3078 (2015).

3. Brixi, S. *et al.* Air and temperature sensitivity of n-type polymer materials to meet and exceed the standard of N2200. *Sci Rep* **10**, 1–10 (2020).

4. Rice, N. A. *et al.* Polycarbazole-Sorted Semiconducting Single-Walled Carbon Nanotubes for Incorporation into Organic Thin Film Transistors. *Adv Electron Mater* **5**, 1800539 (2019).

5. Mirka, B. *et al.* Polyfluorene-Sorted Semiconducting Single-Walled Carbon Nanotubes for Applications in Thin-Film Transistors. *Chemistry of Materials* **31**, 2863–2872 (2019).

6. Yang Chai, Z. X. P. C. H. C. Horizontally aligned carbon nanotube bundles for interconnect application: diameter-dependent contact resistance and mean free path. *Nanotechnology* **21,23**, (2010).

7. Blawid, S., Dallaire, N. J. & Lessard, B. H. Self-Consistent Extraction of Mobility and Series Resistance: A Hierarchy of Models for Benchmarking Organic Thin-Film Transistors. *IEEE Journal on Flexible Electronics* **1**, 114–121 (2022).

8. Liu, F. *et al.* Comparative study of the extraction selectivity of PFO-BPy and PCz for small to large diameter single-walled carbon nanotubes. *Nano Res* **15**, 8479–8485 (2022).

9. Mistry, K. S., Larsen, B. A. & Blackburn, J. L. High-Yield Dispersions of Large-Diameter Semiconducting Single-Walled Carbon Nanotubes with Tunable Narrow Chirality Distributions. *ACS Nano* **7**, 2231–2239 (2013).

10. Samanta, S. K. *et al.* Conjugated Polymer-Assisted Dispersion of Single-Wall Carbon Nanotubes: The Power of Polymer Wrapping. *Acc Chem Res* **47**, 2446–2456 (2014).

Chapter 6: Conclusion

6.1. Conclusion

Thin film transistors are in an ideal position to address the demand for flexible printable electronics. Paired with carbon-based semiconductors such as N2200 or single walled carbon nanotubes, TFTs have the opportunity to be used as sensors, photoreceptors, and in logic circuitry. This combination could enable roll-to-roll printing of electronics using solution processable materials, lowering fabrication barriers, and enabling high throughput fabrication[1-3] . Unfortunately, diagnosing problems within carbon-based TFTs can be challenging given the current utilised models are based off inorganic semiconductor physics and apply approximations which are unreasonable to assume for organic carbon-based semiconductors[4-7].

In Chapter 3, I elaborated on a project which involved the optimization of electrode interlayer type and thickness to lower contact resistance in N2200 based TFTs. In addition, to improving the organic virtual-source emission-diffusion model, the model was equipped with a voltage dependent contact resistance and voltages corrections. These resulted in obtaining better curve fits when comparing to the traditionally used, inorganic models. In tandem with traditional models, the OVSED model was applied to analyse the contact resistance of the N2200 based TFTs with different electrodes materials using various interlayers. The optimal interlayer was found to be 10 nm of Mn. The project also served as validation for the model as a benchmarking tool to surpass classical models. This work was published in Applied Physics Reviews. The chapter concluded by introducing a second manuscript discussing in depth the limits of the model and establishing a hierarchy of models from the traditional models to the more complex OVSED model.

In the 4th chapter, I applied the traditional models once again with the now improved OVSED model to diagnose the optoelectrical effects on three conjugated polymer wrapped single walled carbon nanotube TFTs. The TFTs were exposed to light with selectively chosen wavelengths corresponding to two semiconducting single walled carbon nanotube absorption peaks, S_{22} and S_{33}, and the polymer's absorption peak. The work revealed two phases when exposed, a "Soaking" phase which compares the pre-exposure state to the initial exposure. For all wavelengths and polymers, the threshold voltage decreased, the leakage current decreased and the mobility increased, although the degree varied upon the polymer and the exposed absorption peak type. The second phase, the "Photo-Cycling" describes the differences between exposures and post-exposures. Once again the threshold and leakage current decreased during illumination, however the mobility scarcely changed. The degree once more depends on the polymer and wavelength. The OVSED model allowed better diagnosis and provided a quantitative position on the innerworkings of the TFTs. The model ultimately concluded that the mean free path was extended during illumination, which could potentially stem from charge trap filling using separated photon-released excitons. This work was also summarized in a published manuscript.

The chapter 5 is the combination of both chapters and all three manuscripts. The chapter discusses the differences between the characterized N2200 devices from chapter 3 and the SWNT devices from chapter 4. The work details the differences in the extracted parameters and discusses potential reasons for the differences, citing current research which agrees with the potential reasons. The chapter concludes stating that the model suggests that although the SWNT devices have a larger mean free path and charge density, they typically contain more charge traps than the N2200 devices. In conclusion, the improved OVSED model is a useful benchmarking tool, optimal to diagnose carbon-based TFT. The new model has helped the optimization of

contact resistance using interlayers and has helped established innerworkings of SWNT photodetectors.

6.2. Future Research

The model holds great promise to optimize TFT research by enabling better characterisation. The application of an accessible version of the OVSED model on more TFTs would enable a better understanding of device performance and allow a better widespread implementation. Improvements to the model could be made to include photon interactions. A final potential project would be the continuation of chapter 4, although it was clear that the type of polymer influenced the degree of change. Comparing two single walled carbon nanotube TFT of same chirality, one wrapped in a conjugated polymer, the other with different extraction process, both exposed to light similarly to what was described in chapter 4 would allow better differentiation between the polymer's optoelectronic properties, particularly when using the improved OVSED model.

6.3. References

1. Minemawari, H. *et al.* Inkjet printing of single-crystal films. *Nature* **475**, 364–367 (2011).
2. Bucella, S. G. *et al.* Inkjet Printed Single-Walled Carbon Nanotube Based Ambipolar and Unipolar Transistors for High-Performance Complementary Logic Circuits. *Adv Electron Mater* **2**, 1600094 (2016).
3. Li, J. *et al.* A stable solution-processed polymer semiconductor with record high-mobility for printed transistors. *Sci Rep* **2**, 754 (2012).
4. McCulloch, I., Salleo, A. & Chabinyc, M. Avoid the kinks when measuring mobility. *Science (1979)* **352**, 1521–1522 (2016).
5. Paterson, A. F. *et al.* Recent Progress in High-Mobility Organic Transistors: A Reality Check. *Adv Mater* e1801079 (2018) doi:10.1002/adma.201801079.
6. Bittle, E. G., Basham, J. I., Jackson, T. N., Jurchescu, O. D. & Gundlach, D. J. Mobility overestimation due to gated contacts in organic field-effect transistors. *Nat Commun* **7**, 10908 (2016).
7. Lin, Y.-J., Tsai, C.-L. & Huang, B.-C. Discrepancy in mobility extracted from transfer and output characteristics of organic thin film transistors. *Appl Phys Lett* **97**, 203509 (2010).